Czech Technical University in Prague
Faculty of Electrical Engineering

Analyte Detection Techniques Based on Specialty Optical Fibers

Dissertation thesis

Prague, January 2019
Ing. Tomáš Němeček

Czech Technical University in Prague
Faculty of Electrical Engineering
Department of Electromagnetic Field

Analyte Detection Techniques Based on Specialty Optical Fibers

Dissertation thesis

Ing. Tomáš Němeček

Doctoral Programme:
Electrical Engineering and Information Technology, P 2612

Doctoral Branch:
Radioelectronic, 2601V010

Supervisor: Ing. Matěj Komanec, Ph.D.
Co-Supervisor: Prof. Ing. Stanislav Zvánovec, Ph.D.

Prague, January 2019

Thesis Supervisor and Co-Supervisor:
    Ing. Matěj Komanec, Ph.D., and Prof. Ing. Stanislav Zvánovec, Ph.D.
    Department of Electromagnetic Field
    Faculty of Electrical Engineering
    Czech Technical University in Prague
    Technická 2
    160 00 Prague 6
    Czech Republic

Declaration

I hereby declare I have written this doctoral thesis independently and quoted all the sources of information used in accordance with methodological instructions on ethical principles for writing an academic thesis. Moreover, I state that this thesis has neither been submitted nor accepted for any other degree.

In Prague, January 2019

....
Ing. Tomáš Němeček

Abstract

Fiber-optic sensors provide several benefits such as immunity to electromagnetic interference, low weight or chemical resistance. These advantages can be exploited in demanding industrial environments, under strong electromagnetic field or in areas with a higher risk of explosion. Dissertation thesis is focused on the refractometric sensing method as a general method allowing detection of liquid analyte presence, measurement of mixture concentration or verification of liquid quality. Specialty optical fibers, tapered and microstructured, which provide enhanced evanescent-wave overlap with studied liquid analytes have been investigated. Special attention was paid to tapered optical fibers, their preparation process, optimal waist diameter determination, long-term stability and sensitivity enhancement based on the taper surface structural modification. Furthermore, a new refractometric method based on microstructured optical fibers has been derived. Microstructured optical fiber sensor has been proposed, measured and characterized for various liquid analytes. Both sensor types, based on tapered optical fibers and microstructured optical fibers, have been compared in terms of their usability and performance in real conditions. A generalized model for sensor design has been derived, with regard to sensor parameters such as sensitivity, dynamic range and refractive index of a particular liquid analyte.

Keywords: Optical fiber sensing, Sensors, Refractometry, Microstructured optical fibers, Multi-mode optical fibers, Tapered optical fibers.

Abstrakt

Vláknově-optické senzory poskytují celou řadu výhod jako například imunitu na elektromagnetické pole, malou hmotnost či chemickou odolnost. Těchto předností lze využít v náročných průmyslových prostředích, v místech, kde by mohlo dojít k výbuchu, či v silném elektromagnetickém poli. Disertační práce byla zaměřena na refraktometrickou metodu měření kapalin, jakožto univerzální metodu umožňující zkoumat přítomnost kapalin, koncentraci daných kapalných směsí či ověřovat kvalitu kapalin. Za účelem zvýšení citlivosti měření byla analyzována speciální optická vlákna, a to taperovaná a mikrostrukturní, která mají zvýšený překryv evanescentní vlny se zkoumanou kapalinou. U taperovaných optických vláken byl kladen důraz na přípravu taperů, nalezení ideálního průměru pasu taperu, dlouhodobé testy stability senzoru a zvýšení citlivosti pomocí modifikace povrchu taperu. Dále byla vyvinuta nová refraktometrická metoda založená na mikrostrukturních optických vláknech. Byl vyvinut senzor obsahující mikrostrukturní optické vlákno, který byl dále charakterizován pro různé kapalné analyty. Oba typy senzoru, tj. na bázi taperovaného a mikrostrukturního optického vlákna, byly porovnány z hlediska jejich parametrů a využitelnosti v reálných podmínkách. Byl odvozen univerzální model, umožňující návrh senzoru s mikrostrukturním optickým vláknem s ohledem na citlivost senzoru, jeho dynamický rozsah a index lomu kapalného analytu.

Klíčová slova: Vláknově-optická detekce, Senzory, Refraktometrie, Mikrostrukturní optická vlákna, Vícevidová optická vlákna, Taperovaná optická vlákna.

Acknowledgements

I would like to acknowledge my supervisor Matěj Komanec, who guided me during my doctoral studies, discussed my ideas and directions of my thesis. Matěj became a close collaborator of my whole research.

I would like to thank my co-supervisor Stanislav Zvánovec, who gave me the unique opportunity to be a part of a great team of people as well as optics specialists. He supported me as a student and developed my professional as well as soft skills.

I would like to thank to Pavel Honzátko, who introduced me to fiber-optics and presented me the strength of theory-based approach. Further, Tomáš Martan, who was at the begining of the SC-MOF sensing development and Bryan Nelsen who had an impact on the way I was thinking about optics as well as many people from the ELMAG department, thank you.

Special thanks goes to my family who supported me deeply from the beginning as well as my girlfriend and Mr. A.

Abbreviations

- DNA - deoxyribonucleic acid

- FD-BPM - finite difference – beam propagation method

- FEM - finite element method

- FFT - fast Fourier transform

- FBG - fiber Bragg grating

- HC-MOF - hollow core microstructured optical fiber

- LPG - long-period fiber grating

- mPOF - microstructured plastic optical fiber

- MFD - mode field diameter

- MIR - mid-infrared

- MOF - microstructured optical fiber

- NIR - near-infrared

- POF - plastic optical fiber

- RI - refractive index

- SC-MOF - suspended-core MOF

- SMF - single-mode fiber

- SMF - single-mode fiber

- SPR - surface plasmon resonance

- TIR - total internal reflection

- TOF - tapered optical fiber

- ZBLAN - heavy metal fluoride glasses ($ZrF_4 - BaF_2 - LaF_3 - AlF_3 - NaF$)

Contents

1. Introduction

The main research interests in the field of fiber optics have been shifting in the last decade, from pure communication topics towards sensing areas. Optical fibers can offer many advantages when compared to other, mostly electronic, sensors including mechanical and chemical resistance, low weight and low cost. These advantages allow optical fibers to be used in demanding and hazardous environments, and are especially useful in environments where electric spark can cause explosion, or in electromagnetic interference sensitive scenarios. Optical fibers, at the same time, can act as physical sensors (temperature, pressure, electrical field, humidity or refractive index), or can be used for object detection (bio-samples or molecular detection) [1]. Thanks to the combination of the abovementioned advantages, fiber-optic sensors have become widely used in petrochemistry, biochemistry, automotive industry, construction etc.

Since conventional telecommunication fibers do not often provide sufficient sensor sensitivity, the optical fiber is frequently modified for specific sensing purposes, or a new type of an optical fiber is developed. To analyze the refractive index of the surrounding environment, the evanescent-wave principle is commonly exploited. Geometric modifications of an optical fiber, lead to increased sensitivity and allow for specialized sensor applications [2]. Secondly, various fiber glass materials, shape-tailoring or inner fiber structure design can be used to provide enhanced sensor parameters, bearing in mind the final implementation and design.

The core of this dissertation thesis is focused on analyte detection techniques based on specialty optical fibers. To increase sensor sensitivity and to provide liquid analyte detection in hazardous environments, the refractometric sensing principle has been selected owing to its ability to detect various liquid analytes in an easy and effective way. Refractometric sensing is a promising approach for controlling liquid mixtures, measuring the concentration, or detecting the presence of the target analyte, and can be used in many industrial areas. To achieve enhanced sensor sensitivity, two approaches have been selected. First, the thesis focuses on the geometric modification of the optical fiber. Tapered optical fibers (TOFs) have been chosen in order to optimise the design and the fabrication process to achieve the highest sensitivity. The second focus of the thesis is on the inner structure modification in terms of microstructured optical fibers (MOFs). Suspended-core MOFs (SC-MOFs) have been designed, measured and, ultimately, a new approach of SC-MOF refractometric sensing has been proposed.

In the first part of the doctoral thesis, the state of the art of fiber-based sensing is presented, containing an overview of sensing techniques used for analyte detection.

Refractive index (RI) sensing approaches are outlined with a focus on TOFs and SC-MOFs. In the second part of the thesis the objective of the thesis is defined and achieved results in journal papers are presented with a description summarizing their contribution and relevance to the thesis topic. In the end, the achieved results and the possibilities of possible further research extensions are summarized.

2. State of the art

Optical fiber sensing is one of the most promising areas in the field of fiber optics and is in a state of constant development. This chapter first discusses the most common analyte detection principles to provide an introduction to the physical phenomena based on fiber optics. In the following two chapters the state of the art of analyte sensing via TOF and SC-MOF is thoroughly described. The theoretical background, followed by the fabrication process, is presented, furthermore, measurement setups, methods, and achieved results are discussed.

2.1 Analyte detection techniques

Based on diverse quantum phenomena, many analyte sensing approaches have been studied. Each approach exploits different properties of analytes and can be used in specific fields of application. The key sensor differences are their spectral range, sensitivity, robustness and demands on fiber sensor design.

Attenuation-based optical fiber sensing

Attenuation-based detection is an elementary technique, easy to use and implement. Generally, light is transmitted through the analyte, resulting in attenuation. This attenuation is dependent on the interaction length with the analyte and analyte characteristics, typically refractive index. Sensors exploiting this technique are utilized either in the transmissive or reflective regime.

Many variants of attenuation-based techniques have been presented to improve sensitivity performance and extend their use. One way to enhance sensitivity is to bend the fiber to change the total internal reflection (TIR) condition between the fiber and the surrounding environment (liquid analyte). Alternatively, using D-shaped or polished fibers [3], [4] evanescent-wave will expand more into the liquid analyte increasing sensitivity. Similarly, fibers with chemically removed coating [5], enable increased evanescent-wave penetration into the liquid analyte in dependence on the analyte RI. Tapering various fibers will result in TOFs, which have enhanced evanescent-wave, described in more detail in Chapter 2.2.1. Alternatively, MOFs, where due to a very small core diameter the evanescent-wave is significantly overlapping into the air-holes, allowing high interaction with the liquid analyte as described in Chapter 2.2.2.

Generally, the attenuation method is useful for detecting the presence of analytes, and refractometric sensing. Based on attenuation also spectroscopic analysis can be used

to observe the absorption of a particular liquid analyte at various wavelengths. This method determines not only RI and the presence of liquid, but is able to determine the liquid analyte's exact composition [6]. Usually, mid-infrared spectroscopy is used in the MIR, where region the strongest absorption bands can be found. The spectral limitation is posed by fiber glass materials. Silica needs to be substituted by MIR transmissive glasses, such as fluoride, sulfide or telluride glasses.

Fluorescence

Fluorescence is a kind of photo-luminescence, where a unique spectrum fingerprint is generated, based on each material's specific electron orbit structure, which leads to the determination of the exact material. In principle an electron is excited by an incident light to a higher energy level and when it falls back, it emits light of a given wavelength strictly according to the exact material as depicted in Fig. 2.1. This method is highly accurate and determining when compared to other sensing methods. This is often used for an analyte-mixture measurement where two or more analytes are included. Additionally, fluorescence lifetime (1-100 nm) can be measured and serves as a form of liquid analyte determination represented by the time of electrons staying excited.

Optical fibers can be doped or covered by specific materials allowing sensitivity to sensor surroundings, such as temperature [7]–[9] or humidity [10] and they can be used in many other applications, including food quality [11] or gas concentration measurements [12], while retaining the advantages of optical fiber.
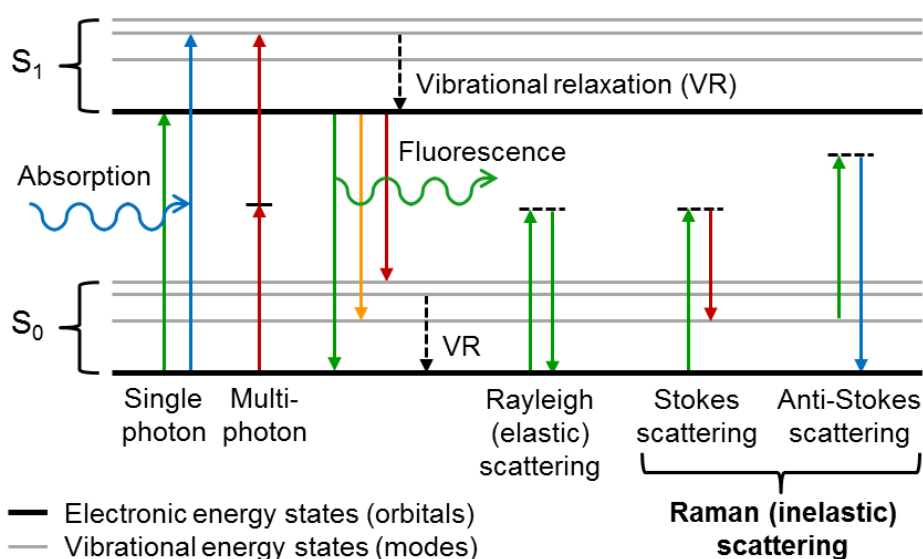

Figure 2.1: Visualization of quantum phenomena in an analyte, representing different detection techniques described in this chapter (Absorption, Fluorescent, and Raman sensing) [13].

Raman spectroscopy

Raman spectroscopy is in contrast to the fluorescence technique a non-resonant (inelastic) process. A photon is excited and released from a non-resonance energy level in conjunction with Stokes and Anti-Stokes scattering. This process is shown in Fig. 2.1. The wavelength shift between excited and emitted photons carries information on electron levels characteristic of each analyte. This method is supplementary to IR spectroscopy as the intensity of bands is usually inverse. The virtual states causing the Raman effect do not depend on the wavelength of excitation and an arbitrary source can be used. To avoid resonance wavelength, where the Fluorescence causes additional noise, a wavelength such as UV (photons often do not have enough energy to excite to resonant levels) or IR/NIR (fluorescent energy is widely separated in the spectrum) are commonly preferred.

Raman spectroscopy boasts a wide array of applications in the fields of medicine, safety, and biology: it detects explosive materials [14] and miniscule amounts of drugs [15]; verifies the origin of a piece of art or the layers of materials in a piece of art [16]; detects major species in natural gas [17]. Other applications can be found in the fields of food safety [18] or criminalistics [19].

Surface plasmon resonance

Surface plasmon resonance (SPR), or localized plasmon resonance, is based on surface plasmon polaritons which are represented by transverse magnetic waves propagating along the transition between materials with positive and negative permittivity (e.g., metal and dielectric). Metallic layers (50-100 nm) or metallic nanoparticles deposited on the substrate surface enable us to investigate particles from the surrounding environment and are designed to capture these particles on the surface greatly increasing the selectivity and sensitivity of this sensor. The SPR condition is strongly sensitive to surrounding RI, which could be used for real-time monitoring in bio-sensing and biochemistry.

Localized SPR usually uses metal nanoparticles coated on a glass substrate, whereas SPR works with a metal film coated on a prism as compared in [20]. The RI is usually changed by the presence of molecules, including proteins and DNA. The material layers can be deposited on a part of the fiber and on a flat surface, as presented by Homola [21]. The metalic sensing layer replaces the cladding of the fiber which can be partially removed by side polishing as presented by Ahn [22]. Ahn also studied the tuning of resonant wavelength, from VIS up to IR, based on a combination of metallic and dielectric layers.

Many sensor configurations have been presented regarding shape-tailored fibers: TOF for SPR sensing is described in [23], U-bent fibers in [24], fiber dip in [25] as well as its application inside of MOF [26] and others [27]. SPR methods can be highly selective, but

appropriate functional layer materials must be designed [28] for specific applications which makes this process more complex and more selective. With an eye on mass production, the design requires a low-cost solution putting demands on established fabrication processes, with respect to the costs of materials and the fabrication process.

2.2   Selected refractometric sensing techniques

Refractometric sensing is a promising area for detecting liquid or gas analytes. As an example, the quality of liquid mixtures can be controlled. This is useful in industry, laboratories or in everyday use where a specific product or liquid mixture is desired. Using this method also analyte presence can be detected or one can also identify the evaporation rate, liquid level and, in more advanced methods, presence of specific particles in the liquid analyte.

Refractometry is an analytical method leading to analyte RI determination which is a fundamental material property. The RI of the analyte is dependent on its temperature, wavelength and density [29], which has to be taken into account. In most literature, RI of analyte is determined and well-described at 589.3 nm (sodium D-line). For extended range RI equations are also available [30], [31]. Concerning temperature influence on liquid analyte RI, usually room temperature (20 ^{o}C) is assumed to be the case. In literature a broader temperature range [32] can be found, describing the RI effect on specific measurements. In refractometric sensing a second probe, or software post-processing, is frequently used to eliminate the effect of temperature.

Many approaches have been presented for fiber based RI sensing. The most commonly used methods are based on spectral shift, amplitude modulation, carrier phase tracking, fringe visibility, and Fast Fourier transform (FFT) analysis [33].

Due to its ability to detect various liquid analytes in an easy and effective way, the attenuation-based refractometric sensing principle has been selected as the core of this thesis. Since conventional optical fiber often provides insufficient sensitivity when used as a sensor, two approaches have been selected to achieve enhanced sensor sensitivity. First, TOFs are used for their increased evanescent-wave overlap, with the focus on TOF design, fabrication process, the improvement of TOF sensing parameters. Secondly, MOFs have been evaluated, especially those with an enhanced evanescent-wave overlap into the cladding air-holes. Suspended-core MOFs (SC-MOFs) were designed, drawn, measured and a new approach to SC-MOF refractometric sensing has been proposed.

Various approaches of RI measurement have been, up to now, widely studied and reviewed e.g. in [33], [34], from which the most relevant papers to my research (TOF and SC-MOF sensing) are presented in detail in following Chapters 2.2.1 and 2.2.2

2.2.1   Detection of liquids with tapered optical fibers

To increase the detection sensitivity of optical fibers, many modifications and adaptations have been developed. One of the most effective and robust is optical fiber tapering [35], which significantly increases the sensitivity of the optical fiber-based sensor and no additional coupling system is required. The process of optical fiber tapering represents a reduction of fiber diameter achieved by the lateral stretching of the fiber while it is heated. For thin TOFs, energy from fiber core exceeds out of the fiber into surrounding environment, in form of evanescent-wave, which allow the detection of attached analyte. The increased evanescent-wave is acquired for thin TOFs, which increases sensitivity. As Tong showed [36], low-loss waveguiding is also possible, even for TOF core diameters of hundreds of nanometers, with certain conditions such as high RI contrast between the TOF core and cladding. The smaller the TOF core diameter, the higher dimension uniformity and sidewall smoothness is required, otherwise losses occur. In the following text, the focus is placed on TOF sensors for the detection of liquid analytes with some additional gas detection schemes showing basic principles and measurement configurations.

TOF sensing principle and fabrication

A TOF schematic side-view is depicted in Fig. 2.2. In area l_1 and l_2, which is tapered area, evanescent-wave penetrates into the surrounding material. Taper waist diameter, as a key factor of tapering, represents l_1 thickness. Area l_3 could be connectorized, and connected to conventional fibers, leading the light to and from the tapered area.
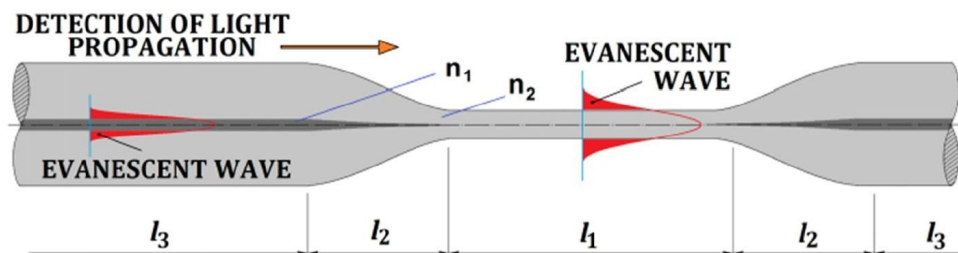

Figure 2.2: TOF profile. Tapered optical fiber cut, with evanescent-wave, overlapping into the cladding and surrounding analyte, where l_1 is the taper waist length, l_2 represents the transition part of TOF, and l_3 is the un-tapered part of the TOF [37].

The evanescent-wave is sensitive to external refractive index, depicted in Fig. 2.2. The characteristic penetration depth of such light is given by [38]:

$$d_p = \frac{\lambda}{4\pi}(n_{core}^2 sin^2\phi_{init} - n_{clad}^2)^{-1/2}, \qquad (2.1)$$

where ϕ_{init} is the incident angle (from a normal core-cladding interface) for single-mode

fibers and it varies for higher modes: λ is the wavelength, n_{core} and n_{clad} are refractive indices for the core and cladding respectively.

Silica TOFs are commonly fabricated by heating the target fiber at one point while drawing to both sides. The longer the drawing length, the thinner the taper waist. The drawing scheme is depicted in Fig. 2.3 where two translation stages controlled by direct current motors draw the fiber while it is simultaneously rotated and heated. A heat of 1710 ^{o}C must be reached as this is the melting point of silica. Rotation brackets allow fiber rotation and drawing. Drawing speed is in micrometers per second, based on the heating source and material properties of the fiber. As for the heating source, we can use a hydrogen flame, resistance furnace or CO_2 laser. CO_2 focused on one spot which is heated, in contrast to the flame technique where the heated area is larger.
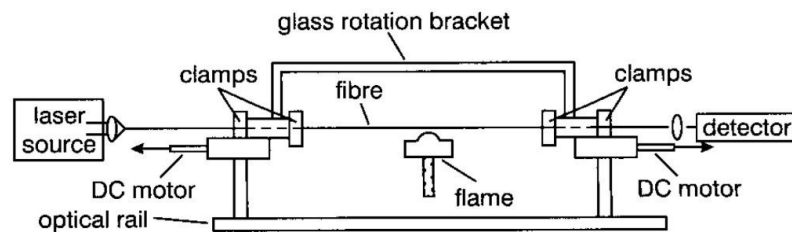

Figure 2.3: Schematic of a drawing rig for the fabrication of TOFs [39].

During the flame method [40] the stability of the flame is crucial, as is ensuring a clean-burning process to avoid the risk of depositing material on the fiber surface. Not only is a static flame used, but a brushed flame method [41] could also be applied when the flame is moving along the length of the TOF which cedes more control to the tapering process by using speed and a particular length of motion. Compared to this, a CO_2 laser [42] provides a clean and effective heat source with stable heating power and control. The heating temperature is controlled by focusing the laser beam. This method is limited by the temperature gradient around the CO_2 heating spot, which must be compensated by, or substituted by, indirect heating where the capillaries surrounded the fiber are heated by CO_2. Similarly, electrical resistance heating systems [43] have been developed. Electric stripe heater performed a consistent heating system, allowing to reach ten times longer taper compared to the flame heating technique. In the end, it is critical to create a stable heating source and to design a repeatable and controllable fabrication process.

Polymer TOFs can also be fabricated and used as sensors. Polymers can be heated, though it is more common to dissolve the polymer material in a solvent, and the evaporation process causes solidification [44]. This technique of polymer TOF fabrication provides an excellent geometric profile due to the slow fabrication process.

There are two main groups of TOFs with regard to TOF attenuation: non-adiabatic and adiabatic TOFs. Non-adiabatic TOFs have excited cladding modes in the taper waist

area (*l1* depicted in Fig. 2.2), because of the steep shape of tapering when compared to length. This kind of taper is suitable for coupling in and out of the fiber, which can be used in setups based on interference [45], [46]. Compared to this, adiabatic TOFs have a slow-decreasing transition part (which is typical for longer TOFs), where no power transfer into the higher modes is present, which is also a characteristic of low TOF attenuation. These non-adiabatic and adiabatic mode transmissions are described in greater detail in [47].

To further increase sensitivity during fabrication process, various TOF functionalizations have been proposed, such as TOF grating inscription, forming cavities, knot fabrication, surface functionalization, etc. TOFs were also fabricated with asymmetrical up/down-tapering, which was tested for RI sensing [48].

Light propagation inside a TOF

The propagation inside a TOF is determined by the fiber's RI profile and the tapering geometry. The key factors for sensing are evanescent-wave penetration depth and power fraction in particular modes. The down-tapered part of the TOF causes the stable state of modes entering this area to be scattered or to be propagated along the TOF (more or less outside of the TOF) in what is known as an evanescent-wave, and their intensity decays exponentially with distance from the fiber surface in a perpendicular direction. In the waist area, the taper diameter is uniform and the penetration depth is the highest. Later, the propagating signal reaches the up-tapered transition region where signal is back-coupled into the TOF core and propagates further. If there is more than one mode present, intermodal interference occurs during back-coupling which could influence a spectral response as described in [49]. A propagation analysis of a conventional TOF has been modeled and calculated using a finite-difference beam-propagation method (FD-BPM) [50] and further expanded by taking the propagating constant into account [39]. The power loss caused by the TOF waist diameter was measured and this loss depends on the surrounding environment (especially on RI), TOF fabrication quality and TOF geometry. If the contrast of RI between the TOF and the surrounding environment is high (e.g., silica-air) and the TOF waist diameter is larger than the signal wavelength, then TOF loss is almost negligible. When the TOF waist diameter is in the scale of the signal wavelength or smaller (these fibers are called subwavelength fibers or nanowires) TOF attenuation increases. Advanced numerical methods are also used for TOF numerical description. Baude [51] presented a comparison between the FD-BPM and the finite element method (FEM), which included solving propagation equations and determined attenuation with respect to TOF waist diameter, waist length, and the external liquid analyte. Since the length of propagation is large with respect to the signal wavelength, the FD-BPM method is suitable. Nevertheless, the finite element method fits when the fiber

diameter changes and the curved boundaries can be effectively meshed, e.g., by triangular elements.
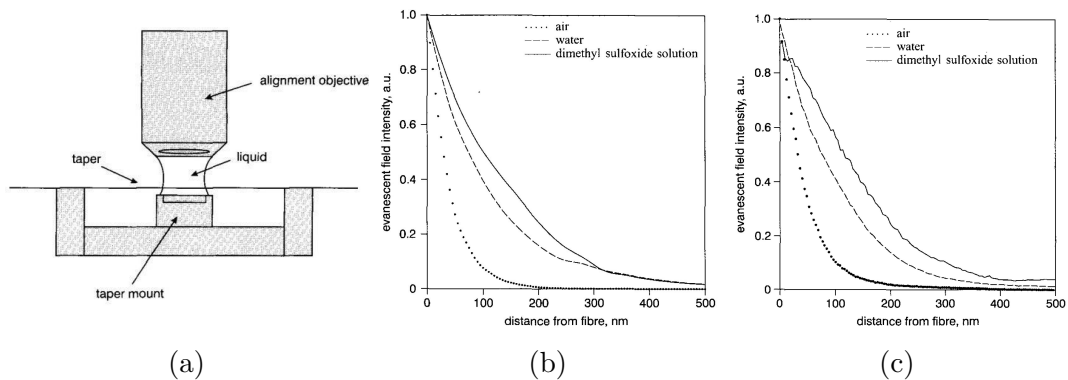

Figure 2.4: a) Mounting system used for near-field optical measurements in liquid analytes b) calculated and c) measured evanescent-wave magnitude as a function of distance from the TOF surface [39].

Huntington presented an evanescent-wave characterization of a TOF submerged in liquid analytes which were characterized by near-field scanning microscopy and atomic force microscopy [39] and, simultaneously, a longitudinal TOF shape was analyzed. An evanescent-wave penetrating air, water, and dimethyl sulfoxide solutions was recorded by a modified near-field scanning microscope as depicted in Fig. 2.4. These results were in correlation with a theoretical calculation with the FD-BPM [50]. Evanescent-wave is an important parameter for optimizing fabrication and the application process of TOFs, and may also be simulated, e.g., by COMSOL software as shown in [52]

Further, Jung [47] studied a broad range of wavelength for multi-mode and single-mode transmissions of tapered SMF-28, which is commonly used in telecommunications. By tapering its outer diameter from 125 μm down to 0.4 μm results in output power visualized in Fig. 2.5a). The step change in the power corresponds to the change in the number of modes in the optical fiber. As depicted, tapering SMF-28 to 70 μm causes interference between different modes and single mode operation e.g. for TOF around 1 μm. In Fig. 2.5a) a comparison between the transmission spectra of SMF-28 with and without 1 μm TOF is visualized simultaneously with fiber mode, which are present. The analysis of TOFs around 1 μm was especially useful due to minimal attenuation (0.1 dB at 1550 nm) while keeping the fundamental mode in the whole measured range.

TOFs with subwavelength core diameters were theoretically studied by Tong [53] who included the calculation from Maxwell's equation for silica and silicon (RI = 3.5) materials. Enhanced evanescent-wave, single-mode condition, power distribution, and mode field have been studied. The Poynting vector has been calculated to as small as a 200 nm silica TOF core diameter. TOFs having a wavelength, or subwavelength core diameter, are significantly affected by surface smoothness and core diameter uniformity. Due to
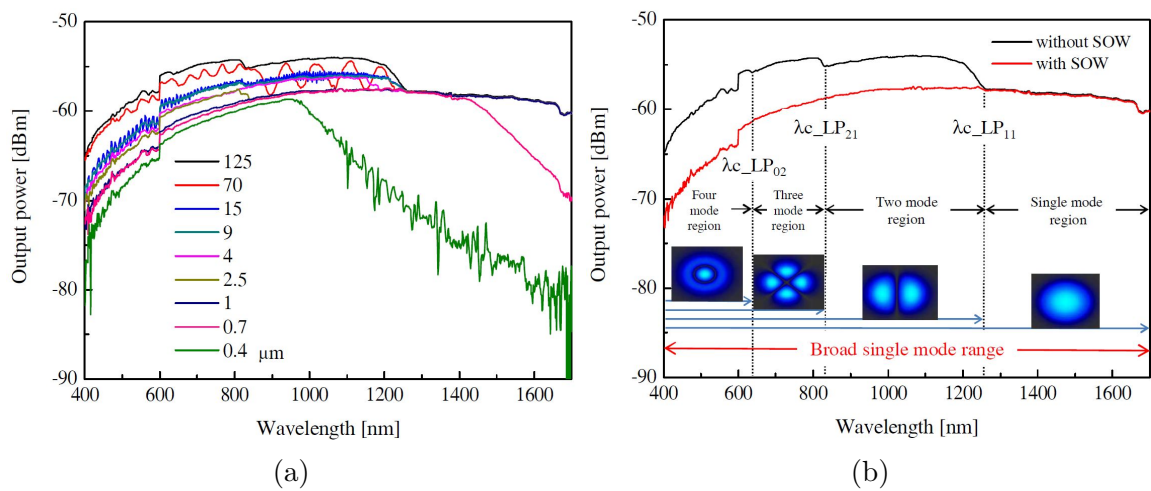
Figure 2.5: Transmission spectra of a) several down-tapered SMF-28, b) SMF-28 with a 1 μm TOF (red), in contrast to SMF-28 fiber only (black), with depicted high-order modes [47].

this, low guiding losses at these wavelengths are hard to reach. Another theoretical study dealing with the analytical expression for the intensity of the electrical field inside a small core diameter TOF was presented further by Kien [54].

Measurements setups with tapered optical fibers

Refractometric detection of liquid analytes based on tapered optical fibers has been widely studied and many measurement configurations have been proposed. There are two main groups of TOF sensors: attenuation-based; and interferometric. Interferometric TOFs provide better sensitivity and resolution, but also commonly require a more complex measurement configuration and post-processing. Furthermore, TOF sensors can be divided by the detection principle into TOF sensors based on evanescent-wave and TOF sensors based on transition regions (coupling into higher-order modes).

Polynkin [55] reported a simple and robust sensing concept for the measurement of the refractive index of liquid analytes, integrating the TOF into a soft polymer block, as depicted in Fig. 2.6a). The liquid analyte is localized in a pre-fabricated channel and separated from the TOF by a thin layer of polymer. Polymer RI is suitable for allowing the evanescent-wave to reach up to the channel and, simultaneously, protect the integrated TOF. This setup is theoretically described and mode field diameter (MFD) is simulated for a variable range of TOF waist diameters. The sensitivity of the device is presented for varying RI, using a TOF with a taper waist diameter of 1.6 μm and 0.7 μm as shown in Fig. 2.6b). The channel is filled with a solution of glycerol and water and provides a RI range of 1.311-1.459, at 1500 nm. The measured accuracy of the RI range of 1.37-1.40 is estimated to be 5x10^{-4} RIU which changes with source/detector stability and mechanical

rigidity of the TOF sensor.

Fig. 1.   Schematic side view of the sensor.

(a)   (b)
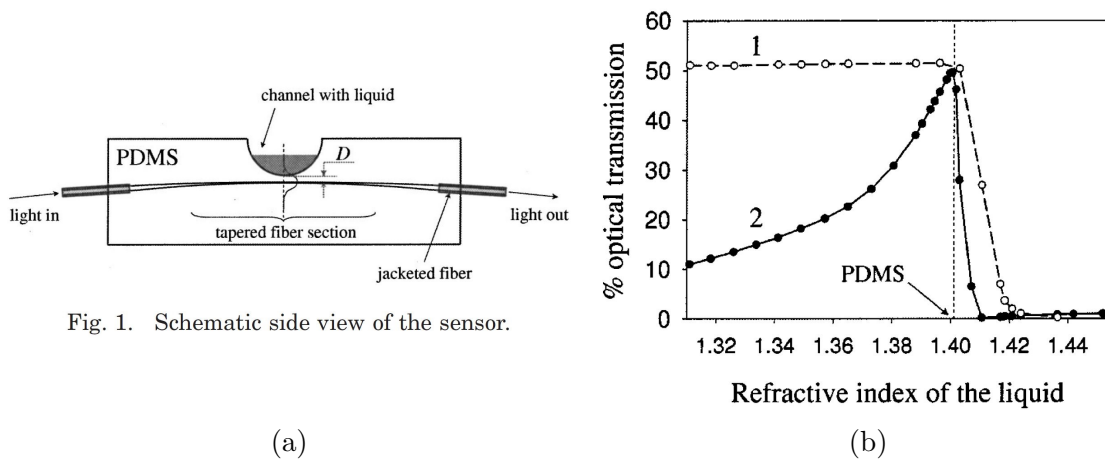
Figure 2.6: a) Schematic side view of the measurement unit with a soft polymer block containing a TOF and a channel for the liquid analyte, b) measured optical transmission through a TOF with respect to the refractive index of the selected liquid analyte for 1) 1.6 μm and 2) 0.7 μm TOF waist thickness [55].

To enhance the refractometric sensitivity of the TOF, the TOF can be further bent. Experimental results of this combination were presented by Clenilson [56] who tuned the sensitivity to the target RI range by bending the TOF to increase sensitivity around the RI of water (1.33-1.35) from 41nm/RIU up to 378.73 nm/RIU, and, at RI = 1.40, from 378.73 nm/RIU to 1506 nm/RIU, with a curvature radius of 16.5 mm.

A wide group of refractometric measurements of liquid analytes with TOFs based on interference techniques are presented in [57], [58]. Interference occurs when the core mode interferes with a higher-order mode which is out- and then in-coupled. Any change of the liquid analyte RI will result in an interference spectrum shift. Fundamental mode, and first-order cladding mode interference formed, when a non-adiabatic TOF with a waist diameter of 1.64 μm was used [59]. TOF sensor sensitivity was 980 nm/RIU in the RI range of 1.332 to 1.392. Multiple TOF sensors based on interference in biconical TOF were presented by Kieu [60]. An RI range of 1.333 to 1.350 has been simultaneously studied with the possibility of strain and temperature measurement, and sensitivity of about Δn 1.42x10^{-5} has been reached. A Mach-Zehnder interferometer was presented to measure RI and temperature simultaneously which allowed for immediate temperature compensation (compared to only RI measurements where additional temperature stabilization is required). A non-adiabatic TOF with a waist length of 1 cm and waist diameter of 83.1 μm has been fabricated. The non-adiabaticity caused multiple resonance wavelength dips and, by monitoring two of them, both parameters (RI and temperature) were determined. Resolution reached 72.21 nm/RIU [61]. Multiple sensors for the concentration of protein in water and for RI measurement have been designed using a TOF,

where out/in coupled modes caused a phase shift, in comparison to a fundamental mode, resulting in a wavelength shift of the transmitted spectrum. Sensitivity of 1500 nm/RIU was reached [62].

The above-mentioned techniques [59]–[62] require an optical spectral analyzer and complex post-processing. To avoid these, Mas [63] used a combination of TOFs and a broadband light source, as depicted in Fig. 2.7a). This approach provided equal measurement results and also simultaneous strain and RI measurement. One and two TOFs on one fiber, with waist diameters of 18 μm, served as liquid analyte sensors of ethanol deionized in water having an RI in the range of 1.3173 up to 1.3212. The achieved sensitivity for a single TOF was 907.69 dB/RIU and the sensitivity for two TOFs was 2261.53 dB/RIU, with transfer function depicted in Fig. 2.7b). A long-term stability measurement has also been conducted for 2000 seconds. The broadband source provided stability of 0.039 dB, compared to 0.139 dB for the tunable source.

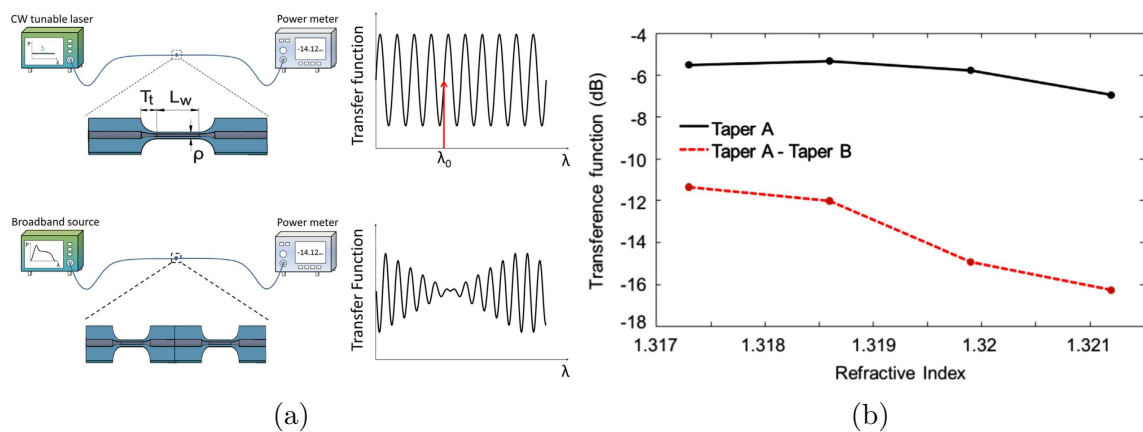(a)   (b)

Figure 2.7: a) Measurement setups for refractive index and strain measurement with a continuous wavelength tunable laser with one TOF and a broadband source with two TOFs, b) Measured RI response for one (black) and two (red) TOF measurements [63].

As mentioned in the Introduction, the temperature effects must be compensated to achieve correct results. Salceda [64] created a temperature insensitive measurement setup where the TOF waist (10 μm diameter) was connected directly to the untapered region of a conventional SMF. This transition will generate two modes, which beat to each other. This sensor is insensitive to temperature, though sensitive to the surrounding change of the RI, as shown in Fig. 2.8. Temperatures from 20 to 100 ^{o}C did not influence the RI measurement. The beat period could be set, based on the TOF waist length, which improves the resolution of the post-processing. A maximal resolution of 3.7×10^{-6} has been reached for an RI of around 1.428.

To achieve better results and to have access to additional sensing possibilities, other fibers than conventional SMF-28 can be tapered. A combination of the tapering process applied to specialty optical fibers, multiple tapering, or TOF surface functionalization
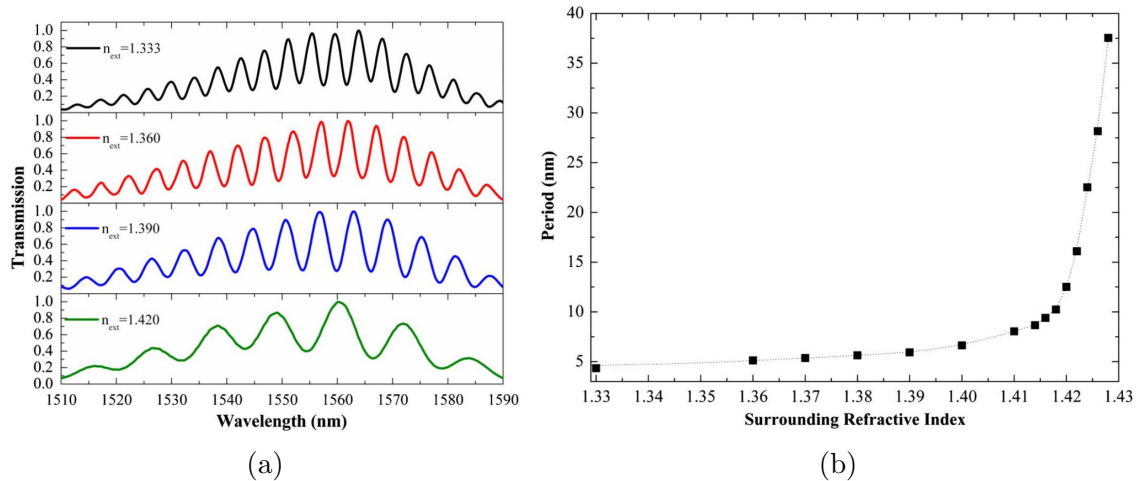
Figure 2.8: a) Normalized transmission of a TOF with waist diameter of 10 μm for various RI b) Beat period for TOF waist 30 mm long and 10 μm in diameter [64].

can provide enhanced sensitivities, increased and measurement range. The advantages of tapering of specialty optical fibers have been studied and MOFs have been tapered [65], [66] to increase the detection sensitivity either with or without collapsing air-holes in the taper area. Nguyen [66] described the fundamental properties and characterization techniques of a tapered MOF. The fiber tapering process and its non-destructive probing of the fiber profile have been described, as well as fundamental mode attenuation and transmission properties. Tapering SC-MOF up to its waist diameter, from 125 μm down to 31.25 μm, increased the evanescent-wave overlap from 0.84% up to 29.16%, which has been simulated and further verified by fabricating an adiabatic TOFs [65]. The influence of tapering and water filling has been theoretically studied in terms of the transmission spectrum, influence on MFD and confinement loss.

Studies of the advantages of plastic optical fiber (POF) have been conducted. POF provide low attenuation in the visible region, larger core diameter and high numerical aperture, which led to higher signal in- and out- coupling efficiency. Microstructured POF (mPOF) has been studied theoretically and experimentally [67], for an RI range of 1.33 to 1.45, and with temperature dependent bending loss. Further, Teng [68] fabricated a tapered POF with macro-bending applied for higher sensitivity. As shown in Fig. 2.9a), the temperature was controlled with a digital thermometer as the thermo-optics coefficient is one order higher than that of silica fibers [69]. An RI range from 1.33 to 1.41 has been measured and temperature dependency was analyzed (see Fig. 2.9b). The thermo-optic coefficient has been derived, as well as the influence of fiber tapering and U-bending.

A POF taper working as a biosensor was published by Beres [70] who used the sensor to detect the presence of variable cells and bacteria (Candida guilliermondii and Escherichia coli) in water. This sensor can be used as a monitoring device against chemical threats.

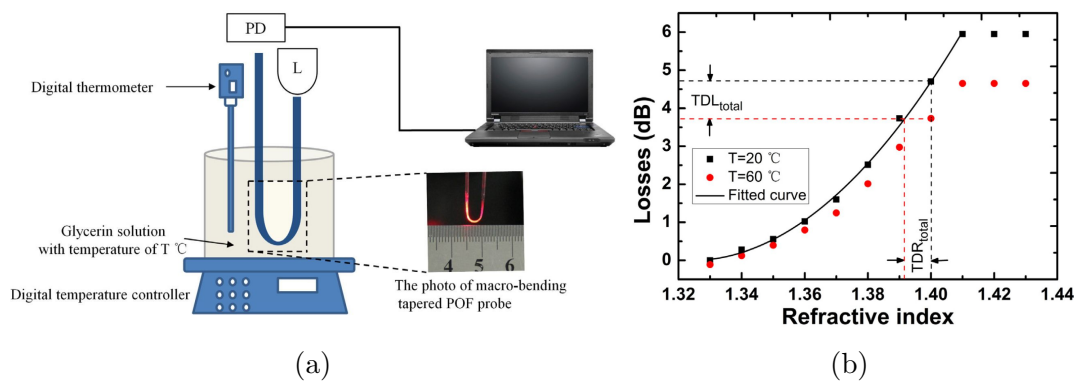(a)   (b)

Figure 2.9: a) Experimental setup for RI measurement with tapered POF, where L is the laser and PD is the photodiode b) Propagation loss dependent on the RI of the liquid analyte with respect to two temperatures [68].

A U-shaped tapered POF has been studied with an RI range from 1.33 to 1.45. Achieved sensitivity was 6.1 mV/10^{-3} RIU and 12.1 mV/10^{-3} RIU for a straight and U-shaped taper, respectively. Several experiments were carried out to functionalize the surface of TOFs to provide better performance. One of the most promising methods, SPR, has also been applied to TOFs [71]. A gold layer (estimated at ±24 nm) on a tapered SMF-28 caused a localized SPR which transduced the change of the surrounding liquid analyte RI into the spectral response of the TOF sensor. The RI resolution reached 51 nm/RIU at the wavelength of 537 nm. With respect to the light source, detector and averaging, sensitivity has been estimated at 3.7×10^{-5} RIU. Direct real-time measurement of absorbance has been realized and the result is depicted in Fig. 2.10b) for sucrose solutions with various RIs ranging from 1.333 to 1.403. The resolution of the intensity-based sensor has reached 3.2×10^{-5} RIU. Further, the purification process, as well as biomolecular interactions, are described. SPR methods can be highly selective, but the design must be adapted according to the desired liquid analyte or the biomolecular and multi-step production process.

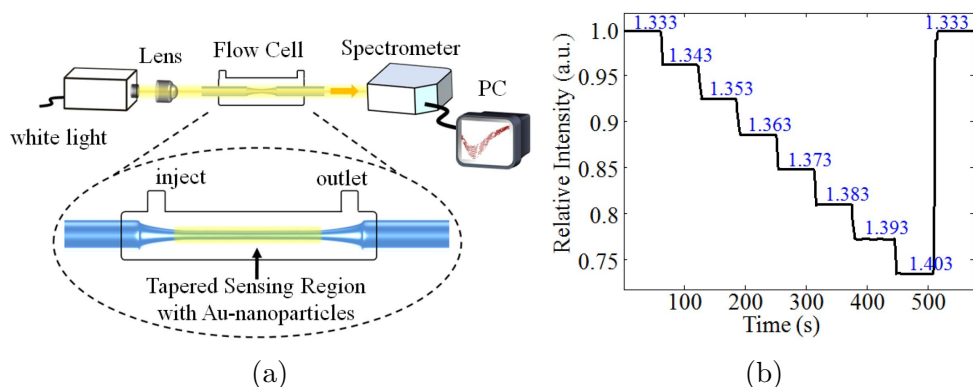(a)   (b)

Figure 2.10: a) Measurement setup containing a TOF with gold nanoparticles inside the flow cell introduces a liquid analyte to the TOF and allows the coupling inside or outside the TOF, b) recorded transmitted light intensity for various RI of liquid analytes [71].

2.2.2 Detection of liquids with suspended-core microstructured optical fibers

In 1993 E. Yablonovitch [72] realized that there is an analogy between electromagnetic wave propagation in multidimensional periodic structures and electron-wave propagation in crystals, which later led to the first photonic band-gap structures. This idea was further pursued by P. J. Russell's research group and resulted in the development of a new type of optical fiber: the microstructured optical fiber [73]. Thanks to the extreme variability of MOF structure design, transmission parameters such as attenuation, dispersion, zero-dispersion wavelength, numerical aperture, and mode-field diameter can be tailored for a target purpose. This is the main advantage of MOFs which has led to a wide range of applications.

The MOF manufacturing process is usually accomplished by the stack-and-draw technique [73], [74] where the hollow capillaries are placed into a jacket tube forming the perform, then later drawn into the final MOF. Glass capillaries are fabricated separately and could have different diameters, shapes (determines later pitch and a hole diameter of the fiber lattice) or can be doped or covered for specific properties. The target capillary could be filled by a glass material creating a multiple-core fiber which can also be used for sensing purposes. The stack-and-draw technique equipment is low-cost, but due to the complexity of the pressure setup during the preform drawing, an alternative method based on ultrasonic drilling [75] was developed to allow air-holes to be created more precisely. This alternative technique is extremely precise but needs a lengthy working time. The extrusion method was presented [76] and is suitable for small-core, large air-filled holes. The glass is under high pressure and temperature to create the preform from the microstructure matrix.

MOFs have been fabricated from a wide range of glass materials, including conventional silica glass [6], [77], lead-silicate glasses [36], tellurite glass [78] and bismuth glass [75] and even instead of glass using a polymer [79]. The choice of glass material, with regard to MOF structure, allows the tailoring of the operating wavelength, transmission window, dispersion curve, fiber effective/refractive index or fiber nonlinearity. Based on the core material, the MOF can be divided into: a) a solid-core MOF (with special case of a suspended-core MOF) and b) a hollow-core MOF, all depicted in Fig. 2.11.

Solid-core MOFs (Fig. 2.11a,b) have a solid glass-material core surrounded by concentric rows of air-holes, creating a lower effective refractive index of the cladding. Solid-core MOFs hold the light in the core due to the principle of modified total internal reflection (MTIR [74], [80]) close to the guiding mechanism of conventional core/clad fibers. Compared to hollow-core MOFs, they provide single-mode guidance and exhibit attenuation

as low as 0.18 dB km^{-1} [81]. A special type of solid-core MOF, with steering-wheel shape of solid-core, is the suspended-core MOF (denominated in this thesis as SC-MOF), which will be discussed later in greater detail.
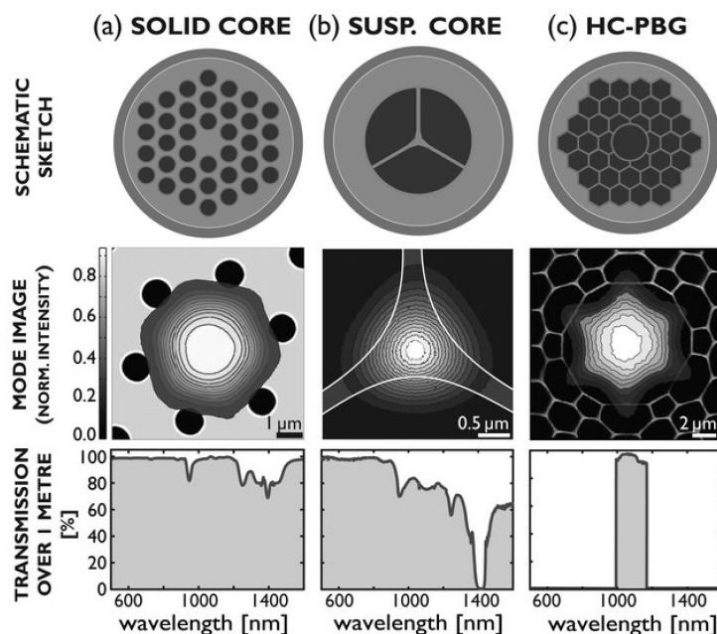

Figure 2.11: From top to bottom: schematic representation of MOF geometry; fundamental optical mode guided in the core of the fiber and transmission over one meter of fiber for (a) a solid-core MOF; (b) an SC-MOF; (c) an HC-MOF [82].

In hollow-core microstructured optical fibers (HC-MOFs), contrary to solid-core MOFs, light propagates in an air-core surrounded by a periodical photonic band-gap structure which holds light inside the core area of a lower refractive index, as depicted in Fig. 2.11c). HC-MOFs are less sensitive to fiber bends and they provide a few hundred nanometer-wide transmission windows with attenuation as low as 1.2 dB/km [82]. HCFs transmit light even at wavelengths where silica glass is highly absorptive (above 2000 nm) thanks to light propagation occurring almost entirely in the air. HC-MOFs can be used for sensing application purposes and for high-power signal guiding, as well as high-speed data transmission with low latency. HC-MOFs enable analyte detection thanks to the air-core which can be easily filled.

Among MOFs, SC-MOFs have two interesting advantages when developing refractometric sensors: a) they provide significantly higher overlap of the evanescent-wave; and b) in contrast to other MOFs mentioned, they have significantly larger air-holes which are convenient for easy liquid filling. The light guiding effect of the MTIR is applied to SC-MOFs. To detect an arbitrary analyte with the SC-MOF, the analyte has to interact with the evanescent-wave of transmitted light. The ability to fill various materials, such as liquids, gases, metals or even semiconductors has been reported [83]. Filling the

SC-MOF can be realized either by the SC-MOF itself, or, by modifying the measurement setup. Gases, as well as liquids, can be filled via diffusion or, even more effectively, using a pressure pump once the SC-MOF end-face is mounted in a cell [6], [78]. Liquid analytes can fill the SC-MOF by capillary forces [84]. Filling via capillary forces can be used when one fiber end is immersed in the liquid analyte [85], which must be done without compromising the fiber guidance or robustness. Alternatively, to avoid any entry or exit of the liquid analyte at the end-faces of the SC-MOF, Cordeiro presented a lateral access to the longitudinal dimension of the air-holes of SC-MOF [86], [87] as depicted in Fig. 2.12a,b) and Warren and Cox presented exposed-core SC-MOF [88], [89]. Lateral access is achieved by simultaneously increasing the air pressure in the SC-MOF air-holes and melting the SC-MOF glass material by applying an electric arc. Another approach creating a lateral access was demonstrated by precisely focusing an ion beam to the external jacket of the fiber. A rectangle hole of about 20 x 5 μm was milled, making it possible to monitor the structure with SEM imaging of this beam at the same time as depicted in Fig. 2.12a,b). The filling of selected holes with different liquid analytes was presented.

(a)   (b)   (c)   (d)
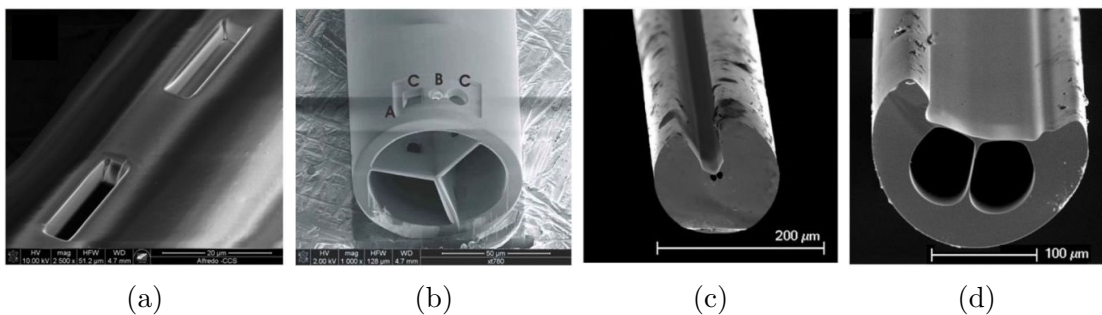
Figure 2.12: a/b) SC-MOF tip with holes formed by an ion beam [86], c/d) extraction used for fabricating asymmetric SC-MOF structures [90].

The first demonstration of an exposed-core polymer SC-MOF was carried out by creating an opening at the preform stage of the fiber fabrication [88]. The preform opening was reached by drilling holes into the cladding and long lengths of exposed-core were achieved. Similarly, micro-channels were fabricated by using silica SC-MOFs in a single air-hole by femtosecond laser drilling [91], and subsequently used to measure acetylene diffusion. The possibility of further evolution to microfluidic devices was discussed. Another long-length exposed-core fabrication process was presented in [89] by creating (blowing) a hole in the SC-MOF cladding (using a fusion splicer and pressure application), where the extraction was used for the fabrication of asymmetric SC-MOF structures (Fig. 2.12b), ultimately being used for real-time fluorescence sensing.

Mode power fraction within the air-hole of the SC-MOF is an important parameter and will significantly decrease with smaller SC-MOF core diameter. Core diameters as small as 1.7 μm have been demonstrated previously for silica exposed-core SC-MOF [90],

[92] as can be seen in Fig. 2.12c) d), however, the attenuation of these SC-MOFs was pro-
hibitively high. Recently, the fabrication process of low-loss, small-core exposed-core silica
SC-MOFs was demonstrated [93] by employing the drilling technique. Fabrication pro-
cedure and fiber design modification enabled high evanescent-wave overlap while keeping
low attenuation from the perspective of the sensing application. Various articles were pre-
sented on the selective filling of SC-MOF fibers [94] by filling other holes via UV curing
of epoxy and cutting it out after filling as shown in Fig. 2.13a). A similar technique was
used by blocking air-holes with a polymer or collapsing the air-holes to perform selective
filling [95]. Two methods were proposed by Wang [96]: a) carving a hole into the side
of an MOF to expose the same air holes as a femtosecond laser, later filled by capillary
forces with the redundant part of the fiber cleaved; and b) laser drilling into a silica mask
as depicted in Fig. 2.13b).

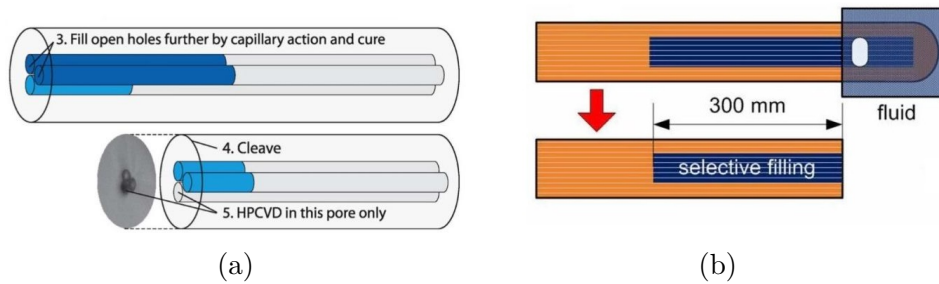(a)   (b)

Figure 2.13: Selective filling of an SC-MOF by a) UV curing of epoxy inside of additional
air-holes [94], b) Carving a hole into an MOF and selectively-filled by capillary forces
which are subsequently cleaved [96].

Recently, the use of the drilling technique to fabricate a new structure of an exposed-
core SC-MOF was presented [93]. As mentioned earlier, low-loss and good mechanical
strength were achieved for an enhanced SC-MOF sensor application. Spectral attenua-
tion for a small core SC-MOF was measured (1.65 - 2.08 μm), presenting an increase in
confinement loss with increasing strut thickness and decreasing air-hole size. An SC-MOF
with sub-wavelength core diameter was fabricated and investigated in [97]. First, by the
tapering of an SC-MOF and, later, on nanowires. SC-MOF design parameters and the
influence of the selected glass material on optical field behavior of guided modes were
studied using a full vectorial FEM approach and several liquid-analyte filled SC-MOFs
were theoretically analyzed in terms of single-mode guidance and mode power fraction [98].

Surface functionalization could significantly increase sensitivity as presented by Maz-
horova [99]. Mazhorova deposited phages onto the core surface of an SC-MOF to detect
E.coli bacteria by spectroscopic absorption of transmitted THz light. Detection at con-
centrations in the range of 104-109 cfu/ml has been reached.

Suspended-core MOF sensors

As mentioned above a fraction of the optical field extends via evanescent-wave into the SC-MOF air-holes. This evanescent-wave is used for the sensing of analytes, which are filled in the SC-MOF air-holes. Long interaction lengths of SC-MOF allow detect even gases and liquids having low RI, and at the same time a small air-holes require only a tiny amount of the analyte sample. Numerous measurement concepts have been reported during the last decade and the most relevant will be mentioned.

A SC-MOF for sensing purposes was first presented in 2001 [100]. Concerning the aim of analyte sensing applications, the SC-MOFs were early designed and theoretically described especially for this purpose by several research groups [78], [101], [102].

One of the first complex steering-wheel type SC-MOF sensors was presented in [77]. A drilling technique was used to fabricate 3 air-holes surrounding the core. A mode overlap of over 29%, as a key parameter for sensitivity was calculated with FEM software for an SC-MOF for a core diameter of 0.8 μm. This SC-MOF was studied and simulated using FEM-based software. Further, several measurements with the setup depicted in Fig. 2.14 have been realized. The signal from/to SC-MOF was launched/collected by a multi-mode fiber. The SC-MOF filling system contains a gas cell, where the gas was allocated and, due to diffusion, penetrated into the SC-MOF. As an example, the absorption of acetylene was recorded for near-IR wavelengths. Such a combination of a filling and coupling system for the refractometric sensing of analytes was first presented for SC-MOFs.
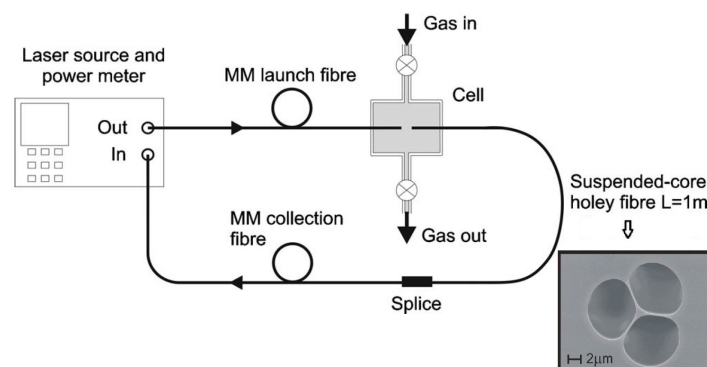

Figure 2.14: Scheme for gas analyte measurements with a unique combination of filling and coupling into an SC-MOF with (inset) an SEM picture of an SC-MOF [77].

A fully-filled SC-MOF located in a water cell was used to investigate the purity of water [6]. The purity of water was investigated and 21 mm of $NiCl_2$ caused the attenuation of the sensor of about 4.3 dB (107cm of SC-MOF, containing 1 μl analyte) in contrast to standard cuvette measurements (1 cm long) which provide attenuation of only 0.4 dB. A schematic picture of the measurement setup with unique water cells is presented in Fig. 2.15a). Normalized results are depicted in Fig. 2.15b). This work was presented

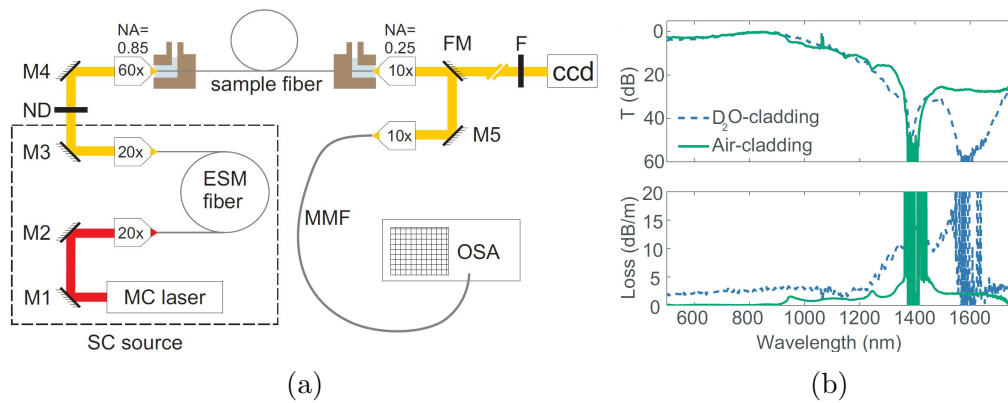(a)   (b)

Figure 2.15: a) Schematic of the setup. Supercontinuum source (SC) light is in/out collimated into the core of SC-MOF. Both SC-MOF ends are uniquely mounted into water cells. CCD beam profile camera (CCD) and optical spectrum analyzer (OSA) analyze fiber output. b) Transmission and loss spectra for 2.9m long SC-MOF filled by air (solid green) and selected liquid (dashed blue) [6].

by Euser whose team was the first to fabricate SC-MOFs, with core diameters from 0.8 up to 3.0 μm, capable of guiding light from 500 nm – 1750 nm with losses below 0.2 dB/m at 500 – 900 nm. These SC-MOFs were used [6] for the broadband spectroscopic detection of a selected liquid analyte. Based on this spectral measurement, a critical wavelength of around 1600 nm was found where the measurement setup is highly sensitive to the presence of liquid analyte inside an SC-MOF, but a broadband spectral source and spectrometer was required for this measurement configuration. For core diameters 0.8 up to 3.0 μm the mode power fraction in cladding, with respect to the wavelength (400-1200 nm) and core diameter (up to 2.2 μm), was analyzed by FEM simulations. Sample results for a wavelength of 1000 nm are shown in Fig. 2.16a), where the MFD starts to significantly overlap the air-holes (compared to 700 nm, where the overlap is negligible). The longer the wavelength and the smaller the core diameter, the greater was the mode power fraction in the liquid analyte. Absorbance spectrum of an aqueous

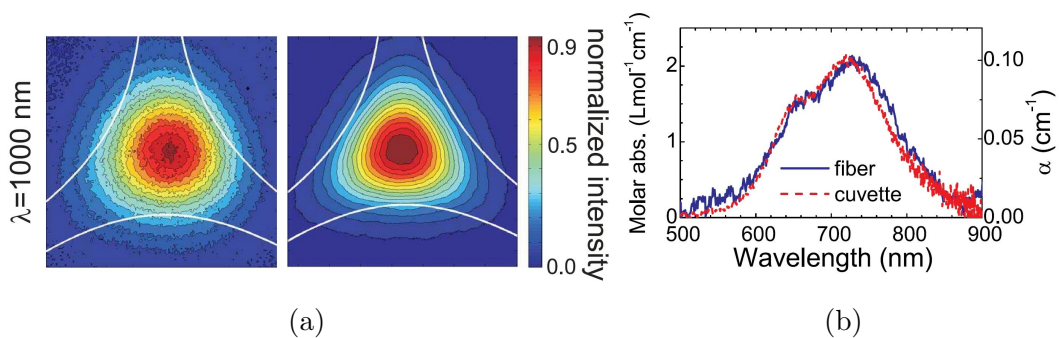(a)   (b)

Figure 2.16: a) Calculated and measured mode in SC-MOF at 1000 nm b) Absorbance spectrum normalized to the length between cuvette and SC-MOF, where α is the absorption coefficient [6].

solution, normalized to water reference has been presented in Fig. 2.16b). Furthermore, a comparison using FEM calculations was carried out and compared to measurements of an SC-MOF mode profile.

The spectroscopic approach was further extended by the direct-coupling of vertical-emitting laser and gas sensor characterization in the range of 763 - 2004 nm [103] and the spectral background of the SC-MOF was determined for the selected analyte. This was further applied to photochemistry based on HC-MOFs where absorption in the spectrum was monitored [104].

First, real-time chemical sensing with a polymer SC-MOF was presented by Cox [88], where the SC-MOF core was exposed Fig. 2.17a,b) and the liquid analyte interacted with the evanescent-wave directly along the whole SC-MOF length. Even more, the SC-MOF core could be easily functionalized. Evanescent-wave absorption spectroscopy was presented with the highest sensitivity around the wavelength at 620 nm. The presence of NaOH and HCl in water was measured. Used SC-MOF and pH presence measurement is visualized in Fig. 2.17c).

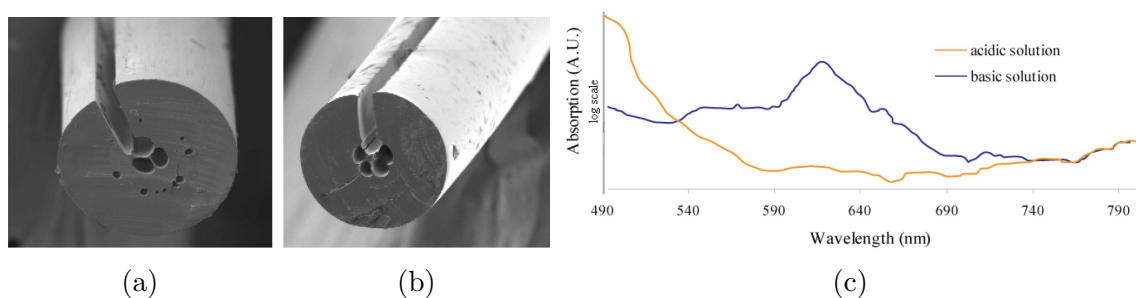| (a) | (b) | (c) |

Figure 2.17: Real-time chemical sensing with an mPOF which contains a) 3 air-holes b) 5 air-holes. c) Normalized absorption spectra of selected water mixture [88].

Significant research was carried out by Warren and Monro. Warren [105] presented sensing with an exposed-core SC-MOF where just one air-hole was filled with the liquid analyte. In the article, the first theoretical study of this fiber for the purposes of absorption and fluorescence sensing was presented. The mode profile spreading out into the exposed section was investigated and simulated with FEM as shown in Fig. 2.18, where subwavelength core diameters were simulated. The effective mode area, as well as power fraction calculation, has been provided, which is important for sensitivity evaluation during the design process.

The SC-MOF analysis was later extended from conventional silica glass to fibers having a glass material of higher RI (therefore stronger mode confinement), e.g., SC-MOFs made from lead-silicate (RI = 1.62) and bismuth (RI = 2.09) glass. Warren [105] showed that a SC-MOF of higher RI glass material could be used for higher liquid analyte RI sensing and suppresses internal interferences. The less sensitive wavelength of 590 nm,
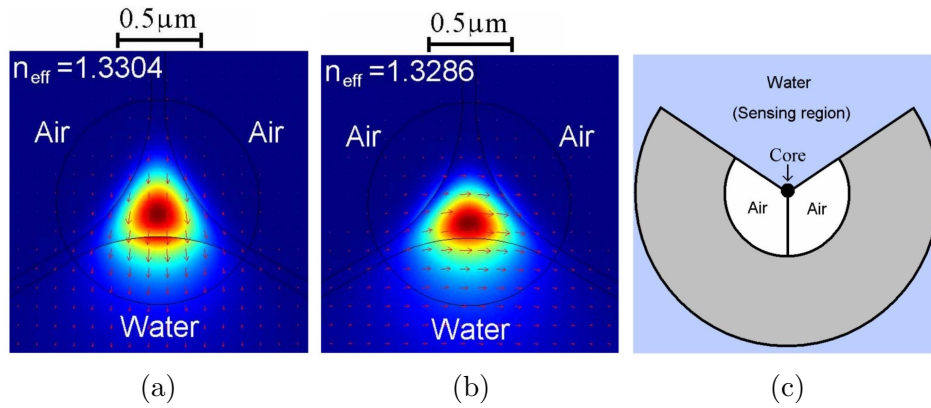
Figure 2.18: a) First and b) second fundamental modes of filled silica SC-MOF, having core diameter 0.505 μm, c) schematic picture of the SC-MOF [105].

with regard to evanescent-wave overlap (selected because of fluorescence sensing), was compensated by fabricating an SC-MOF whose core diameter was below 0.6 μm. It was calculated that an SC-MOF sensor with an exposed-core can reach the performance of a fully-filled SC-MOF sensor. It was shown that SC-MOFs with larger core diameters have a larger effective area for a fully filled SC-MOF, in contrast to a one filled air-hole, and vice versa as depicted in Fig. 2.19a). Liquid interface transmission for coupling in and out of SC-MOF was analyzed and the results are depicted in Fig. 2.19b). It is mentioned that for smaller core diameters the amount of interface losses increased, and that for exposed and fulfilled fiber it is similar. For silica, these interference losses are significant if the core is smaller than 0.5 μm. This number refers to measurements with water and can vary based on the RI of the liquid. Coupling efficiency was studied as well and the results are depicted in Fig. 2.19c). These measurements presented the same properties of fully-filled SC-MOFs, as well as exposed-core SC-MOFs and pointed to their advantages as well as their similar limitations.

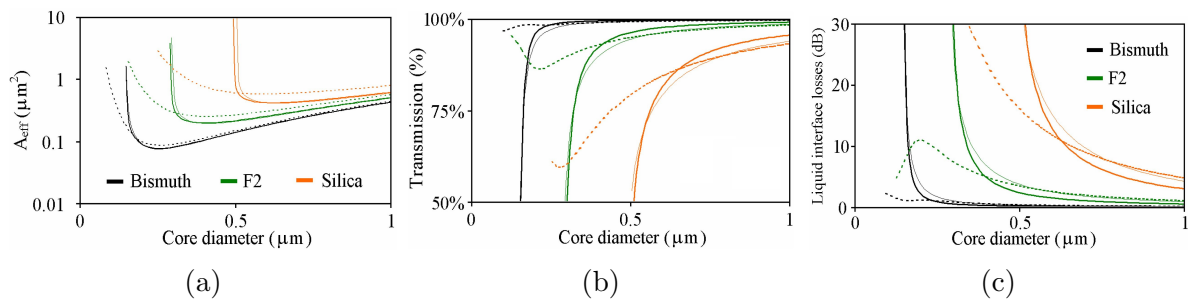Figure 2.19: SC-MOF fully filled by water (dashed) and SC-MOF with one hole containing water (solid) - a) effective area, b) liquid transmission on the interface for in- and out-coupling, c) liquid interface losses for in- and out-coupling [105].

Later, the research was extended using two methods for fabricating exposed-core SC-MOFs, and these methods were demonstrated using lead-silicate glass SC-MOFs [89].

The first method involved etching the SC-MOF after the draw, the second method involved exposing the SC-MOF core at the preform stage and directly drawing the exposed-core SC-MOF. The functionalized surface of the SC-MOF was presented two years later [106] for fluorescent real-time sensing of aluminum ions. New preforms [107] with an exposed-core, more suitable for sensing, were created by Warren et al. and the splicing of these exposed-core SC-MOFs to conventional SMFs was investigated. Theoretical, as well as experimental, results of splice loss from the SMF to the exposed-core SC-MOF, were presented. FBG was inscribed to the exposed-core SC-MOF and RI, with precision up to 6.4 nm/RIU, was measured with the theoretical limit estimated at 101 nm/RIU. Schartner [93] continued to developed exposed core SC-MOF fibers, demonstrating <1 dB/m guidance losses for core diameter 1.65 μm at 1550 nm opening up possibilities for using these SC-MOFs for long-distance distributed measurements.

Many SC-MOF properties were studied in by Monro [108] with a focus on light confinement in the core with regard to wavelength and sub-wavelength scale core diameters. The research was driven by the motivation to enhance the power fraction of the guided light, and to make an impact on the performance of SC-MOF sensors, thus increasing their sensitivity. A simulation of the effective area and the power fraction of SC-MOF fibers was presented with respect to their core diameters and analyte-filled air-holes (with air or water). More glass materials, such as silica, lead-silicates, and bismuth, were studied. Monro mentioned that the impact of the choice of SC-MOF core diameter on the fiber attenuation must be considered. For larger (>2 μm) SC-MOFs core diameters, fiber attenuation tends towards material loss (most notably material absorption and loss resulting from fabrication-related imperfections), indicating that fabrication, confinement and scattering losses (due to surface roughness [109]) are negligible [110]. Thus, confinement loss can be essentially eliminated via appropriate SC-MOF design. Note that when SC-MOFs are filled with liquid analytes, confinement losses increases. Results of several research groups regarding propagation losses in a small core SC-MOF were summarized

(a)   (b)
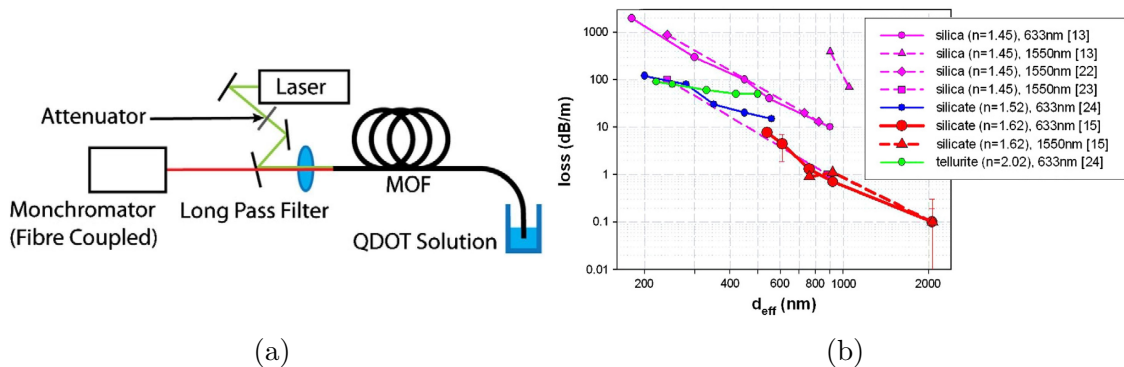
Figure 2.20: a) measurement scheme based on the dip of an SC-MOF [97] b) Propagation losses for selected core diameters using different glasses and for different wavelengths [108].

in [108], depicted in Fig. 2.20b), where previous measurements are extended to 1550 nm (where mode power fraction is greater) and conducted on selected materials and core diameters (200 nm - 2 μm). Further fluorescent measurement was carried out on the same SC-MOF based on the scheme depicted in Fig. 2.20a). This setup could also be used for the absorptive type of measurement.

Results from Fig. 2.20a) demonstrate the work of Ebendorff-Heidepriem [97], who reported the fabrication of SC-MOFs from F2 lead silicate glass material (n = 1.62) and compared it to other materials and wavelengths. Nanoscale core diameters have been reached due to direct drawing and without the use of any post-processing. Ebendorff reported effective mode area and propagation loss characteristic of these fibers with respect to core diameter and compared them with circular nanowires reported in [111]. Further, propagation losses of an SC-MOF (made from F2 material) are depicted in Fig. 2.21, which predict their area of usability and report dependency on core diameter.
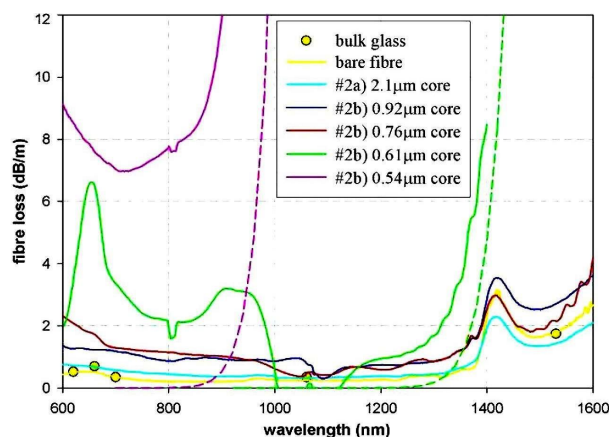

Figure 2.21: Measurement of spectral absorption by the cut-back method for an SC-MOF made from F2 material. Dashed lines represent two modeled SC-MOF with the smallest core diameters [97].

SC-MOF sensors were compared to HC-MOF by Lehmann in [112] in terms of sensitivity and spectral bandwidths in the NIR region. The SC-MOF performed better for higher RIs of the analyte and for longer sensor lengths due to the robustness to the interferences inside the SC-MOF. A comparison between SC-MOF was presented by Schuster [113] for ethylene sensing while declaring the advantages of three air-hole SC-MOFs over four air-hole MOFs. Attenuation spectra and sensitivities were measured for both SC-MOF, with a core of 1.5 μm and bridge widths < 700nm. Measurements results are presented in Fig. 2.22a,b). Furthermore, two gas feeding techniques were tested for another MOF with a fiber-end face inlet and side-filling using laser drilled holes.

Temperature, an important additional parameter which influences measurement precision, was studied in [114]. Temperature sensitivity of selected liquid-analyte filled solid-core MOFs was studied to compensate for RI measurement, using liquid oil with a thermo-

optic coefficient of -4.79 x $10^{-4}/^{o}C$, as well as fiber-filling and fiber splicing. Variations of the RI (liquid 1.300 to 1.430) with temperature are depicted in Fig. 2.22c), predicting an average error of compensated measurement at 3.03 x 10^{-4}.
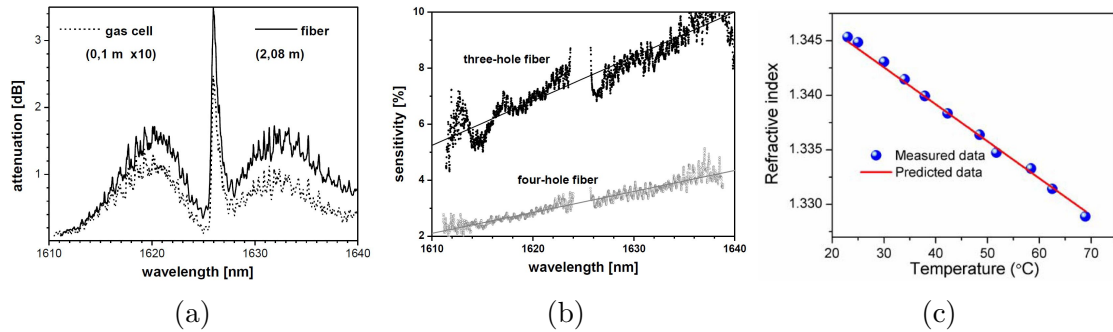

Figure 2.22: a) 3 air-hole SC-MOF and gas cell absorption spectrum of Ethylene, b) sensitivity of 4- and 3- air-hole SC-MOF [113] c) measured RI dependence on temperature of selected analytes [114].

3. Objective of the thesis

The previous chapters revealed that in the field of specialty optical fibers for the refractometric detection of liquids theoretical background and basic measurement configuration have been described. This opens up possibilities for investigation of advanced techniques leading to significant sensitivity enhancement. For TOF sensors, stability and long-term performance, as well as methods of achieving high fabrication repeatability can be perfected. Furthermore, advanced sensing methods based on MOFs, especially SC-MOFs, offer a promising substitute to TOFs, and, in several aspects, they provide substantial advantages. However, a universal methodology for refractometric SC-MOF sensing of liquid analytes is still missing.

Therefore, the goals of this thesis are set as:

- Analyze TOFs concerning various fiber types (single-mode, multi-mode, polymer-clad silica). Extend the knowledge of sensitivity enhancement, measurement repeatability and long-term stability of TOF sensors.

- Design and analyze alternative approaches for the refractometric detection of liquids using. Describe and characterize SC-MOF sensors for RI measurements.

- Compare parameters of TOF and SC-MOF sensors and determine their advantages and drawbacks.

- Develop a generalized analytical model of the SC-MOF sensor

To achieve these goals, the following milestones have been selected

- Analyze the detection of various liquid analytes using TOFs with respect to the tapering process and fiber types.

- Characterize a significant number of single-mode and multi-mode TOF sensors to examine sensor performance, including long-term measurements.

- Analyze aspects of refractometric detection of liquid analytes with SC-MOF

- Perform a critical parameter selection of refractometric sensors based on SC-MOFs.

- Derive a universal analytical model to characterize a sensing methodology with SC-MOF.

4. Achieved results

Results, forming the core of the thesis, have been published in significant scientific journals and international conference proceedings. The main results, forming the following chapters, are published in seven journal papers [J1-J7].

Chapter 4.1 presents a theoretical approach for MM optical fibers submerged in liquid analytes. We focused on higher-order modes propagation in order to find modes with the highest sensitivity with respect to specific liquid analyte absorption. This estimation could be used to increase the overall performance of such MM fiber-based sensors. The analytical approach was then verified by an experimental campaign utilizing a chalcogenide MM fiber which allows detection in the mid-infrared region.

Chapter 4.2 presents results from the study of plastic-clad silica fiber and graded-index MM TOFs acting as refractometric sensors for the detection of liquids. Sensitivity was increased by fiber tapering and, further, by U-shaping the TOF profile. The TOF preparation process has been perfected on over 200 samples. Significant trends of sensitivities and, for the first time, sensitivity saturation points for different fibers dependent on the TOF waist diameters have been determined. Optimal TOF waist diameter, in terms of sensitivity, allows us to determine the most effective working points of the sensor. With the aim of a real application, a long-term measurement over 6 months was carried out.

Furthermore, Chapter 4.3 contains recently published journal paper [J3], where improvement of sensitivity has been investigated. Structural modification caused by sol-gel development in single-mode TOF surface layer has been evaluated, leading to TOF sensitivity enhancement up to ten times. Later on a 12-months continuous measurement campaign with a liquid analyte having variable RI, have been carried out. The campaign verified single-mode TOF sensor stability. This long-term measurements has been carried out with one freshly fabricated TOF and one TOF with surface structural modification to evaluate the impact of the structural modification on sensitivity, resolution and sensor stability.

In Chapter 4.4 a novel attenuation-based detection approach is presented, for the first time based on SC-MOFs. In this paper extreme evanescent-wave overlap, which is present SC-MOFs, was exploited to determine a particular liquid analyte based on its refractive index. The liquid filling process was proposed and mastered to enable precise and equal filling in all SC-MOF air-holes. Furthermore the measurement configuration was designed, which was afterwards realized and provided significant results. Simulations of the mode field distribution in terms of the evanescent-wave overlap, as well as experimental analysis of multiple liquid analytes, were carried out. SC-MOF behavior as a sensor has

been investigated, proving high sensitivity and resolution while maintaining measurement simplicity in terms of attenuation-based refractometry. Last but not least thanks to the SC-MOF inner structure, only extremely small amount of liquid analyte in order of nanoliters is required.

In Chapter 4.5 a semi-ellipsoidal sensing element is presented and compared to the SC-MOF and TOF sensors. The main advantage of the semi-ellipsoidal sensor is its simplicity combined with its high sensitivity to the external RI and its capability of covering a broad measuring range by varying the position of the input optical fiber. The sensing region, featuring a semi-ellipsoidal element, is easy to change and enables wide RI measurement range, however, both the TOF and SC-MOF sensors exhibit higher sensitivity, especially close to the refractive index of silica.

In Chapter 4.6 a comparison of a TOF and SC-MOF sensors is presented, both theoretically and experimentally. The study of a TOF sensor and an SC-MOF sensor is carried out for the purposes of detecting glycerol dissolved in water, which represented hazardous liquids with identical refractive indices such as gasoline. Experimental campaign involved identical analyte environment for both sensors, thus accurate comparison was obtained. Possible practical applications, especially in the field of petrochemistry, are discussed as well.

Chapter 4.7 significantly extends the previous SC-MOF study by deriving a universal methodology for the utilization of SC-MOF sensors. First, an analyte-filled SC-MOF has been described analytically and the influence of key parameters has been determined to design a high-quality sensor. Secondly, 283 measurements with various SC-MOFs and different liquid analytes were carried out. In comparison to previous results, higher sensitivities have been reached for longer filling lengths of SC-MOF sensors. Based on the obtained data set, a generalized model of an SC-MOF sensor has been derived which could be used as a universal tool for SC-MOF sensor design. Using the generalized SC-MOF sensor model enables us to determine, based on preset demands, specific sensor attributes such as sensitivity, resolution, dynamic range and to predict overall sensor behavior.

4.1 Multimode chalcogenide fibers for evanescent wave sensing in the mid-IR

This chapter is a version of the published manuscript:

[J1]: E. A. Romanova, S. Korsakova, M. Komanec, T. Nemecek, A. Velmuzhov, M. Sukhanov, and V. S. Shiryaev, "Multimode Chalcogenide Fibers for Evanescent Wave Sensing in the Mid-IR", IEEE JOURNAL OF SELECTED TOPICS IN QUANTUM ELECTRONICS, vol. 23, no. 2, 2017.

Relevance to my Ph.D. thesis:

This paper focuses on specialty optical fibers for the detection of liquids in terms of a non-silica glass material fiber, specifically a chalcogenide multi-mode coreless fiber. If the fiber is properly excited, higher-order modes significantly overlap into the surrounding liquid analyte via the evanescent-wave of that particular mode. To examine which mode has the highest sensitivity we presented a detailed analysis of mode absorption of a general MM fiber based on a theoretical approach. Modes with the highest sensitivity were determined. Sensitivity can be significantly increased by selective mode excitation. The theoretical approach was supported by experiments with the MM chalcogenide fiber in the mid-infrared region, where the chalcogenide glass material has high transparency. The spectral absorbance, of selected liquid analytes, has been obtained with respect to molar concentrations. In the experiments, the linear dependencies of the absorbance on the concentration of the analyte were obtained.

Multimode Chalcogenide Fibers for Evanescent Wave Sensing in the Mid-IR

Elena A. Romanova, Svetlana Korsakova, Matej Komanec, Tomas Nemecek, Alexander Velmuzhov, Maksim Sukhanov, and Vladimir S. Shiryaev

Abstract—**Evanescent wave spectroscopy in the mid-infrared (MIR) is a powerful tool for remote real-time sensing. Chalcogenide fibers transparent in MIR are considered as a base for creation of a fiber-optical platform for the MIR sensing. In this paper, a rigorous theoretical approach has been applied for the analysis of evanescent modes propagation in a multimode chalcogenide fiber surrounded by an absorbing medium. A role of particular evanescent mode in power delivering through the fiber has been revealed. Strong absorption of water in this spectral range has been shown to be a main factor limiting sensitivity of the evanescent wave sensor. Possibilities of sensitivity enhancement by using waveguiding properties of the fiber have been discussed. The analysis is supported with an experimental measurement of a $[GeSe_4]_{95}I_5$ glass fiber partially immersed in an aqueous acetone solution, in the wavelength range of 2–5 μm.**

Index Terms—**Optical fiber devices, infrared sensors, glass, electromagnetic propagation.**

I. INTRODUCTION

CONTROL of environmental hazards in cities, enterprises and objects of nature is necessary for health protection and safety. A basis of an effective control is real-time monitoring of air and water chemical composition, which gives information about the content of toxic impurities.

Technology for evanescent wave sensing based on silica fibers is limited to the near-infrared (NIR) and visible (VIS) spectral ranges due to the fibers are transparent at the wavelengths $\lambda = 0.4 - 2.0 \, \mu m$. Silica fibers and all supporting technology are already mature in the form of compact sources, detectors, connectors, gain media, which can route and exploit the NIR and VIS. However an unambiguous identification of molecular species is not possible in these spectral ranges. In the mid-infrared (MIR,

$\lambda = 3 - 25 \, \mu m$) spectra of inorganic and organic molecular substances exhibit strong fundamental vibration bands much more suitable for spectroscopic analysis than the weak overtone absorption bands in NIR and VIS.

MIR spectroscopy provides a universal tool for quantitative detection of molecular species in gaseous or liquid form. Current state-of-the-art approach utilizes a sample chamber of an IR spectrometer in which any gas or liquid substance can be analyzed. For real-time remote molecular sensing outside of a laboratory, special technological platform is to be developed.

Chalcogenide glasses are known for their high transparency in MIR, which makes them attractive for the design of a MIR sensing platform. Compositional changes of the glass give rise to variations in optical, physical, chemical, thermal and mechanical properties important for subsequent fabrication of optical devices in both fiber and planar waveguide form.

In recent decades, there has been a significant progress in the design of chalcogenide glass fibers and integrated optical devices for chemical sensing [1], [2] that is often based on evanescent-wave absorption in an external medium and subsequent attenuation of the power transmitted by a fiber or waveguide at wavelengths corresponding to characteristic absorption bands of molecules in a studied medium.

For efficient interaction of the evanescent field with absorbing species, an unclad fiber or waveguide are to be used, or some part of the cladding is to be removed over a given sensing length. In NIR, refractive index of a chalcogenide glass ($n \approx 2.40 - 2.80$) is usually much greater than that of aqueous solutions of measureable analytes ($n \approx 1.30 - 1.50$) and propagating radiation is more confined in a chalcogenide fiber core in comparison with a silica one ($n \approx 1.45$). This is a drawback for the evanescent wave spectroscopy where amount of radiation propagating in the external medium is the key parameter.

Multimode chalcogenide fibers were used in [3]–[5] for measurements of the absorbance spectra of various chemical substances in aqueous solutions in MIR spectral range. In the experiments, linear dependencies of the absorbance on the analytes concentration were obtained. The importance of using multimode fibers to provide linear logarithmic output characteristics and high sensitivity was demonstrated in [6], [7] for a straight silica fiber acting as a sensing element in VIS. In [7], a multimode silica fiber with microbends over a length of 60 mm was used, where the evanescent-wave sensor was acting as a logarithmic detector with a dynamic range greater than six orders of magnitude.

In spite of several successful experimental demonstrations of optical fibers utilization for the evanescent-wave spectroscopy, a rigorous theoretical approach based on electrodynamics' calculation of evanescent modes of a fiber with an absorbing cladding has not been yet applied as a possible design tool.

Theoretical consideration of the evanescent-wave absorption was usually based on a simple approach using an assumption that the input power decreases only in a surrounding absorbing medium acting as the fiber cladding but it keeps constant in the fiber core [1], [6], [7]. In this case, normalised transmittance can be evaluated as:

$$T = P/P_0 = \sum_{i=0}^{N} \left(P_1^i + P_2^i \cdot \exp(-\alpha \cdot L) \right) / \sum_{i=0}^{N} \left(P_1^i + P_2^i \right)$$

$$= 1 - (1 - \exp(-\alpha \cdot L)) \cdot \sum_{i=0}^{N} r_2^i \qquad (1)$$

Here P and P_0 are the total powers transmitted through the fiber, respectively, with and without an absorbing medium over an unclad section of length L, α represents the bulk absorption coefficient of the medium, N stands for the number of guided modes propagating in the fiber. P_1^i and P_2^i are powers of the i-th guided mode, respectively, inside and outside the fiber core in non-absorbing medium (air), r_2^i is the fraction of the i-th guided mode power outside the fiber core:

$$r_2^i = P_2^i / \sum_{i=0}^{N} \left(P_1^i + P_2^i \right). \qquad (2)$$

In an assumption that $\alpha \cdot L << 1$, (1) can be reduced to:

$$T \approx 1 - \alpha \cdot L \sum_{i=0}^{N} r_2^i \approx \exp(-\sigma \cdot L), \qquad (3)$$

where σ is the evanescent-wave absorption coefficient:

$$\sigma = \alpha \sum_{i=0}^{N} r_2^i \qquad (4)$$

In MIR, the molecular absorption bands are strong and the condition $\alpha \cdot L << 1$ is not generally satisfied.

An approximate approach developed in the framework of geometric optics [8], [9] is relatively simple and efficient for analysis of launch conditions in multimode fibers. However being based on calculation of Fresnel reflections from an absorbing medium in the local plane wave approximation, it fails to describe penetration of radiation outside a fiber core.

Rigorous approach based on electromagnetic theory of optical waveguides [10] is a base of modern designs of fiber-optic devices. In this paper, we apply this approach for analysis of experimental results obtained in measurements of transmittance spectra of radiation passed through a chalcogenide fiber immersed into aqueous acetone solutions. Purpose of this analysis was twofold: first, to describe electromagnetic phenomena in the fiber for a particular experimental situation; second, to reveal specific features of the evanescent wave measurements in MIR spectral range.

II. EVANESCENT MODES OF AN OPTICAL FIBER

In electromagnetic theory of optical fibers, complex-valued dielectric constants are used to describe light absorption in a fiber material. If a fiber segment is submerged into an absorbing medium, this medium acts as an absorbing fiber cladding [10]. Then propagation constants of the fiber modes are complex-valued, too, so that all the guided modes become evanescent. Power flow of an evanescent mode along the fiber axis is decreasing, radial and azimuthal components of the power flow in the fiber being non-zero that means constant power leakage outside the fiber core.

Amplitudes of the evanescent modes can be found from radiation launching conditions at the input facet of the fiber. When an input light beam is coaxial with a fiber axis, only azimuthally symmetric modes of the fiber can be excited. Azimuthally symmetric modes of a weakly guiding step-index fiber are known as $\mathrm{HE}_{1m}-$modes [10] with m being a mode radial order. If the difference between refractive indices of the core n_{co} and cladding n_{cl} is large, the weakly guiding approximation is not valid and solutions of the exact characteristic equation:

$$\left\{ \frac{J_1'(u_m)}{u_m \cdot J_1(u_m)} + \frac{K_1'(w_m)}{w_m \cdot K_1(w_m)} \right\}$$

$$\cdot \left\{ \frac{J_1'(u_m)}{u_m \cdot J_1(u_m)} + \frac{n_{\mathrm{cl}}^2}{n_{\mathrm{co}}^2} \cdot \frac{K_1'(w_m)}{w_m \cdot K_1(w_m)} \right\}$$

$$= \left(\frac{\beta_m}{k \cdot n_{\mathrm{co}}} \right)^2 \cdot \left(\frac{V}{u_m \cdot w_m} \right)^4 \qquad (5)$$

are to be found. In (5), J_1, K_1 are, respectively, Bessel and Macdonald functions, J_1', K_1' represent derivatives of the functions, u_m and w_m are parameters, which describe transverse profile of the m-th fiber mode, $\beta_m = \sqrt{k^2 n_{\mathrm{co}}^2 - u^2/R^2}$ is a longitudinal propagation constant, $V = k \cdot R \cdot \sqrt{n_{\mathrm{co}}^2 - n_{\mathrm{cl}}^2}$ is the fiber parameter, $k = 2\pi/\lambda$, R stands for the fiber core radius. The refractive indices $n_{\mathrm{co}} = n_{\mathrm{co}}' + i \cdot n_{\mathrm{co}}''$, $n_{\mathrm{cl}} = n_{\mathrm{cl}}' + i \cdot n_{\mathrm{cl}}''$ are complex in general with the nonzero imaginary parts appearing due to material losses in the fiber.

Longitudinal propagation constants $\beta_m = \beta_m' + i \cdot \beta_m''$ of the evanescent modes can be found by numerical solution of (5). Attenuation coefficient $\eta_m = 2\beta_m''$ is related to the m-th fiber mode power decrease along the fiber axis z:

$$P_m(z) = P_{0m} \exp\left(-\eta_m z\right) \qquad (6)$$

Here P_{0m} is the initial power of an evanescent mode at the fiber input facet, $P_m(z)$ is evaluated as longitudinal component of a power flow. The fraction of an evanescent mode power (2) outside a fiber core is a determining parameter for the attenuation coefficient magnitude. In fact, for each mode this fraction depends on the ratio R/λ [10]. At a given λ, this fraction grows with decrease of the core radius until the mode reaches its cutoff. For a given R, this fraction increases with wavelength.

As guided modes of an infinite dielectric cylinder used as a fiber model are orthogonal they propagate independently of each other and the power flow propagating in a multimode fiber is equal to the sum of powers of all the modes.
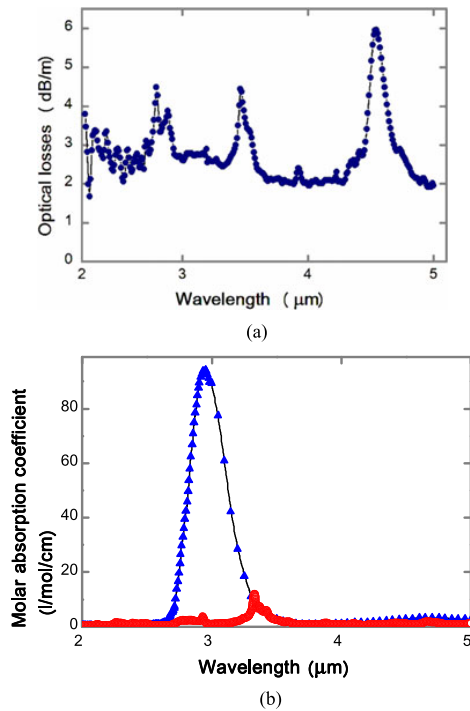
Fig. 1.   Spectral dependencies of: optical losses in the [$GeSe_4]_{95}I_5$ fiber (a); molar absorption coefficients of water (triangles), acetone (open circles) (b).

As follows from the theory of optical waveguides, number N of guided modes in a fiber is defined by the magnitude of parameter V. For each HE_{1m} mode, the cutoff parameter V_c can be found from the condition $J_1(V_c) = 0$ [10]. If $V_c < V$, the HE_{1m} mode is a guided mode. In an absorbing fiber, shape of the transverse profile of electromagnetic field of an evanescent mode does not vary along the fiber, but its power decreases [11]. Transformation of such an evanescent mode into a leaky one at the cutoff is rather complex [11], but the magnitudes of V_c calculated for a lossless fiber of the same geometry still can be used for N evaluation. A fundamental difference between an evanescent mode and a leaky mode is that electromagnetic field of a leaky mode grows in radial direction outside a fiber core.

III. Measurements of the Evanescent Modes Transmittance in Aqueous Acetone Solutions

In this work, measurements were carried out with a multimode single-index (unclad) fiber made of [$GeSe_4]_{95}I_5$ glass ($R = 145\,\mu m$). The [$GeSe_4]_{95}I_5$ fiber was fabricated from a melt from a single crucible as described in details in [12]. Addition of iodine atoms into the glass matrix reduces the formation of crystalline phases during bulk sample annealing and fiber drawing. The glass rod was placed in the crucible and heated to a plastic state (at the temperature about 300 °C). Inert gas (Ar) pressure was used to create the necessary melt flows through the die.

Optical losses of the fiber (Fig. 1(a)) were measured by using the conventional cut-back technique. Because of the low optical

losses in the range of wavelengths 2–9 μm [12], this fiber is very promising for MIR spectroscopy. Refractive index of this glass is around 2.4 in NIR [13] and can be taken of this magnitude in MIR because the refractive index is almost constant in spectral range far from the fundamental absorption band edge that is at $\lambda \approx 0.6\,\mu m$ for the [$GeSe_4]_{95}I_5$ glass.

Aqueous acetone solutions were used in [3]–[5], [12] in similar experiments.

Spectral dependencies of the molar absorption coefficients shown in Fig. 1(b) have been obtained from the IR spectra of bulk water and bulk acetone recorded by using a Fourier - Transform Infrared Spectrometer (FTIR) in zinc-selenide cells with the optical path-length of 18 μm. At around $\lambda = 3.33\,\mu m$, an absorption band is observed that is attributed to acetone molecular vibrations.

From these measurements, the molar absorption coefficient of pure acetone ($\alpha_m^a = 12.01/mol/cm$) and pure water ($\alpha_m^w = 9.01/mol/cm$) have been obtained at $\lambda = 3.33\,\mu m$. As the molar concentration of water ($c^w = 55.5\,mol/l$) is much greater than that one of acetone ($c^a = 13.5\,mol/l$), the resulting absorption coefficient of water is much greater than that of acetone ($\alpha_m^a c^a << \alpha_m^w c^w$). These conditions are absolutely different than in VIS range measurements where water absorption is negligible.

For experimental treatment, a broadband 50 W silicon-nitride bulb-based MIR light source with the maximum intensity at $\lambda = 2.5\,\mu m$ was used. The light source was free-space coupled to the $[GeSe_4]_{95}I_5$ fiber, which was cleaved at a 90° angle with a specialized low-tension cleaver.

The whole fiber facet area was coaxially and uniformly irradiated. Output signal was then detected by an FTIR within the spectral range $\lambda = 2 - 6\,\mu m$.

The [$GeSe_4]_{95}I_5$ fiber was inserted into a slightly curved silica glass tube of the length of 24 cm, diameter of 7 mm and radius of curvature of 15 cm (Fig. 2(a)). This tube was used to decrease acetone evaporation that is quite fast in an open vessel.

At first, transmittance T_0 of the fiber without the liquid analyte was acquired. Next, an aqueous acetone solution was poured into the tube in a total volume of 5 ml, and the transmittance T_1 was measured again. Relevant length L of the fiber submerged into the solution was equal to 14 cm. By evaluating the normalized transmittance $\tau = T_1/T_0$ for each concentration of the solution, the influence of reflections from the fiber facets was minimized.

Spectral dependencies of τ shown in Fig. 2(b) have been obtained for several volume concentrations of acetone. As water absorption was strong, the absorption peak of acetone at $\lambda = 3.33\,\mu m$ was not observable at its volume concentration less than 50%.

IV. Electromagnetic Analysis

Number N of the evanescent modes of the [$GeSe_4]_{95}I_5$ fiber varies over the spectral range of the fiber transmittance measurements (Fig. 3(a)). At $\lambda = 5\,\mu m$, N is more than two times less than at $\lambda = 2\,\mu m$. As refractive indices of water and acetone have similar values ($n^w = 1.33$ and $n^a = 1.35$), N does not depend on the acetone solution concentration. The number of
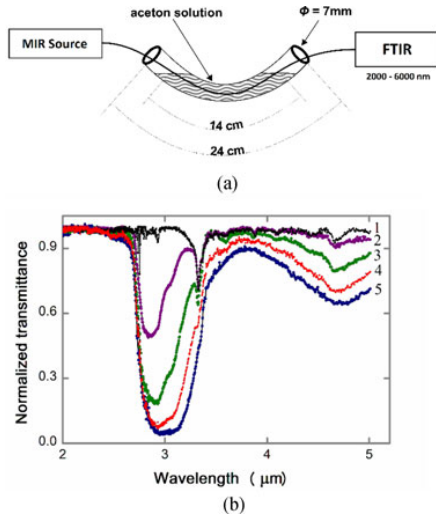
Fig. 2.   Measurement configuration schematic with a glass tube filled with an aqueous acetone solution. (a); measurement results for various volume concentrations of acetone: 100% (1), 90% (2), 75% (3), 50% (4), 0% (pure water) (5)(b).

modes is less in a fiber section immersed in the solution than that in the same fiber in the air. This is a reason for some additional radiation losses when electromagnetic field is propagating through the boundary between air and the acetone solution.

In order to evaluate attenuation coefficients of the evanescent modes, imaginary parts of refractive indices of the fiber material and surrounding medium are to be quantified.

In the $[\,GeSe_4]_{95}I_5$ fiber, material absorption coefficients of the bulk glass samples of the compositions $[\,GeSe_4]_{95}I_5$ in the spectral range 2–5 μm are no more than 0.01 cm^{-1} [12] that is significantly less than the absorption coefficients of aqueous acetone solutions at $\lambda = 3.33\,\mu$m (for ex., $\alpha_m^a c^a = 162$ cm^{-1}). Then absorption of the fiber material can be neglected ($n''_{co} = 0$).

As absorbance of a solution in bulk is:

$$A = (\alpha_m^w c^w + \alpha_m^a c^a) \cdot L, \qquad (7)$$

in accordance with the Bouguer-Lambert-Beer law, the imaginary part of the refractive index of the solution can be defined as:

$$n''_{cl} = (\alpha_m^w c^w + \alpha_m^a c^a) \cdot \ln(10)/(2k). \qquad (8)$$

In Fig. 3(b), magnitudes of the attenuation coefficient η_m evaluated at $\lambda = 3.33\,\mu$m by numerical solution of (5) are plotted for pure water and for pure acetone at each radial order m of the HE_{1m} modes of the $[GeSe_4]_{95}I_5$ fiber. In accordance with the theory of optical fibers [10], higher-order modes of the fiber have greater penetration into the cladding than the lower-order ones (an example is shown in Fig. 3(c), inset). That is why magnitudes of η of the higher-order modes shown in Fig. 3(b) are more than ten times greater than that of the fundamental mode.

In the analysis, it is reasonable to find out how η_m depends on the fiber core radius. If the $[\,GeSe_4]_{95}I_5$ fiber would have a greater or a lesser R, the number of modes would increase
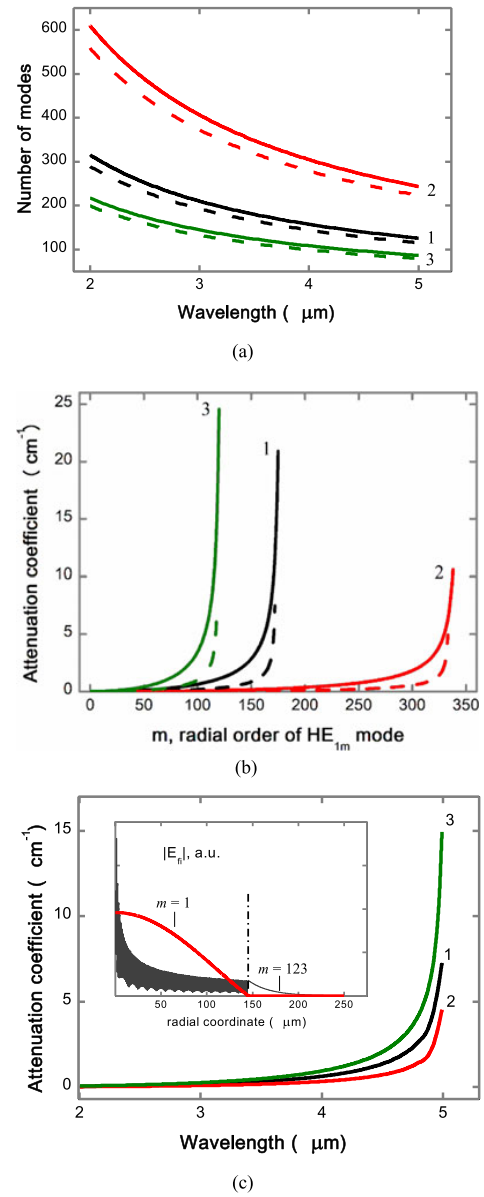

Fig. 3.   Number of the HE_{1m} modes of the $[\,GeSe_4]_{95}I_5$ fiber in air (solid lines), immersed in aqueous acetone solution (dashed lines) (a); attenuation coefficient of the HE_{1m} modes of the fiber immersed in pure water (solid lines), in pure acetone (dashed lines) at $\lambda = 3.33\,\mu$m (b); attenuation coefficients of the HE_{1m} modes with $m = 114$ (1), 221 (2), 79 (3) (c); Inset: radial profiles of electrical field components of the HE1m modes with m = 1 and m = 123 at $\lambda = 4.6\,\mu$m. R = 145 μm (1), 280 μm (2), 100 μm (3).

or decrease, respectively, at a given wavelength as shown in Fig. 3(a). Attenuation coefficient of each evanescent mode of a given m grows with an R decrease (Fig. 3(b)) because of greater penetration of the mode filed into the absorbing medium (see Section II). From this point of view, it would be optimal to decrease R as much as possible taking into account relating technological restrictions. However, as was mentioned in Section I, a

multimode propagation has an advantage in providing a logarithmic output characteristics and a large dynamic range [6], [7].

Another important feature is that at a given core radius, η_m of each radial mode grows with wavelength due to greater penetration of a mode field into the cladding (see Section II). In Fig. 3(c), the magnitudes of η_m have been calculated in assumption that the absorption coefficient of a liquid was the same at all the wavelengths (equal to $\alpha_m^a = 12\,1/mol/cm$ at $\lambda = 3.33\,\mu m$). The observed η_m increase with wavelength is specifically due to the waveguiding properties of the fiber. It is shown here that if the $[GeSe_4]_{95}I_5$ fiber would be of $100\,\mu m$ core radius it would be more efficient for the evanescent wave spectroscopy. Over the range $\lambda = 2-5\,\mu m$ (Fig. 3(c)), attenuation coefficients of the highest-order HE_{1m} mode ($m = 79$) of the fiber with $R = 100\,\mu m$ are larger than those of the fibers with greater radii ($m = 114$ for $R = 145\,\mu m$, $m = 221$ for $R = 280\,\mu m$).

This wavelength dependence of the attenuation coefficients reveals why decrease of the fiber transmittance measured at $\lambda = 4.7\,\mu m$ (Fig. 2(b)) is significant in spite of the bulk absorption coefficients of water and acetone are small at this wavelength (Fig. 1(b)).

When several evanescent modes propagate in a fiber, total transmittance depends on initial amplitudes of the modes at the input facet of the fiber. In general, the initial amplitudes depend on radiation launching conditions.

In our analysis, we assume at first that all the input power was launched into just one m-th evanescent mode. For this case, the normalized transmittance $\tau = P_m(L)/P_{0m}$ has been calculated for several evanescent modes of the fiber immersed in pure acetone (Fig. 4(a)) or in pure water (Fig. 4(b)).

Transmittance of some higher-order modes at some wavelengths is equal to zero because their attenuation length $L_m = \eta_m^{-1}$ is much less than the length of fiber length immersed in the solution $L = 14\,cm$ (for ex., in Fig. 4(b), for the evanescent mode with $m = 100$ at $\lambda = 3.33\,\mu m$, $L_m \approx 1\,cm$).

This means that if only the higher-order modes be excited at the input facet, L can be significantly reduced for sensing purposes. In comparison with the higher-order modes, the lower-order ones are delivering power over longer distances. Attenuation coefficient of the fundamental evanescent mode ($m = 1$) is so small that $L_m \gg L$ and the mode transmittance is equal to unity over all the spectral range. Then we can conclude that the observed decrease of transmittance measured in the experiment (Fig. 2(b)) is due to absorption by a group of evanescent modes having the attenuation length $L_m \approx L$. For the $[GeSe_4]_{95}I_5$ fiber, these are modes with $m > 10$ (Fig. 4).

As a next step of the analysis, we assume that the input power is equally distributed between all the evanescent modes. Then the normalized transmittance can be evaluated as

$$\tau = N^{-1} \sum_{m=1}^{N} \exp(-\eta_m L), \qquad (9)$$

In spectroscopic sensors based on measurements of power decrease over a path length in a bulk liquid substance, transmittance can be evaluated separately for water T^w and acetone T^a
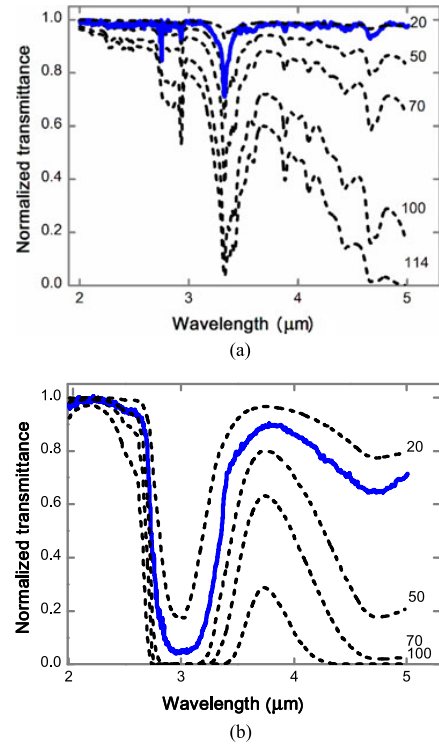

Fig. 4. Normalized transmittance (τ) of the $[GeSe_4]_{95}I_5$ fiber immersed in pure acetone (a) and in pure water (b): measured (solid lines) and calculated for HE_{1m} modes with $m = 20,50,70,100,114$ (dashed lines). $R = 145\,\mu m$, $L = 14\,cm$.
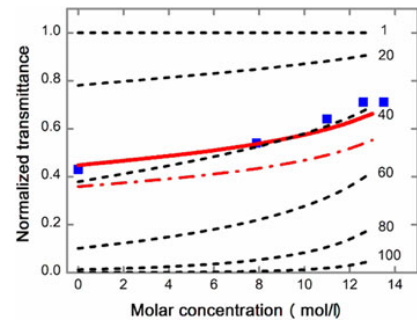
Fig. 5. Normalized transmittance (τ) at $\lambda = 3.33\,\mu m$ of the $[GeSe_4]_{95}I_5$ fiber immersed in the acetone solution: measured (squares), calculated for the HE_{1m} modes with $m = 1, 20, 40,60,80,100$ (dashed lines), calculated by using (9) with $N = 80$ (solid line), $N = 100$ (dash-dot line). $R = 145\,\mu m$, $L = 14\,cm$.

so that the total transmittance is equal to their product:

$$T = 10^{-A} = 10^{-\alpha_m^a c^a L} \cdot 10^{-\alpha_m^w c^w L} = T^a \cdot T^w \qquad (10)$$

However for a fiber with an absorbing cladding, (10) is not valid because the magnitude of β_m'' of each evanescent mode is defined by the profile of the complex refractive index over all the fiber cross-section with the imaginary part defined by (8).

In Fig. 5, the magnitudes of τ at different molar concentrations of acetone are shown: calculated separately for some

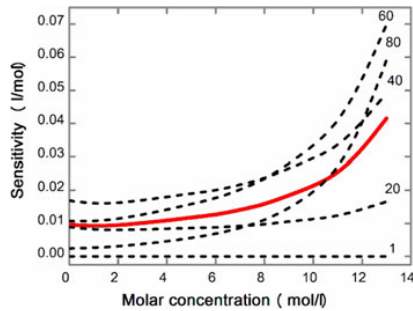Fig. 6.   Sensitivity (S) calculated at $\lambda = 3.33\,\mu$m for the HE_{1m} modes of the [GeSe$_4$]$_{95}$I$_5$ fiber with $m = 1, 20, 40, 60, 80$ (dashed lines) and by using (9) (solid line). $R = 145\,\mu$m, $L = 14$ cm.

evanescent modes (dashed curves) and calculated in approximation of equally distributed input power (solid curves) by using (9). Due to the stronger absorption of water rather than acetone, the transmittance grows with acetone concentration that is unusual in comparison with the absorption spectroscopy in VIS or NIR where an analyte has a stronger absorption than water.

In spite of $N = 114$ at $\lambda = 3.33\,\mu$m in the [GeSe$_4$]$_{95}$I$_5$ fiber immersed in the solution, we can see in Fig. 5 that some higher-order modes cannot reach the fiber output because of the stronger absorption. For example, transmittance of the 100-th evanescent mode is negligibly small at low concentrations of acetone. As in fact the input power was not equally distributed between the fiber modes at the input facet, actual number of the evanescent modes delivering power to the fiber output depends on both the initial amplitudes and attenuation coefficients of each mode. Then the 100-th mode of the [GeSe$_4$]$_{95}$I$_5$ fiber (and some other higher modes) might have a small amplitude and a small impact into the total transmittance. In our approximate calculations, indeed, the curve calculated by using (90 with $N = 80$ provides a good fit with the experimental results (Fig. 5), but the curve obtained with $N = 100$ is located much lower.

For sensitivity characterisation, the derivatives

$$S = d\tau/dc^a \qquad (11)$$

have been evaluated and plotted in Fig. 6 for several individual modes and for τ calculated by using (9) with $N = 80$. For the fundamental mode ($m = 1$) magnitudes of S are close to zero and do not depend on the acetone concentration. The mode with $m = 80$ is strongly absorbed by water at low acetone concentrations but at greater c^a its sensitivity increases because of partial replacement of water by acetone. In the range of concentrations $c^a = 0-2$ mol/l, magnitudes of S calculated by using (9), (11) at low c^a are defined mostly by the evanescent modes with m from 20 to 60. At larger concentrations, some higher-order modes, which has not been totally absorbed at $L = 14$ cm, impact into the total sensitivity.

In general, magnitudes of S depend on the slopes of the curves shown in Fig. 5, and the slopes depend on the difference between the pure water and pure acetone absorption coefficients at a given λ.

In addition to the HE_{1m} modes considered in this paper, other types of evanescent modes having potentially greater attenuation coefficients can be excited if an input light beam is not co-axial with the fiber. These modes are not azimuthally symmetric and correspond to tilted rays, which may have greater penetration into the absorbing medium.

V. Conclusions

We have applied a rigorous electrodynamics' model of a multimode optical fiber with an absorbing cladding for analysis of evanescent wave absorption in a chalcogenide fiber immersed in an aqueous acetone solution. Azimuthally symmetric evanescent modes of a single-index (unclad) fiber have been considered. We have demonstrated that higher-order modes of the fiber have greater attenuation coefficients than the lower-order ones because of greater penetration of the higher-order modes into the absorbing solution. By this, we have revealed that a selective excitation of the higher-order modes can be used for optimisation of fiber-optic sensing elements by decrease of the fiber length immersed into an absorbing medium.

As modal fields penetration into an absorbing cladding grows with decrease of the ratio of the fiber core radius to radiation wavelength, attenuation coefficient of an evanescent mode increases with wavelength. From this point of view, MIR spectral range is more attractive for evanescent wave sensing than VIS or NIR. This is especially important when using chalcogenide fibers, which generally have large refractive indices (2.4 or more). However strong absorption of water is a serious limitation in the MIR spectroscopy. To achieve high sensitivity, absorption coefficient of an analyte should by much greater than that one of pure water at a given wavelength.

For real-time remote sensing, supercontinuum sources are considered as a reasonable alternative to the heat sources used in laboratories. The supercontinuum sources provide coherent high-intensity radiation (more than three orders higher power spectral density than incoherent sources). Recently a new commercially available 1.7–4.2 μm mid-IR supercontinuum source has been presented by NKT photonics, thus representing a significant enhancement for spectroscopic applications. Furthermore a supercontinuum generation in chalcogenide fibers in the spectral range of 1–14 μm has been demonstrated in laboratory conditions [14], providing an excellent possibility for the future of the MIR spectroscopy.

References

[1] J. D. Musgraves, S. Danto, K. Richardson, and J. Hu, "Chalcogenide glass thin-film and fiber structures for chemical and biological sensing," in *Amorphous Chalcogenides: Advances and Applications*, R. Wang, Ed. Singapore: Pan Stanford Publ., 2014.

[2] R. R. Gattass *et al.*, "Review of infrared fiber-based components," *Appl. Opt.*, vol. 54, no. 31, pp. F25–F34, 2015.

[3] J. Heo, M. Rodrigues, S. J. Saggese, and G. H. Sigel, Jr., "Remote fiber-optic chemical sensing using evanescent-wave interactions in chalcogenide glass fibers," *Appl. Opt.*, vol. 30, no. 7, pp. 3944–3951, 1991.

[4] J. S. Sanghera, F. H. Kung, L. E. Busse, P. C. Pureza, and I. D. Aggarwal, "Infrared evanescent absorption spectroscopy of toxic chemicals using chalcogenide glass fibers," *J. Amer. Ceram. Soc.*, vol. 78, no. 8, pp. 2198–2202, 1995.

[5] K. Michel *et al.*, "Monitoring of pollutant in waste water by infrared spectroscopy using chalcogenide glass optical fibers," *Sensors Actuators B, Chem.*, vol. 101, pp. 252–259, 2004.

[6] P. S. Kumar, C. P. G. Vallabhan, V. P. N. Nampoori, V. N. Sivasankara Pillai, and P. Radhakrishnan, "A fibre optic evanescent wave sensor used for the detection of trace nitrites in water," *J. Opt. A, Pure Appl. Opt.*, vol. 4, pp. 247–250, 2002.

[7] L. S. Thomas *et al.*, "Chemical sensing with microbent optical fiber," *Opt. Lett.*, vol. 26, pp. 1541–1543, 2001.

[8] A. Messica, A. Greenstein, and A. Katzir, "Theory of fiber-optic, evanescent-wave spectroscopy and sensors," *Appl. Opt.*, vol. 35, no. 13, pp. 2274–2284, 1996.

[9] Y. Xu, A. Cottenden, and N. Barrie Jones, "A theoretical evaluation of fibre-optic evanescent wave absorption in spectroscopy and sensors," *Opt. Lasers Eng.*, vol. 44, pp. 93–101, 2006.

[10] A. W. Snyder and J. D. Love, *Optical Waveguide Theory*. London, U.K.: Chapman & Hall, 1983.

[11] L. A. Melnikov and E. A. Romanova, "Transformation of HE1m guided mode into the leaky one in absorbing optical fiber," *Opt. Commun.*, vol. 141, pp. 10–16, 1997.

[12] A. P. Velmuzhov *et al.*, "Preparation and investigation of [GeSe4]100xIx glasses as promising materials for infrared fiber sensors," *Opt. Mater.*, vol. 60, pp. 438–442, 2016.

[13] G. Boudebs *et al.*, "Linear optical characterization of chalcogenide glasses," *Opt. Commun.*, vol. 230, pp. 331–336, 2004.

[14] C. R. Petersen *et al.*, "Mid-infrared supercontinuum covering the 1.4–13.3 μm molecular fingerprint region using ultra-high NA chalcogenide step-index fibre," *Nature Photon.*, vol. 8, pp. 830–834, Nov. 2014.

Elena A. Romanova received the Ph.D. degree in optics and the Dr.Sc. degree in laser physics from the Saratov State University, Saratov, Russia, in 1988 and 2004, respectively. She is currently a Professor at the Chair of Computational Physics and Metamaterials, Saratov State University. She spent one year in research at the University of Nottingham as a Marie Curie Fellow. She specializes in theory and modeling of laser beams and pulses propagation in linear and nonlinear dielectric waveguides and optical fibers. Her research interests include the study of nonlinear optical response of noncrystalline semiconductors and the development of the technology of optical materials processing by the ultrashort laser pulses. She has been involved into several research projects supported by the European Commission and the Royal Society.

Svetlana Korsakova received the M.S. degree in laser physics and nonlinear optics from the Faculty of Physics, Saratov State University, Saratov, Russia, in 2015, where she is currently working toward the Ph.D. degree in the Faculty of Physics. Her research interests include fiber sensing, IR-spectroscopy, and computer modeling.

Matej Komanec received the M.S. and Ph.D. degrees in radioelectronics from the Czech Technical University in Prague, Prague, Czech Republic, in 2009 and 2014, respectively, where he is currently a Research Assistant at the Faculty of Electrical Engineering. His research interests include specialty optical fibers, nonlinear optics, optical interconnects, and fiber sensing. He is a member of OSA and SPIE.

Tomas Nemecek received the M.S. degree in radioelectronics from the Faculty of Electrical Engineering, Czech Technical University in Prague, Prague, Czech Republic, in 2013, where he is currently working toward the Ph.D. degree. His research interests include fiber sensing, specialty fibers, and measurement techniques. He is a member of SPIE.

Alexander Velmuzhov received the Graduate (Hons.) degree from the Department of Inorganic Chemistry, Nizhniy Novgorod State University, Nizhniy Novgorod, Russia, in 2009. In 2009, he started a postgraduate course in the Institute of Chemistry of High-Purity Substances, Russian Academy of Sciences and began to work in the Laboratory of Chemistry of the High-Purity Non-Oxide Glasses. In March 2012, he defended his Ph.D. thesis on "Preparation of Special Pure Ge-Sb-S(Se)-I Glass Systems Via Volatile Iodides of Germanium and Antimony." His research interests include high-purity substances, optical materials, inorganic chemistry, optical spectroscopy, thermodynamics simulations, infrared glasses, and iodids and chalcogenids of p-elements. Main results of his research work were published in 22 scientific publications.

Maksim Sukhanov received the Graduate degree from the Department of Inorganic Chemistry, Nizhniy Novgorod State University, Nizhniy Novgorod, Russia, in 2003 and the Ph.D. degree in chemistry in 2006. Since 2010, he has been working as a Senior Researcher in the Laboratory of Chemistry of the High-Purity Non-Oxide Glasses, Institute of Chemistry of High-Purity Substances, Russian Academy of Sciences. His research interests include high-purity substances, optical materials, inorganic chemistry, optical spectroscopy, infrared glasses, and isotopes and chalcogenide glasses. Main results of his research work were published in 35 scientific publications.

Vladimir S. Shiryaev received the Graduate degree from the Department of Applied Physics and Microelectronics, Nizhny Novgorod State University, Nizhny Novgorod, Russia, in 1983 , the Ph.D. degree in chemistry in 1992, and the Dr.Sc. degree in chemistry in 2007. Since 1985, he has been working in the Laboratory of Chemistry of the High-Purity Non-Oxide Glasses, Institute of Chemistry of High-Purity Substances, Russian Academy of Sciences, Nizhniy Novgorod, Russia. Since 1996, he has been a Lecturer in optical fibers and chemistry of glassy state, Nizhny Novgorod State University. He is involved in several international research programs. He has more than 180 scientific articles and contributed papers. He has been involved in research work on the preparation and investigation of various properties of infrared transmitting glasses for ultralow-loss fiber optics. His current research interests include synthesis and investigation of chalcogenide and fluoride glasses, and preparation of low-loss optical fibers (multimode, single-mode, microstructured, activated with REE).

4.2 Multimode fiber tapers for reproducible refractometric liquid detection

This chapter is a version of the published manuscript:

[J2]: M. Komanec, T. Martan, T. Nemecek, and S. Zvanovec, "Multimode fiber tapers for reproducible refractometric liquid detection", OPTICAL ENGINEERING, vol. 54, no. 4, 2015.

Relevance to my Ph.D. thesis:

To detect hazardous liquid analytes in explosive or flammable environments, a non-electrical sensing unit is necessary and optical fibers present an advantageous solution. If the environment is chemically aggressive, the sensor principle must avoid non-resistant opto-chemical transducers, furthermore, for widespread application, a facile sensing approach is desired. Refractometric sensors based on optical fibers present such an option. The refractometric principle is highly dependent on evanescent-wave overlap in terms of sensitivity and resolution. TOFs thus allow desired sensor performance. In this paper, MM TOFs have been analyzed. Polymer-clad silica and graded-index MM fibers have been evaluated. A significant number of TOF samples has been prepared leading to the improvement and optimization of TOF sensor preparation reproducibility, measurement repeatability, and also long-term stability. For the first time, in terms of trends of sensitivity and relative power, the loss was given in correlation with MM TOF waist diameters, allowing us to identify peak and saturation sensitivity points related to the waist diameter for selected MM fiber types. This paper led to the definition of an optimal TOF waist diameter for achieving maximum sensitivity, supported by measurements and simulations.

Multimode fiber tapers for reproducible refractometric liquid detection

Matej Komanec
Tomas Martan
Tomas Nemecek
Stanislav Zvanovec

Multimode fiber tapers for reproducible refractometric liquid detection

Matej Komanec, * **Tomas Martan, Tomas Nemecek, and Stanislav Zvanovec**
Czech Technical University in Prague, Department of Electromagnetic Field, Faculty of Electrical Engineering, Technicka 2, Prague 16627, Czech Republic

Abstract. This paper describes the refractometric detection of liquids based on silica multimode optical fibers which were tapered to increase the evanescent-wave overlap for higher sensor sensitivity. By precisely monitoring the production process, consistent sample parameters were achieved. More than 200 tapers with a taper waist diameter range from 6.0 to 76.3 μm were prepared from polymer-clad silica and gradient-index multimode fibers. U-shaped fiber taper sensitivities were analytically compared with straight tapers with resulting intensity sensitivities of over 200%/RIU. Crucial parameters for real sensor applications, such as measurement repeatability, reproducibility, and long-term stability, were further studied for polymer-clad silica straight tapers. Long-term stability was monitored showing stable measurement results over a 6 months long interval. Measurement repeatability and reproducibility with standard deviations of 0.55%/RIU and 2.26%/RIU, respectively, were achieved. © *2015 Society of Photo-Optical Instrumentation Engineers (SPIE)* [DOI: 10.1117/1.OE.54.4.047102]

1 Introduction

Fiber optic liquid detection represents remarkable advantages in comparison, for instance, with semiconductor and electronic detection. The advantage of optical fibers lies in their immunity to surrounding electromagnetic fields. Additionally, optical silica fibers can withstand high temperatures and are resistant to a variety of chemical substances. Therefore, fiber optic sensors can be employed in extreme conditions, e.g., in explosive environments or in areas with high electromagnetic disruption.

Detection of liquids based on evanescent-wave overlap into measured analytes exploiting tapered optical fibers has been extensively studied for the last two decades. Refractometers employing tapered optical fibers were first presented[1] in a detailed study of evanescent-field overlap. More sophisticated refractometric applications have since been proposed including the tapered microstructured optical fiber refractometer presented in our previous work,[2] which features a tapered suspended-core microstructured optical fiber and an evanescent-field overlap which substantially increased from 0.29% to 29.16%.

The singlemode-multimode-singlemode (SMS) sensing structure represents a facile approach to enhancement of evanescent-wave overlap including a segment of multimode fiber between two single-mode fibers, resulting in optical mode spreading and subsequent interference in the multimode segment. A detailed study of in-line production monitoring and liquid sensing based on SMS structures was presented,[3] where 2946 nm/RIU (refractive index unit) was attained for tested analytes having a refractive index range of 1.42 to 1.43.

Surface plasmon resonance (SPR) refractometers were developed in parallel to tapered optical fiber-based refractometers allowing us to present achievements in extreme sensitivities and resolutions comparable to tapered fibers. In this scenario, SPR refractometers employing polymer-clad silica (PCS) fibers,[4] tapered fibers with multiple layers deposited,[5] and long-period grating sensors[6] were used. However, SPR refractometers require a multistep manufacturing process and more complex measurement configuration.

Tapered optical fiber sensors (TOFSs) are utilized either in transmissive[7] or reflective regimes,[8] whereas the sensor shape can be further tailored.[9] Furthermore, abrupt tapers (multiple in-line tapers on a single fiber) forming a Mach–Zehnder configuration were utilized for liquid sensing.[10]

Facile high-quality fabrication will determine the future success of TOFS applications. This paper focuses on straight and U-shaped polymer-clad silica TOFS for detecting liquids in the visible range and compares and analyzes conventional gradient-index multimode TOFS with polymer-clad silica TOFS. Our earlier studies[11,12] have been considerably extended, simulations have been carried out to provide preliminary results, prepared samples have been summarized and the measurement setup is, herein, described. Taper production quality and tapering process conditions are discussed, with a particular emphasis placed on stable taper parameters. A sensitivity analysis for all measured TOFS follows. Measurement repeatability (for a standalone TOFS) and measurement reproducibility (for a set of three TOFS) are studied in three consequent measurement cycles. Long-term stability, tested in periods of up to 6 months, is then presented. Our developed detection units can be employed as key instruments e.g., in petrochemical, automobile, or food industries.

2 Simulations

Preliminary simulations were carried out in the Synopsys BeamProp software for polymer-clad silica TOFS (PCS TOFS)

*Address all correspondence to: Matej Komanec, E-mail: komanmat@fel.cvut .cz
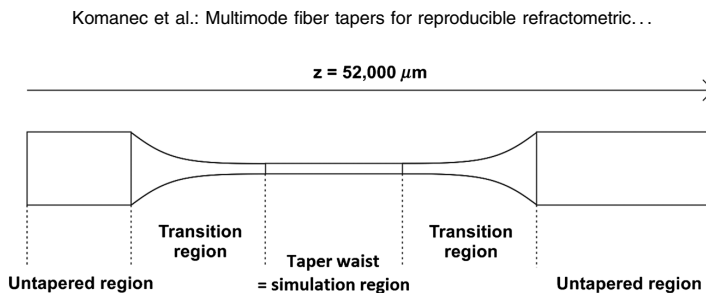
Fig. 1 Model of a taper structure with the taper waist as the simulation region.

of 200-μm outer diameter. The selected waist diameters were 3, 4, 5, 6, 8, 10, 15, and 20 μm, with the wavelength set at 632 nm. The full transparent boundary condition and a grid size notably below the evaluated wavelength were considered. In the simulations, external mediums with refractive index of 1.432, 1.380, and 1.361 were used to simulate ethylenglycol (EG), isopropylalcohol (IPA), and ethylalcohol (ETOH), respectively. The taper structure, set according to a real taper, is depicted in Fig. 1. For the simulation, we assumed an adiabatic transition region, all modes propagating (multimode launch field defined by the silica/cladding-polymer refractive indices) and only the taper waist was considered as the sensing region. One of the major parameters of tapers represents the tapering ratio, which defines how many times the final waist diameter is reduced to the original fiber diameter, as utilized e.g., by Kerttula et al.[13]

The relative power loss summarized in Fig. 2, obtained for all three analytes and chosen waist diameters, occurs when higher propagating modes are being radiated into the analyte and no longer guided in the TOFS. Areas I and II depict a relative power loss saturation point where, for a particular waist diameter range, the evanescent-field overlap does not increase. If further tapered toward narrower diameters, most of the guided energy is transferred into higher (evanescent) modes and consequently radiated into the analyte with respect to the refractive index of the analyte. The saturation area is a boundary between the original mode set propagating in the untapered PCS (which is defined by silica/cladding-polymer refractive indices and is preserved for lower tapering ratios) and full mode excitation in the
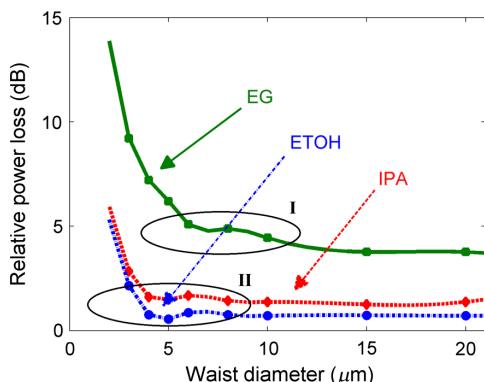
case of a tapering ratio higher than approximately 15 for EG and 20 for IPA and ETOH.

3 Measurement Setup

All measurements were carried out in the wavelength range 450 to 1000 nm. The measurement setup included a broadband light source with a 2 m-long 200PCS fiber attached at the generator side. A calibration fiber and a mode stripper were inserted between the light source and the detector segment. For each fiber type, an appropriate calibration fiber (e.g., 125PCS in case of the 125PCS TOFS measurement) was employed. Afterward, TOFSs were inserted between the calibration fiber and the mode stripper. The detection was performed by a spectral analyzer with a 2 m-long 200PCS fiber attached. The measurement setup is depicted in Fig. 3.

4 Prepared Samples

Three conventional fiber types were used for fiber tapering: (1) Corning multimode 62.5/125 μm gradient-index fiber (62.5 MM), (2) CeramOptec Optran HWF 125/140 μm hard polymer-clad silica fiber (125PCS), and (3) CeramOptec Optran HWF 200/230 μm hard polymer-clad silica fiber (200PCS), which was the same as that considered in simulation. The 200PCS fiber was chosen based on simulations with the 125PCS fiber to provide comparisons in sensitivity and tapering limits. The 62.5MM fiber was selected as a representative of a conventional core/clad composition with a maximum core size typically available, while having a gradient-refractive index profile. A modified tapering technique, developed in our previous work,[14] where flame-heating, in conjunction with two synchronized motors pulling the fiber evenly in the opposite directions, was employed. We have utilized the exponential-linear taper profile which was also employed by Verma et al.[15] for SPR sensing, where a taper profile study was performed and the taper profile resulted in further improvement of the measurement sensitivity.

TOFS waist diameters from 79 μm to less than 10 μm were developed for enhanced evanescent-wave overlap with the selected analytes. The largest core diameter tapering ratio of almost 20 was achieved in the case of 200PCS fibers. For 125PCS fibers and 62.5MM fibers, the tapering ratios were approximately 15 and 10, respectively. Developed TOFSs were divided into four sets of waist diameters. For each TOFS set, at least five TOFSs were produced. Enhanced sensitivity was first achieved by fiber tapering and, further by shape-tailoring. U-shaped tapers were formed by preparing straight tapers and subsequently applying the U-profile, ensuring comparable outputs could be obtained for the same taper diameters in straight and

Fig. 2 Simulation results for 2-mm long taper waist immersed in selected analytes—dependence of relative power loss on waist diameter. Areas I and II depicting a saturation region.
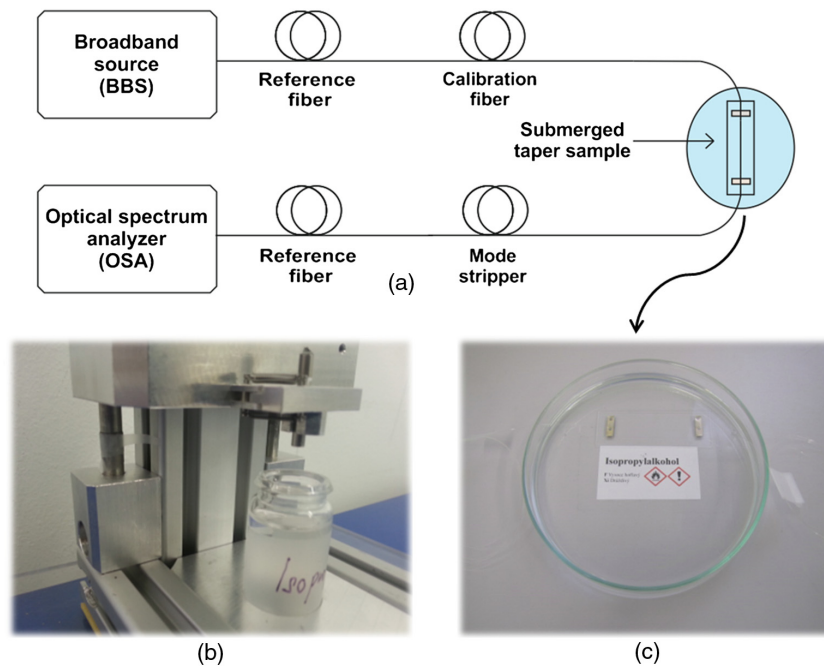
Fig. 3 Measurement setup for liquid sensing, (a) setup configuration; (b) a mini-tower for U-shaped tapered optical fiber sensor (TOFS) immersion; (c) immersion of straight TOFS.

U-shaped variants. A summary of the TOFS prepared is presented in Table 1.

For the U-shaped tapers, the radius was experimentally derived as the closest radius to the breakage point with emphasis on maintaining a repeatable radius (for all samples of a given fiber tapering ratio and fiber type). Table 2 summarizes the bending radii for all TOFSs, excluding the 47.5 μm 62.5MM TOFS, which it was not possible to shape-tailor and the 8.3 μm 125PCS TOFS where we experienced frequent breakage. The U-shape was conserved with a metallic tube located at the untapered part of the fiber, thus creating a fixed loop. A clear relation between the bending radius and tapering ratio can be observed – the higher the tapering ratio is set the smaller the bending radius that can be used, thus increasing sensitivity. The insertion loss of the detection unit also increases with bending radius, but since a reference for each measurement is utilized, this power loss can be neglected.

5 Results

Selected TOFSs were first submerged in IPA for approximately 5 min to remove small dust particles. To employ

Table 1 Taper waist diameters of utilized tapered optical fiber sensor (TOFS) sets.

	Taper waist diameters (μm)			
62.5MM	6.0	12.0	23.2	47.5
125 PCS	8.3	18.5	30.8	54.1
200 PCS	10.9	20.3	42.1	76.3

the TOFS after long-term storage, i.e., several months, a 30-minute purification period was utilized. Then a reference spectrum was recorded for TOFS exposed to air. Spectra were later recorded while the TOFSs were submerged in analytes: ETOH, IPA, and EG. A final spectrum was acquired for purified TOFS after the measurement cycle (again in IPA, to remove residual EG) with the temperature kept constant during the whole measurement cycle. Figure 4 illustrates an example of such a measurement. The figure shows the

Table 2 U-shaped TOFS bending radius summary.

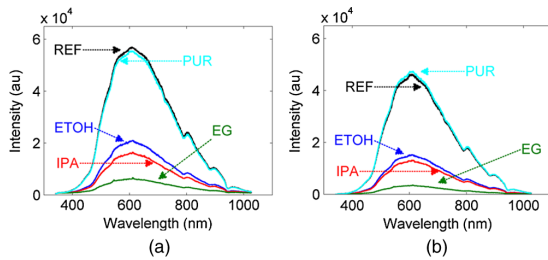|	Taper waist diameter (μm)	Bending radius (mm)
62.5MM	6.0	1.25
	12.0	1.32
	23.2	1.65
125PCS	18.5	0.92
	30.8	1.50
	54.1	1.62
200PCS	10.9	0.72
	20.3	1.11
	42.1	1.57
	76.3	1.70

Fig. 4 Measured spectra for (a) straight and (b) U-shaped 200PCS 20.3 μm TOFS, REF—reference measurement, PUR — purification after measurement cycle.

measured spectra of the same 200PCS 20.3 μm TOFS, both in straight and U-shaped variants.

At first, we determined a significant parameter of the TOFS — the critical waist taper diameter. It was derived from the measured relative power loss for all 200PCS TOFS sets, both in straight and U-shaped variants (see dependences of average measured values with limits of minimum and maximum values reached in Fig. 5). The relative power loss represents a difference between the reference power level and power received after immersion in the analyte (ETOH, IPA, and EG) at the detector at 632 nm, which was derived from our spectral measurements. As can be seen, the measured relative power loss in the case of straight 200PCS TOFS saturates at a diameter of approximately 20 μm (marked areas in Fig. 5).

A similar phenomenon is observed for U-shaped 200PCS TOFS, where the saturation waist diameters are shifted to larger values, which is caused by the TOFS shape inducing a greater evanescent wave overlap.

5.1 Production Process Enhancement

To evaluate and enhance the production level, four sets (of three TOFS each) were produced from 125PCS and 200PCS fibers under monitored conditions. The best results were obtained for the 125PCS 21 μm TOFS set, with a waist diameter standard deviation of 0.25 μm. High-quality production was assured by maintaining stable production conditions, in particular, flame and ambient temperatures. The maximum fluctuation in ambient temperature was below 0.5°C during the manufacturing of all TOFS sets.
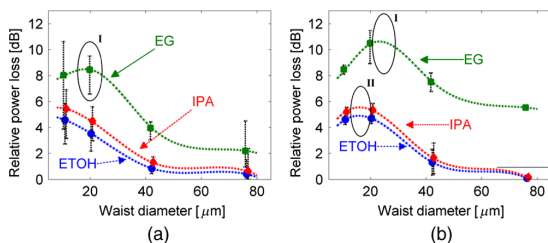
5.2 Sensitivity Study

An intensity sensitivity analysis was used to compare obtained results with the intensity sensitivity (S) evaluated as[8]

$$S = \frac{\Delta I/I_0}{\Delta n} \times 100 (\%/\text{RIU}),\qquad(1)$$

where ΔI stands for the analyte/reference measured intensity difference, I_0 represents the measured reference intensity, and Δn is the analyte/reference refractive index difference.

Figure 6 summarizes the maximum intensity sensitivities for the 200PCS TOFS sets at 632 nm. Here, it is more evident that, for all analytes, the sensitivity saturates around a waist diameter of 17 μm for straight TOFS and 20 μm for U-shaped TOFS. For straight TOFS, the values at the waist diameter of 76.3 μm for IPA are approximately 10%/RIU higher than for 42.1 μm, which is attributed to a measurement error because other intensity sensitivities show no variation in the 76.3 to 42.1 μm region. For U-shaped TOFS, the trend is linear and saturates at the same waist diameter as that of straight TOFS. Based on the results, an optimal tapering ratio in our experiment was derived to be 10 for 200PCS TOFS.

Derived maximum intensity sensitivities for the case of 125PCS TOFS sets are then presented in Fig. 7. Here, the saturation point can be found for waist diameters of approximately 25 μm for both straight and U-shaped variants (marked as area I). An interesting result was revealed for the U-shaped 125PCS TOFS sets submerged in EG, where we observed an almost independent intensity sensitivity on the change of the waist diameter. Therefore, for utilization of

Fig. 6 Maximum intensity sensitivity of 200PCS TOFS sets: (a) straight and (b) U-shaped TOFS. Area I depicts the optimal waist diameter for highest sensitivity.

Fig. 5 Relative power loss for 200PCS TOFS sets: (a) straight and (b) U-shaped TOFS. Areas I and II depicting a saturation region.
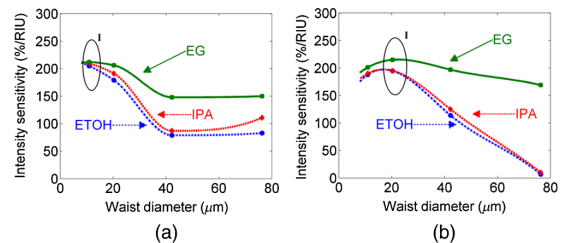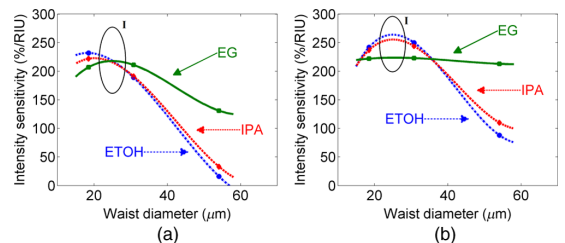

Fig. 7 Maximum intensity sensitivity of 125PCS TOFS sets: (a) straight and (b) U-shaped TOFS. Area I depicts the optimal waist diameter for highest sensitivity.
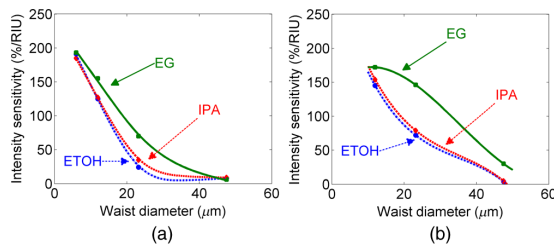
Fig. 8 Maximum intensity sensitivity of 62.5MM TOFS sets: (a) straight and (b) U-shaped TOFS.

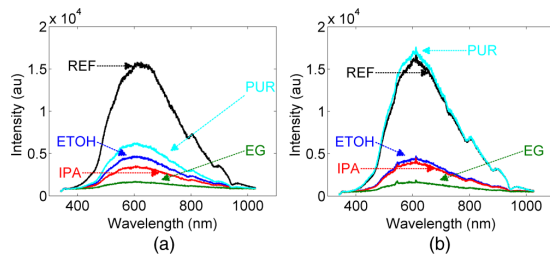**Fig. 9** Measured spectra of a straight 200PCS 10.9 μm TOFS measured (a) 4 months and (b) 6 months after production, REF — reference measurement, PUR — purification after measurement cycle.

such a sensor, a considerably lower tapering ratio could be required.

In comparison, intensity sensitivities of 62.5MM TOFS are depicted in Fig. 8. Here we observe, as expected, straight TOFS sets without any observable saturation in sensitivity. For the U-shaped 62.5MM TOFS, for EG detection only, saturation is evident. Therefore, to achieve an optimal waist diameter for straight and U-shaped TOFSs, a higher tapering ratio than 10 is required.

Resolutions for the most sensitive TOFS of each fiber type were evaluated both in straight and U-shaped variants, respectively. The results are summarized in Table 3 with the sensitivity values as comparisons.

5.3 Measurement Repeatability and Reproducibility

To verify production results and their impact on measurement output further, the 125PCS 21 μm TOFS set was selected and for a standalone TOFS of this set three

Table 3 Resolution and maximum sensitivity for measured TOFS.

	Taper waist diameter (μm)	Profile	Maximum sensitivity (%/RIU)	Resolution (RIU)
62.5MM	6.0	Straight	193 (EG)	1.3×10^{-2}
	6.0	U-shaped	172 (EG)	3.3×10^{-3}
125PCS	18.5	Straight	232 (ETOH)	2.5×10^{-3}
	18.5	U-shaped	242 (ETOH)	1.1×10^{-3}
200PCS	10.9	Straight	212 (EG)	2.0×10^{-3}
	20.3	U-shaped	215 (EG)	1.7×10^{-3}

subsequent measurement cycles were carried out to prove measurement repeatability. The standard deviations for standalone TOFSs were 7.17%/RIU for ETOH, 4.45%/RIU for IPA, and 0.55%/RIU for EG.

Measurement reproducibility, i.e., obtaining the same results for different TOFSs of the same set, was evaluated for the whole 125PCS 21 μm TOFS set. For this purpose, we compared all the TOFS intensity sensitivities acquired and a standard deviation of 10.71%/RIU for ETOH, 8.11%/RIU for IPA, and 2.26%/RIU for EG was observed.

Results indicate 125 μm PCS TOFS (all tested variants) as ideal candidates for stable and repeatable sensing, in particular, for EG detection with a reproducibility deviation below 2.5%/RIU for the entire set and a repeatability deviation below 0.6%/RIU for standalone samples. For ETOH and IPA, the results allude to an application with less precise requirements. The overall difference between a standalone TOFS and the whole TOFS set is only several %/RIU, which further verifies the quality of our production process.

5.4 Long-Term Stability

Long-term stability was tested for a chosen TOFS within a time period of 6 months. Figure 9 depicts the spectra from the 10.9 μm 200PCS TOFS measured 2 months apart. During the first measurement cycle [see Fig. 9(a)], the TOFS was insufficiently purified after submerging in EG. After 4 months of storage we were able, by additional pre-measurement purification, to remove all residual impurities.

6 Conclusion

We presented straight and U-shaped multimode tapered fibers for liquid sensing. Special emphasis was placed on multimode polymer-clad silica fibers' sensitivity, optimal waist diameter, and their measurement repeatability, measurement reproducibility, and long-term stability.

The production process was perfected with a taper waist standard deviation below 0.25 μm when manufacturing conditions were monitored and precautions, in particular with temperature, were taken. Further enhancement of taper parameter stability is possible with a more precise ambient temperature and relative humidity control.

Measurement results showed significant trends, such as saturation points in intensity sensitivities for different fiber types and analytes, and we defined an optimal taper waist for achieving maximum intensity sensitivity while keeping the tapering ratio as low as possible. For 125PCS fiber, a waist diameter of 25 μm with an intensity sensitivity over 200%/RIU is optimal. For the 200PCS fiber, the optimal waist diameter value is 11 μm with an intensity sensitivity again over 200%/RIU.

Measurement repeatability (for a standalone TOFS) was greatly increased for TOFS experiencing the monitored production process. The intensity sensitivity standard deviation measured below 8%/RIU for ETOH, 5%/RIU for IPA, and 1%/RIU for EG. This result leads to a promising application for precise liquid sensing with a refractive index in the range of 1.41–1.44 RIU. Long-term stability was examined and we have achieved more than 6 months' long-term stability.

In contrast to wavelength-based sensors such as SPRs, our TOFSs require only a single-step manufacturing process (double-step for U-shaped TOFS) and represent a low-cost option (cheap sensor, only a simple laser source and a

Komanec et al.: Multimode fiber tapers for reproducible refractometric...

detector are needed) with reasonable sensitivity and stable measurement results. To conclude, a facile manufacturing process of tapered polymer-clad silica fiber sensors was presented, with optimized sensitivity, measurement repeatability, and reproducibility and proven long-term stability for liquid detection in the refractive index range of 1.36 to 1.43.

Acknowledgments

References

1. S. Huntington et al., "Evanescent field characterisation of tapered optical fibre sensors in liquid environments using near field scanning optical microscopy and atomic force microscopy," *IEE Proc. Optoelectron.* **146**(5), 239–243 (1999).
2. T. Martan et al., "Tapered optical fibres for sensing," *Proc. SPIE* **7138**, 71380Z (2008).
3. C. R. Biazoli et al., "Multimode interference tapered fiber refractive index sensors," *Appl. Opt.* **51**, 5941–5945 (2012).
4. S. K. Srivastava, R. Verma, and B. D. Gupta, "Surface plasmon resonance based fiber optic sensor for the detection of low water content in ethanol," *Sens. Actuators B* **153**(1), 194–198 (2011).
5. R. Jha, R. Verma, and B. Gupta, "Surface plasmon resonance-based tapered fiber optic sensor: sensitivity enhancement by introducing a teflon layer between core and metal layer," *Plasmonics* **3**(4), 151–156 (2008).
6. C.-L. Tien et al., "Double-sided polishing long period fiber grating sensors for measuring liquid refractive index," presented at *Asia Communications and Photonics Conf. on Exhibition*, Paper WL93, pp. 1–6, Optical Society of America, Shanghai, China (2009).
7. P. Wang et al., "Enhanced refractometer based on periodically tapered small core single mode fiber," *IEEE Sens. J.* **13**, 180–185 (2013).
8. Y.-H. Tai and P.-K. Wei, "Sensitive liquid refractive index sensors using tapered optical fiber tips," *Opt. Lett.* **35**, 944–946 (2010).
9. E. OConnell et al., "Low cost hydrocarbon spillage sensor for the marine environment with interfacing to a mote platform," in *Proc. 2011 IEEE Sensors* pp. 1558–1561 (2011).
10. C.-L. L. Hun-Pin Chang, Chai-Ming Li and J.-M. Hsu, "Tapered fiber Mach–Zehnder interferometer for liquid level sensing," in *Proc. Progress in Electromagnetics Research Symposium*, Vol. 2528, pp. 734–736, Taipei (2013).
11. M. Komanec, T. Martan, and S. Zvanovec, "Tapered optical fibers for reproducible detection of liquids," presented at *Advanced Photonics 2013*, Paper JT3A.31, Optical Society of America, Río Grande, Puerto Rico (2013).
12. M. Komanec, T. Martan, and S. Zvanovec, "Polymer-clad silica tapers for liquid sensing: long-term measurement repeatability and production imperfections," presented at *Advanced Photonics*, Paper JM5A.63, Optical Society of America, Barcelona, Spain (2014).
13. J. Kerttula et al., "Mode evolution in long tapered fibers with high tapering ratio," *Opt. Express* **20**, 25461–25470 (2012).
14. T. Martan et al., "Workplace for manufacturing devices based on optical fiber tapers," *Proc. SPIE* **6609** 66090K (2007).
15. R. K. Verma, A. K. Sharma, and B. Gupta, "Surface plasmon resonance based tapered fiber optic sensor with different taper profiles," *Opt. Commun.* **281**(6), 1486–1491 (2008).

Matej Komanec is a research assistant at the Faculty of Electrical Engineering of the Czech Technical University in Prague. He received his MS and PhD degrees in radioelectronics from the Czech Technical University in Prague in 2009 and 2014, respectively. His current research interests include specialty optical fibers, nonlinear optics, optical interconnects, and fiber sensing. He is a member of OSA.

Tomas Martan is a research assistant at the Faculty of Electrical Engineering of the Czech Technical University in Prague. He received MS and PhD degrees in radioelectronics from the Faculty of Electrical Engineering of the Czech Technical University in Prague in 2001 and 2006, respectively. His current research interests include specialty fibers, optical fiber sensing, optoelectronics, and optical spectroscopy.

Tomas Nemecek is a PhD student at the Faculty of Electrical Engineering of the Czech Technical University in Prague. He received his MS degree in radioelectronics from the Faculty of Electrical Engineering of the Czech Technical University in Prague, in 2013. His current research interests include fiber sensing, specialty fibers, and measurement techniques.

Stanislav Zvanovec has been a professor at the Faculty of Electrical Engineering of the Czech Technical University in Prague since 2014. He received his MS and PhD degrees in radioelectronics from the Faculty of Electrical Engineering of the Czech Technical University in Prague in 2002 and 2006, respectively. His current research interests include fiber sensors and visible light communicatons.
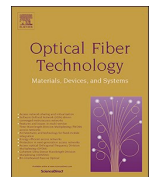
4.3 Structurally-modified tapered optical fiber sensors for long-term detection of liquids

This chapter is a version of the published manuscript:

[J3]: M. Komanec, T. Nemecek, P. M. Vidner, T. Martan, F. Lahodny, and S. Zvanovec, "Structurally-modified tapered optical fiber sensors for long-term detection of liquids", OPTICAL FIBER TECHNOLOGY, vol. 47, pp. 187 –191, 2019

Relevance to my Ph.D. thesis:

Results from previous Chapter 4.2 have been extended, where improvement of sensitivity by surface structural modification has been investigated. Structural modification was achieved by subsequent TOF hydrogenization and drying, leading to sol-gel development in the single-mode TOF surface layer. Characteristics of this process have been examined, leading to significant sensitivity enhancement of up to ten times. A 12-months continuous measurement campaign with two TOF sensor samples and a liquid analyte of variable RI, has been carried out. The liquid analyte slowly increased in RI via evaporation and was deliberately diluted to obtain a series of measurement cycles in the desired RI range. The single-mode TOF sensors were linearly calibrated. The long-term experiment verified sensor stability.

Structurally-modified tapered optical fiber sensors for long-term detection of liquids

Matej Komanec[a,*], Tomas Nemecek[a], Premysl Michal Vidner[a], Tomas Martan[a], Frantisek Lahodny[b], Stanislav Zvanovec[a]

[a] *Department of Electromagnetic Field, Faculty of Electrical Engineering, Czech Technical University in Prague, Technicka 2, Prague 6 166 27, Czech Republic*
[b] *Department of Glass and Ceramics, Faculty of Chemical Technology, University of Chemistry and Technology, Technicka 5, Prague 6 166 27, Czech Republic*

A B S T R A C T

We present an improvement of tapered optical fiber (TOF) sensor's response for the detection of liquids, which is achieved by TOF surface structural modification. Our TOF sensors utilize the refractometric principle with enhanced evanescent-wave overlap due to the wavelength of 1550 nm and TOF waist diameters of 4–6 μm. The structural modification is achieved by long-term TOF exposition to hygroscopic liquid analytes and ambient atmosphere. To analyze the structural modification process, long-term as well as proof-of-principle tests have been carried out to evaluate TOF sensors stability in terms of sensitivity and resolution. Maximum sensitivity of over 2100 dB/RIU has been reached when TOF is used to detect a liquid analyte with refractive index of 1.415. Increase of more than 1400 dB/RIU is attributed to the enhanced sensitivity. Sample TOF sensors were then linearly calibrated and have been tested in more than one year-long continuous measurement campaign. Resolution better than $7 \cdot 10^{-4}$ for a refractive index range of from 1.405 to 1.425 with working point drift below $2 \cdot 10^{-4}$ over 12 months period has been achieved. Our results and observations are suitable for reliable, low-cost and application-tailored TOF sensor development.

1. Introduction

Refractometric detection of liquids based on tapered optical fibers (TOFs) with an enhanced evanescent-wave overlap has been extensively studied, and a variety of configurations have been proposed [1–7]. The key difference of these measurement techniques lies in the intensity-based or the wavelength-shift-based measurement techniques. Wavelength-shift-based TOF sensors generally provide better performance in terms of sensitivity and resolution, on the other hand, they require a more complex processing system. Wavelength-shift-based TOF sensors utilizing periodically tapered fibers [1,2] with sensitivities up to 4000 nm/RIU at a refractive index (RI) of 1.45 were presented in [1]. An average sensitivity of 226 nm/RIU in the RI range from 1.33 to 1.38 was achieved in [2]. Microresonators with a sensitivity of 95.5 nm/RIU in the 1.38 to 1.41 RI range were demonstrated in [3]. To enhance sensor sensitivity, the TOF sensor was further shape-tailored in [4] resulting in $8.0 \cdot 10^{-5}$ RIU resolution in the RI range of 1.38–1.44. In-line production monitoring and liquid sensing based on single mode-multimode-single mode (SMS) structures were presented in [5] with a sensitivity of 2946 nm/RIU in the RI range of 1.42–1.43. Surface plasmon resonance (SPR) refractometers have also been developed in

parallel while utilizing TOFs [6].

Intensity-based sensors remove the wavelength-shift-based sensor demands on the processing system and the complexity of SPR sensor preparation [6,8]. TOF sensors with ultra-thin tapered fiber tips with sensitivities over 8000%/RIU have been presented in [7]. Surface functionalization by additional layer deposition [9] or interferometric configuration can further increase TOF sensor performance but under cost of increased complexity. We have recently demonstrated a possible application of suspended-core microstructured optical fibers for the detection of liquids with a sensitivity of 342 dB/RIU at RI of 1.43 [10].

To provide a facile approach for the detection of liquid analytes, conventional silica single-mode TOF sensors can be applied as they further diminish the disadvantages of both intensity and wavelength-shift-based sensors, such as utilization of specialty optical fibers [1] and sensors' structure fragility [3,10].

Stability and long-term performance of TOFs have been studied only under laboratory conditions and from a short-term point of view within the range of multi-day time periods. An interesting evaluation of TOF degradation was presented in [11], where the primary contribution to the increase of TOF attenuation is attributed to dust particles attached to the nanotaper surface manifesting as scattering loss. The greatest

---

impact was experienced in standard room conditions where, in the case of a TOF with 460 nm waist diameter, dust particles caused almost 10 dB attenuation within a time period of less than 10 h. The effects of humidity were found to be negligible in this study. Crack formations and their degradation effect on TOFs together with the humidity-induced hydrogen-bond formation and further attenuation increase was subsequently summarized in [12] for long microfibers. A 5 dB attenuation increase caused by 18 h long crack formation in a microfiber with a 2 μm waist diameter was observed in [12]. However, none of these publications have described any relation between TOF degradation and sensor performance for the detection of liquids.

This paper presents, for the first time, a long-term evaluation of TOF sensors for refractometric detection of liquids with focus on TOF surface structural modification. We analyze sensitivity enhancement and overall sensor response curve shift. We report on significant sensitivity enhancement, without any need for sol–gel or other functional layer deposition. We study freshly-produced TOF sample versus a structurally-modified TOF sample and we observe similar resolution with a significant shift of the sensors' response curve. Last a linear calibration is applied for selected TOF sensors, and results from sensor performance tests over more than a year-period of continuous measurement are discussed.

2. Sample preparation and measurement setup

Conventional silica single-mode fiber (SMF-28e, G.652) with 8.3/125 μm core/cladding diameters was chosen as the source fiber for development of TOF sensor samples. We used the flame-heating technique and aimed for a reproducible output. Flame temperature T_f, hydrogen generator temperature T_{HG}, room humidity R_H and ambient temperature T_a were controlled during the tapering process, while initial T_{HG} was kept constant for each singular sample. Fluctuations were kept at $\triangle T_a < 0.1$ °C and $\triangle R_H < 0.1\%$.

For the purposes of the long-term analysis, we produced two TOF sample series with the waist length of 10 mm and with waist diameters w_D of 4.5 μm and 5.5 μm (over 25 TOF samples in both series). The waist diameter deviations were kept under 10% for both series, which was verified by a scanning-electron microscope. TOF samples were then stored in normal conditions i.e., $T_a = 22$–25 °C and $R_H = 35$–45%.

The measurement configuration is depicted in Fig. 1. An integrated distributed-feedback laser diode (LD) emitted at 1550 nm. LD signal was divided via a 3 dB coupler to two outputs and two TOF sensor samples were placed between the source and detectors in order to measure both TOF sensor samples simultaneously (in the same liquid analyte) and to both verify performance and exclude temperature discrepancies. Two InGaAs PIN photodiodes (DET) were incorporated altogether with LD into a single stabilized monitoring system to cover both instantaneous and continuous data-readout statistics. All FC/APC connectors were fixed. We have furthermore analyzed long-term
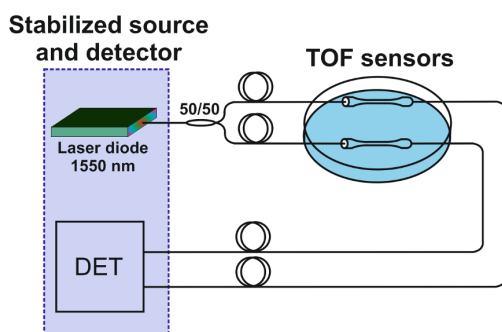
stability of the measurement configuration during a 3 weeks-long campaign and verified that our system is stable without any degradation. The measurement system dynamic range was limited to around 50 dB.

Laboratory testing of explosive or toxic liquids (e.g. hydrocarbons such as gasoline, toluene, or other toxic liquids as dioxane or chloroform) could be harmful to the health, so appropriate harmless liquid analytes were prepared to test our TOF samples. We substituted the above-mentioned hazardous liquids with environmentally friendly azeotropic mixtures of glycerol (GLY) dissolved in water to achieve refractive indices comparable to hydrocarbons or mixtures of hydrocarbons. Glycerol (1,2,3-Propanetriol) $C_3H_5(OH)_3$ represents a hygroscopic, colorless, viscous liquid (trihydric alcohol) which is neither explosive, flammable nor toxic, thereby suitable for such tests. The glycerol molecule is polar, therefore, it is unlimitedly miscible with H_2O. Mixtures of GLY with H_2O of defined concentrations were related via RI, which was measured at 632 nm (at 20 °C) and recalculated to RI at 1550 nm. Refractive index values at 1550 nm and 20 °C are for water 1.3180 and for glycerol 1.4594. Refractive indices of liquid analytes were continuously monitored with a digital refractometer. Refractive index of the GLY-H_2O mixture was then calculated as:

$$RI_{Mix,1550} = \frac{Con_{GLY}}{100} \cdot RI_{GLY,1550} + \frac{Con_{H20}}{100} \cdot RI_{H_20,1550}, \qquad (1)$$

where $RI_{Mix,1550}$ is the recalculated refractive index of the GLY-H_2O mixture at 1550 nm, Con_{GLY} and Con_{H2O} represent the percentage concentration of both liquids and finally $RI_{GLY,1550}$ and $RI_{H2O,1550}$ are the refractive indices of both liquids at 1550 nm.

3. TOF sensitivity-modification process

First, we measured a randomly selected TOF sample with $w_D = 5.20$ μm immediately after the production. The second measurement was carried out after 18 months (meanwhile the TOF sample was stored in standard room conditions). Before both measurements we perfectly purified the TOF sample using several isopropyl-alcohol (IPA) purification cycles to achieve a stable performance (especially after 18 months to remove all dust particles on the TOF surface).

The test was performed on three selected liquid analytes, IPA (RI = 1.374), Ethylene–glycol (EG, RI = 1.420) and their 50/50 mixture (RI = 1.397). Measurement results are summarized in Table 1. Note 13.6 dB higher attenuation when submerged in EG after 18 months (16.7 dB) with respect to the attenuation value just after production (3.1 dB). This attenuation increase is attributed to the surface structural modification of the TOF sample.

The origin of this phenomenon can be understood as a multi-step process. First, optical fibers are formed by extremely pure silica, thus no alkali ions are present, so leaching can be neglected. The starting conditions are defined by the tapering process carried out by the flame-heating technique using a hydrogen-based flame, which causes H^+ and OH^- ions to penetrate into the TOF where concentration decreases in relation to the distance from the TOF surface. Only a few ppm of H_2O content can result in the OH^- ion formation process, where such a low H_2O content is already present after fiber manufacturing [13].

Tapering of silica fibers is achieved by laterally stretching the fiber. The stretching assists in breaking molecular bonds by distorting the SiO_2 tetrahedral structure. Thus non-bridging oxygen atoms are formed,

Fig. 1. Measurement configuration for the analysis of TOF sensor sample performance in selected liquid analytes.; DET – two InGaAs PIN photodetectors.

Table 1
Attenuation of a TOF sample after production and after 18 months of exposition to ambient atmosphere, measured in three liquid analytes at 1550 nm.

Analyte RI	After production (dB)	After 18 months (dB)
1.374	0.4	6.0
1.397	1.1	10.2
1.420	3.1	16.7

bound by one covalent bond to the glass network and holding one negative charge to compensate for the positive ions nearby [14]. The fiber is then less resistant to humidity effects [15].

These effects contribute to the modification of the TOF surface layer, with regard to hydrogen-bonding processes, resulting in a sol–gel layer formation. Note, that this sol–gel layer is formed from the fiber itself, due to the material change in the fiber surface layer, which is completely different from the well-known methods of sol–gel and other functional layer deposition on the fiber surface [9,16].

In the first step, a layer similar to a sol–gel is formed and gradually grows in thickness (in direction towards the TOF core) until equilibrium state is achieved, when TOF is exposed to a humid atmosphere, or submerged into an analyte (presuming the liquid analyte contains water or is able to form OH^- ions). Typically, the sol–gel layer thickness is in the order of nanometers. The sol–gel layer's physical properties differ from the pure silica glass material, in particular refractive index is lower [17]. Typically sensor sensitivity is expected to decrease when considering a modified layer on the TOF surface with a lower RI. This assumption is valid until the TOF is dried. Once the TOF is removed from the analyte (or placed in a lower humidity atmosphere), the sol–gel layer dries and micro-cracks develop [12].

The utilization of GLY and EG as liquid analytes further magnifies the effect of sol–gel layer formation as these liquids are highly hygroscopic. In addition, when IPA is used to purify the fibers, it can help even more to increase micro-crack formation. This is based on the fact that IPA (as a 96% alcohol) efficiently binds water, thus drawing the OH^- ions from the sol–gel layer. The effect of submerging/drying was observed for multiple TOF samples resulting in a high increase of attenuation, thus also in TOF sensor sensitivity enhancement and response curve shift, as will be described in the next chapter.

4. Measurement of TOF sensor response based on structural modification

We investigated the TOF sensor response and possibility of sensitivity enhancement on two randomly selected TOF sensor samples, with $w_D = 4.80\,\mu m$ and $w_D = 5.50\,\mu m$, denoted as Samples A and B, respectively. Sample A was purified immediately after the production without any contact with GLY. Sample B was submerged into GLY immediately after the production, then purified and stored. After 12 months both TOF sensor samples were measured for the first time (such samples are hereafter marked by index 1, i.e., A_1, B_1). Both TOF sensor samples were then purified and stored in the same conditions for additional 6 months, resulting in a total of 18 months prior to the second measurement (indexed as A_2, B_2).

A GLY-H_2O solution was prepared for the measurement. The starting point was set to the RI of 1.435 and the solution was diluted, step-by-step in 19 measurement points, down to the RI of 1.360. For each of these points, refractive index of the mixture was analyzed by the refractometer. Increase in attenuation and thus sensitivity was observed for both TOF sensor samples submerged in the same liquid analytes after 18 months in contrast to the results after 12 months, as presented in Fig. 2.

To provide a comparison of studied TOF sensor samples, sensitivity S was introduced which can be expressed as the ratio of optical intensity difference $\triangle I$ to refractive index difference $\triangle n$ as:

$$S = \frac{\triangle I}{\triangle n} \tag{2}$$

Sensitivity enhancements of up to 1300 dB/RIU and 1400 dB/RIU were reached for Sample A and Sample B, respectively, for a liquid analyte RI of 1.415, when comparing results after 12 and 18 months. The achieved maximum sensitivity values after 18 months of exposure were $S = 1920\,dB/RIU$ and $S = 2100\,dB/RIU$ for Samples A and B, respectively. This is a significant sensitivity enhancement compared to previous results [18], where the studied TOFs were not sensitivity-
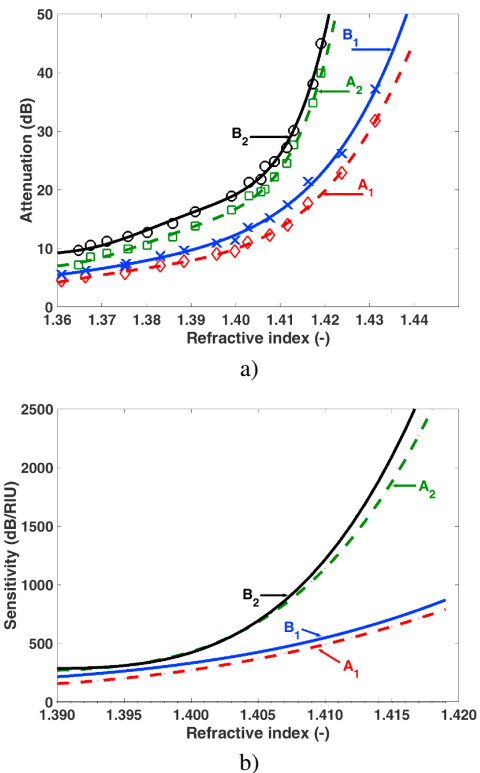

Fig. 2. Measured a) attenuation and b) sensitivity dependences on the liquid analyte RI at 1550 nm, Sample A and Sample B after 12 months of exposure (A_1, B_1) and 18 months of exposure (A_2, B_2).

enhanced.

Please note an interesting point of the TOF surface structural modification: Sample B, with wider w_D, provided greater sensitivity than Sample A (e.g. compare at RI of 1.415 in Fig. 2b). This is in contrast to the general taper theory which states that a thinner TOF should have a larger evanescent-wave overlap and, thus, greater sensitivity. The enhanced sensitivity in the case of Sample B is attributed to the TOF surface structural modification caused by the submersion of the TOF sample into GLY 12 months prior to the first measurement (right after the production).

5. Long-term measurement

Having achieved enhanced sensitivity, we further evaluated the performance of the structurally-modified TOF sensor samples in comparison to freshly-produced TOF sensor samples. Long-term stability of TOFs was studied in terms of sensitivity and resolution. Two selected TOF sensor samples were chosen, both with the identical $w_D = 5.40\,\mu m$, to exclude the effect of waist diameter. First TOF sensor (Sample C) was picked from a freshly manufactured TOF set and was encapsulated in a protective metallic cover as depicted in Fig. 3. Sample D was structurally-modified (i.e. having an enhanced sensitivity) as described in the previous section. Both TOF sensor samples were purified before the test. Afterwards, continuous measurement was carried out for more than 12 months in total.

As the liquid analyte we used again the GLY-H_2O mixture where for the starting point the analyte was diluted to RI of 1.400 and, via water evaporation, the RI of the analyte continuously increased. Once RI of 1.440 was reached (after several weeks), we added H_2O and set RI again to 1.400 to start a new measurement cycle. The measurement
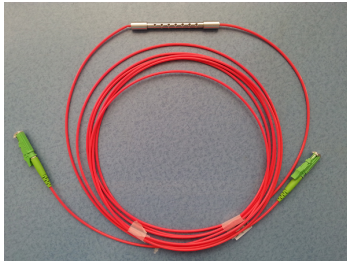
M. Komanec et al.

Fig. 3. TOF sensor sample encapsulation in protective metallic tubing, which allows liquid through-flow, equipped with E2000 connectors for easy inclusion in any optical system.

procedure was always the same step-wise process – first we measured actual attenuation of the submerged sensor, then we took a sample of the liquid analyte and measured its refractive index by a refractometer (which was then recalculated to 1550 nm and plotted with regard to attenuation/normalized power).

Calibration was performed for both TOF sensor samples during the first two measurement cycles, representing a relation between measured optical power (attenuation) and corresponding RI of liquid analyte. It is common that for real sensor application, the operation in the sensors' linear regime is desired. Sample C provided linear calibration in the RI region of interest (1.400–1.425). However, Sample D required a two-part linear calibration, where at liquid analyte RI range of 1.400–1.416 we can observe a significant increase of the calibration line steepness (denoted as "linear fit steep"). In the RI range of 1.416–1.425 we observe almost a flat response (denoted as "linear fit slow") for Sample D. Calibration lines with all measured data (over all cycles) are plotted in Fig. 4.

We see a clear trend of the structurally-modified TOF sensor sample, where the linear regime (steep) shifts to lower liquid analyte RIs (below 1.417) and is accompanied by enhanced sensitivity (derivation of the slope). Using the calibration (presented in Fig. 4) we were able to determine the TOF sensor long-term stability in over 12 months of continuous measurement. Sample C showed a standard deviation in measured RI of $6.6 \cdot 10^{-4}$ and drift of the working point (mean value) of only $1.3 \cdot 10^{-4}$. Sample D provided a standard deviation in measured RI of $12 \cdot 10^{-4}$ and drift of the working point of $15 \cdot 10^{-4}$.

To exactly compare both TOF sensor samples, we calculated their resolutions over all acquired data with regard to their calibration. Resolution (R) was calculated as:
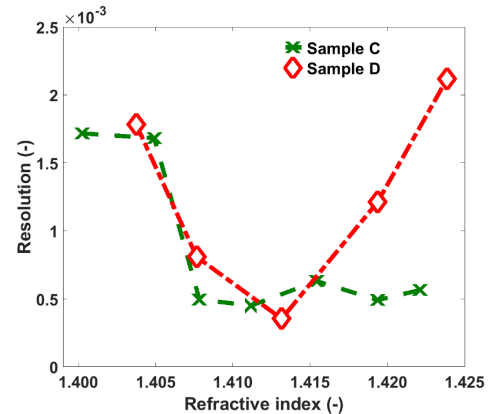
Fig. 5. Resolution of Sample C and Sample D with regard to the refractive index of the liquid analyte.

$$R = \frac{\triangle n}{\triangle I/\sigma_I}, \tag{3}$$

where σ_I stands for the standard deviation of the measured optical power with regard to the calibration.

Fig. 5 presents resolution dependence on the refractive index of the liquid analyte for Sample C and Sample D. For Sample C values around $5 \cdot 10^{-4}$ are experienced in the RI range above 1.405, Sample D has comparable values only in the RI range of 1.406–1.416. On the other hand sensitivity Sample C is 218 dB/RIU compared to Sample D with enhanced sensitivity of 883 dB/RIU for a liquid analyte with RI = 1.415.

6. Conclusion

TOF surface structural modification has been presented and discussed with regards to the detection of liquids. We determined a permanent TOF response curve shift and sensitivity enhancement caused by sol–gel development in the TOF inner surface layer. The structural modification was magnified by repeatedly submerging the TOF sensor sample into hygroscopic liquids (Ethylene–glycol or Glycerol) and then by subsequent drying in Isopropyl-alcohol.

We experimentally verified the sensitivity enhancement with an increase up to 1400 dB/RIU for a liquid analyte with a refractive index of 1.415 for the structurally-modified TOF sensor samples. We thus achieved an overall sensitivity of more than 2100 dB/RIU, which is almost ten times higher than for a freshly produced TOF having a sensitivity around 220 dB/RIU.

For the long-term continuous measurement of over 12 months, selected TOF sensor samples with linear calibration were evaluated. Experimental tests demonstrated high performance stability of a structurally-unmodified TOF sensor sample with an RI standard deviation of $6.6 \cdot 10^{-4}$ and working point drift below $2 \cdot 10^{-4}$. A structurally-modified TOF sensor sample provided significantly higher sensitivity. Working point drift was $15 \cdot 10^{-4}$.

Our results in TOF structural modification show that we can tailor the linear regime of the TOF sensor response curve to a desired RI range. Enhanced sensitivity can be achieved for a particular range of refractive indices. Measurements with duration of less than one month can expect stability of the sensitivity-enhanced TOF sensors in the order of 10^{-4}.
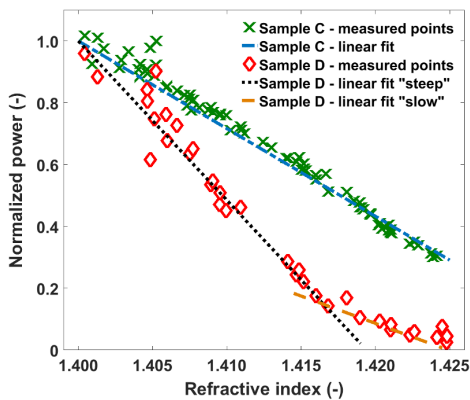

Fig. 4. All measured data points over more than 12 months and linear fits based on the first two measurement cycles further used as calibrations of Sample C (without structural modification) and Sample D (structurally-modified).

Acknowledgements

References

[1] N. Chen, T. Yang, Z. Feng, Y. Chen, C. Lin, Cellular-Dimension Picoliter-Volume Index Microsensing Using Micro-Abrupt-Tapered Fiber Mach-Zehnder Interferometers, IEEE Photonics Technol. Lett. 24 (10) (2012) 842–844.

[2] P. Wang, G. Brambilla, M. Ding, T. Lee, L. Bo, Y. Semenova, Q. Wu, G. Farrell, Enhanced refractometer based on periodically tapered small core singlemode fiber, IEEE Sens. J. 13 (1) (2013) 180–185.

[3] H. Yu, L. Xiong, Z. Chen, Q. Li, X. Yi, Y. Ding, F. Wang, H. Lv, Y. Ding, Solution concentration and refractive index sensing based on polymer microfiber knot resonator, Appl. Phys. Exp. 7 (2) (2014) 022501 .

[4] F. Shi, J. Wang, Y. Zhang, Y. Xia, L. Zhao, Refractive index sensor based on s-tapered photonic crystal fiber, IEEE Photonics Technol. Lett. 25 (4) (2013) 344–347.

[5] C.R. Biazoli, S. Silva, M.A.R. Franco, O. Frazao, C.M.B. Cordeiro, Multimode interference tapered fiber refractive index sensors, Appl. Opt. 51 (24) (2012) 5941–5945.

[6] Y.-C. Kim, W. Peng, S. Banerji, K.S. Booksh, Tapered fiber optic surface plasmon resonance sensor for analyses of vapor and liquid phases, Opt. Lett. 30 (17) (2005) 2218–2220.

[7] Y.-H. Tai, P.-K. Wei, Sensitive liquid refractive index sensors using tapered optical fiber tips, Opt. Lett. 35 (7) (2010) 944–946.

[8] J. Homola, S.S. Yee, G. Gauglitz, Surface plasmon resonance sensors: review, Sens. Actuat. B: Chem. 54 (1) (1999) 3–15.

[9] Z. Qiang, L. Junyang, Y. Yanling, G. Libo, X. Chenyang, Micro double tapered optical fiber sensors based on the evanescent field-effect and surface modification, Optik 125 (17) (2014) 4614–4617.

[10] T. Nemecek, M. Komanec, T. Martan, R. Ahmad, S. Zvanovec, Suspended-core microstructured fiber for refractometric detection of liquids, Appl. Opt. 54 (30) (2015) 8899–8903.

[11] M. Fujiwara, K. Toubaru, S. Takeuchi, Optical transmittance degradation in tapered fibers, Opt. Express 19 (9) (2011) 8596–8601.

[12] S.-M. Chuo, L.A. Wang, Propagation loss, degradation and protective coating of long drawn microfibers, Opt. Commun. 284 (12) (2011) 2825–2828.

[13] M. Tomozawa, D.-L. Kim, V. Lou, Preparation of high purity, low water content fused silica glass, J. Non-Cryst. Solids 296 (1) (2001) 102–106.

[14] W. Wang, P. Lu, L. Han, C. Zhang, L. Wu, P. Guan, R. Su, J. Chen, Structural and electronic properties of peroxy linkage defect and its interconversion in fused silica, J. Non-Cryst. Solids 434 (2016) 96–101.

[15] N. Gougeon, M. Poulain, R.E. Abdi, Evolution of strength silica optical fibers under various moisture conditions, Opt. Mater. 27 (1) (2004) 75–79.

[16] D. Liu, W. Han, A.K. Mallik, J. Yuan, C. Yu, G. Farrell, Y. Semenova, Q. Wu, High sensitivity sol-gel silica coated optical fiber sensor for detection of ammonia in water, Opt. Express 24 (21) (2016) 24179–24187.

[17] Y. Tamar, M. Tzabari, C. Haspel, Y. Sasson, Estimation of the porosity and refractive index of sol-gel silica films using high resolution electron microscopy, Sol. Energy Mater. Sol. Cells 130 (2014) 246–256.

[18] T. Martan, T. Nemecek, M. Komanec, R. Ahmad, S. Zvanovec, Refractometric detection of liquids using tapered optical fiber and suspended core microstructured fiber: a comparison of methods, Appl. Opt. 56 (9) (2017) 2388–2396.

4.4   Suspended-core microstructured fiber for the refractometric detection of liquids

This chapter is a version of the published manuscript:

[J4]: T. Nemecek, M. Komanec, T. Martan, R. Ahmad, and S. Zvanovec, "Suspended-core microstructured fiber for refractometric detection of liquids", APPLIED OPTICS, vol. 54, no. 30, pp. 8899-8903, 2015.

Relevance to my Ph.D. thesis:

Up to the point of writing, all of the above-mentioned methods have their limitations, thus I decided to develop a new approach to combine high sensitivity, robustness, as well as facilitate the sensing system implementation. To fulfill these demands, an SC-MOF filled by a liquid analyte was chosen, for the first time, as a modifiable tool for the refractometric sensing of liquid analytes. SC-MOFs allow the detection of a broad range of liquid analytes by modifying the SC-MOF inner structure, thus reaching the required sensitivity. Extremely small amounts of liquid analyte in order of nanoliters are required compared to other detection methods, such as TOF sensors, which supports the possibility of this method being applied e. g., in medical or biological areas. SC-MOF filling processes have been examined, and, subsequently, a liquid-filled SC-MOF structure has been evaluated as a sensor of liquid analytes. Supreme resolution and sensitivity were reached in comparison to other methods, establishing this method as a promising approach.

appliedoptics

Suspended-core microstructured fiber for refractometric detection of liquids

Tomas Nemecek,* Matej Komanec, Tomas Martan, Redwan Ahmad, and Stanislav Zvanovec

Department of Electromagnetic Field, Faculty of Electrical Engineering, Czech Technical University in Prague, Technicka 2,
166 27 Prague 6, Czech Republic
*Corresponding author: nemect10@fel.cvut.cz

A silica suspended-core microstructured optical fiber sensor for detection of liquids, operating at 1550 nm, is analyzed. The sensing principle is based on the evanescent wave overlap into a tested analyte, which is filled via capillary forces into the cladding holes. Validations for analytes in the refractive index range of 1.35–1.43 are carried out with liquid-analyte-filling-length limits being studied both theoretically and experimentally. We prove, for the first time to our knowledge, that an extreme sensitivity of 342.86 dB/RIU and resolution of 4.4×10^{-5} can be achieved. This sensor represents a high-quality alternative for applications requiring a facile, low-cost solution.   © 2015 Optical Society of America

OCIS codes: (280.4788) Optical sensing and sensors; (060.2370) Fiber optics sensors; (060.4005) Microstructured fibers.

1. INTRODUCTION

Suspended-core microstructured optical fibers (SC-MOFs) were first presented in 2001 by Monro *et al.* [1] and have been studied and enhanced, achieving core sizes below 1 μm [2] utilizing various glass compositions [3,4] and developing inner surface functionalization [5,6]. SC-MOFs outperform conventional MOFs in terms of significantly increased nonlinearity, leading to extreme broadband supercontinuum generation [4] and enhanced evanescent wave overlap which substantially increases when cladding holes are filled with gases or liquids, making these fibers suitable for sensing purposes [7,8].

Optical sensors based on SC-MOFs have, therefore, attracted great attention due to their applications in hazardous environments for liquid-level [9] monitoring and biological DNA analysis [6]. For these applications the operating principle is, in some cases, based not only on refractometry, but is further evolved to fluorescence [6] or Raman spectroscopy [9]. To achieve enhanced sensitivities and resolution, a theoretical study has been carried out for SC-MOFs with core diameters below 1 μm [8] when considering glass materials. Exposed-core SC-MOFs for liquid filling were presented in [10], while other means were proposed in [11].

Significant sensitivity enhancements were achieved by SC-MOF surface functionalization [6], which demands precise deposition steps of the sensing layer, and by core diameter reduction [8], leading to coupling efficiency issues and waveguide losses. For widespread SC-MOF sensor applications, e.g., in petrochemistry and the automotive industry and for chemical analysis purposes, an easy sensing technique is required. Attenuation-based SC-MOF sensors provide a considerably less complicated solution than, e.g., functionalized-surface [6] or exposed-core [8] SC-MOF fluorescence-based sensors. Moreover attenuation-based SC-MOFs have never been studied in greater detail. This approach was only briefly considered with simulations carried out in [12] as an example of the theoretical limit of the utilized method.

In this paper, we present an attenuation-based SC-MOF liquid sensor analysis for the refractive index (RI) range of 1.35–1.43. Our sensor exploits the refractometric effect based on the enhanced evanescent wave overlap in the SC-MOF cladding holes filled with a tested analyte.

With a selected sensor and optimized measurement method, we achieved extreme sensitivity and resolution without the need for any additional fiber surface functionalization or SC-MOF core diameter reduction. The results provide substantial experimental knowledge in the respective fields of SC-MOF liquid sensors and MOF sensing.

2. EXPERIMENTAL BACKGROUND

The measurement setup is depicted in Fig. 1. A laser source with a wavelength of 1550 nm and output power of 10 mW irradiates polarized light. The laser beam is expanded by a graded-index (GRIN) collimator to 0.5 mm full width at half-maximum (FWHM) and, subsequently, collimated by a 40× objective (NA = 0.65) to the core of the SC-MOF.
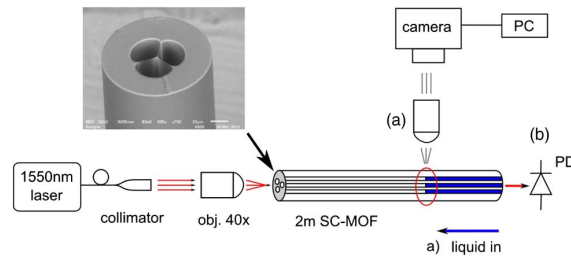
Fig. 1. Measurement setup of the SC-MOF liquid sensor. PD, photodetector; PC, microscope image processing. (a) Step one: filling the liquid analyte into the SC-MOF cladding holes. (b) Step two: attenuation measurement of the analyte-filled SC-MOF. Inset shows the SC-MOF cleave detail.

2 μm 3D stages are utilized to adjust the collimation assembly precisely. Coupling efficiency of over 10% is achieved with this setup. The total length of SC-MOF is 2 m. The analyte-filling length in SC-MOF is visualized and measured by microscope (see Figs. 1 and 4, respectively). Subsequently, an integral photodetector (PD) is used to measure attenuation at the cleaved end of the SC-MOF (filled with analyte).

The employed SC-MOF is composed of undoped silica with a core diameter of 2.75 μm, bridge width of 270 nm, and outer diameter of 122 μm. The radial diameters of the three cladding holes are all 29.73 μm. Material attenuation of an air-filled SC-MOF is 1 dB/m. The SC-MOF cross-section is depicted in Fig. 2(a) with detail of the SC-MOF core shown in Fig. 2(b).

To perform SC-MOF sensitivity analysis, seven liquid analytes are prepared, ranging from 1.3520–1.4269 RI with a continuous step of approximately 0.01 RI. Table 1 summarizes the prepared analytes with their RIs at 1550 nm, and these values are verified by an Abbe refractometer at 632 nm (recalculated to 1550 nm, employing refractive-index equations for each particular analyte).

Light coupled into the SC-MOF core is strongly guided thanks to the silica–air RI difference, and there is minimal evanescent wave overlap in the cladding holes. As the cladding holes are filled with analytes, the RI difference decreases and the evanescent wave overlap is enhanced, which is analyzed using COMSOL software for our specific SC-MOF (results depicted in Fig. 3).

The viscosity of selected analytes makes it possible to use capillary forces for filling. The main advantage of this technique
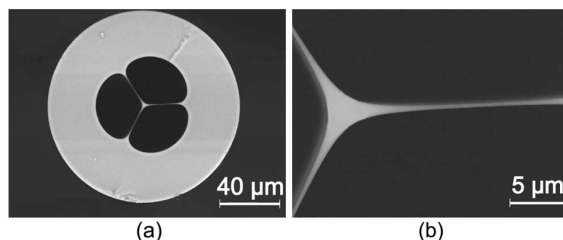
Table 1.   Refractive Indices of Utilized Analytes at 1550 nm

Analyte	Denomination	RI
Ethyl alcohol	ETOH	1.3520
Isopropyl alcohol	IPA	1.3738
75% IPA + 25% EG	IPA75EG	1.3861
50% IPA + 50% EG	IPA50EG	1.3970
25% IPA + 75% EG	IPA25EG	1.4086
Ethylene glycol	EG	1.4204
76% Glycerol + 24% H20	GLY76H2O	1.4269

is that only a small amount of analyte, specifically 27.8 nL/cm (one cladding hole area is 925 μm^2), is required.

Filling length limit is set by the analyte properties in our experiment, whereas the whole measurement setup limit is set by the dynamic range, in our case to 45 dB. The maximum filling length F for the SC-MOF can be calculated as

$$F = 2\sigma \cos(\alpha)/\rho rg, \qquad (1)$$

where σ represents surface tension, α is the contact angle, ρ is the analyte density, g is acceleration due to gravity, and r is the capillary radius, where we assume a capillary approximation for our SC-MOF cladding holes.

The determined maximum filling length for ethyl alcohol (ETOH) and isopropyl alcohol (IPA) is over 26 cm. For ethylene glycol (EG) and glycerol-water (GLY76H2O), it is possible to fill over 39 cm (the contact angle for both analytes is over 23°, but liquid densities and surface tensions are 1110 kg/m^3 and 48 mN/m for EG and 1290 kg/m^3 and 62.5 mN/m for glycerol).

The measurement setup is referenced with the air-filled SC-MOF for all subsequent measurements (one analyte, all filling lengths). Then SC-MOF is continuously filled with a particular analyte up to 25 mm in length, with a step lower than 5 mm. The filling length is monitored by microscopic side-viewing as shown in Fig. 4, guaranteeing a precise analyte filling length within 0.5 mm. For each filling step, the transmitted power is measured at the photodetector. Each analyte measurement is repeated at least three times to avoid inaccuracies.

Fig. 2. SC-MOF scanning electron microscope photographs. (a) SC-MOF cross-section. (b) Detail of the SC-MOF core.
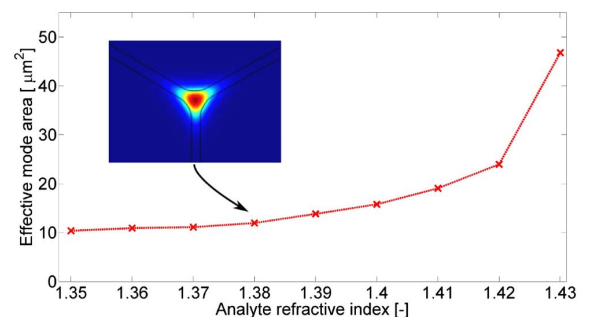

Fig. 3. Simulation of the effective mode area. Inset shows the effective mode area visualization of SC-MOF filled with an analyte of RI = 1.38.
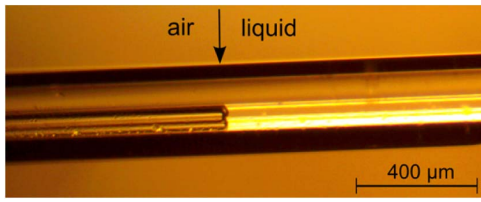
Fig. 4. Microscopic side view of SC-MOF filled with a liquid analyte. Arrow shows the air–analyte boundary.

3. EXPERIMENTAL RESULTS

The measurement results presented in Fig. 5 show loss with respect to the filling length F for each prepared liquid analyte, whereas Fig. 6 depicts attenuation dependence on analyte RI. Figures 5 and 6 show increasing sensitivity with increasing analyte RI and filling length, which is in accordance with the simulation results.

Analytes such as GLY76H20 and EG, where the analyte RI is close to the SC-MOF material RI (1.4454 at 1550 nm), show a significant increase in measured sensitivity with respect to filling length—in particular for GLY76H2O, where the first 5 mm filling step causes almost 20 dB loss though, for filling lengths longer than 6 mm, the slope of the loss curve decreases considerably. A similar effect is observed for EG, where loss increases more rapidly at the beginning. These phenomena are
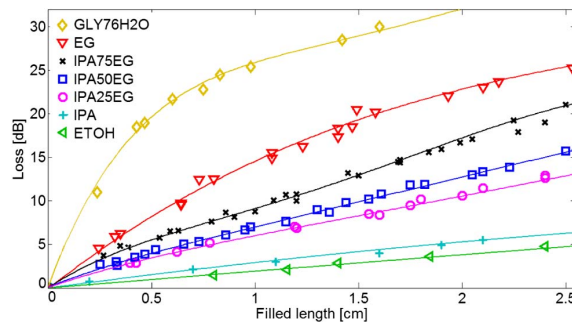

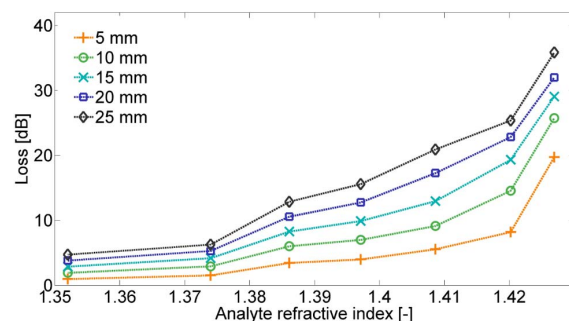**Fig. 5.** Measured attenuation of SC-MOF dependent upon analyte filling length for all tested analytes.

Fig. 6. Measured attenuation of SC-MOF dependent upon refractive index for selected filling lengths.
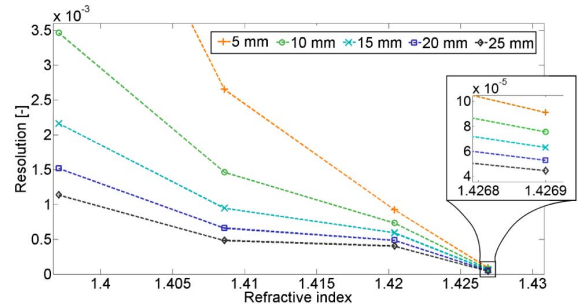

Fig. 7. Resolution of SC-MOF sensor dependent upon analyte refractive index for selected filling length. Inset shows a detail of the resolution values for GLY76H2O.

in contrast to other tested analytes, where trends are observed in near-linear fashion.

The SC-MOF sensor resolution R is calculated as [13]

$$R = \frac{\Delta n}{\Delta I / m_n},\qquad(2)$$

where Δn represents the RI difference between the two closest analytes, ΔI is the intensity difference, and m_n is measurement noise. The results are summarized in Fig. 7.

Our SC-MOF sensor reaches a resolution of 4.4×10^{-5} at RI of 1.4269 for filling length of 25 mm. The longer the filling length, the higher the resolution; therefore, resolution can be modified for sensing purposes, e.g., for a specific RI range. Longer filling lengths imply higher resolution, especially for analytes with 1.35–1.41 RI, where maximum filling lengths are limited by Eq. (1), not by the measurement setup dynamic range.

Sensitivity S is also enumerated for our SC-MOF sensor as [14]

$$S = \frac{\Delta I}{\Delta n},\qquad(3)$$

where Δn represents the RI difference between the two closest analytes; ΔI then stands for intensity difference. A maximal sensitivity of 324.86 dB/RIU (1341.61 μW/RIU), for filling length 25 mm at RI of 1.4269, has been achieved. For RI 1.43–1.44, sensitivity is predicted to increase as the dynamic range poses the limit.

A comparison to published results is provided in Table 2. So far, published results are based on several different methods of RI measurement: a RI fiber sensor based on a tilted fiber Bragg grating (FBG) interacting with multimode fiber [15], a RI sensor which consists of a combination of an intermodal photonic crystal fiber interferometer as a sensing head and FBG as a demodulating element [14], a sensing architecture consisting of a two-core chirped MOF [12], a sensor based on multimode interference (MMI) in the multimode fiber core section sandwiched between two single-mode fibers [16], a sensor based on MMI in the fiber tip [17], a laser-micromachined Fabry–Perot optical fiber tip sensor [18], a sensor based on Fresnel reflection modulated by Fabry–Perot interference [19], and an all-silica miniature dual-parameter fiber-optic Fabry–Perot sensors [20,21].

Table 2.   Comparison of our Results from SC-MOF Liquid Sensor with State-of-Art Liquid Sensor References

References	RI	Sensitivity	Resolution (RIU)
[15]	1.37–1.43	28.5 µW/RIU	–
[14]	1.36–1.39	679 µW/RIU	1.5×10^{-5}
[12]	1.42	300/RIU	3×10^{-6}
[16]	1.38–1.45	300.4 dB/RIU	3.3×10^{-5}
[17]	1.33–1.38	110 dB/RIU	2.2×10^{-4}
[18]	1.33–1.441	27 dB/RI	3.7×10^{-5}
[19]	1.314–1.365	205 dB/RI	5×10^{-6}
[20][a]	1.38–1.45	1027 nm/RIU	$\sim 10^{-7}$
[21][a]	1.320–1.325	830 nm/RIU	2×10^{-5}
Our SC-MOF sensor			
	1.4269	1341.61 µW/RIU	4.4×10^{-5}
	1.4269	342.86 dB/RIU	4.4×10^{-5}

[a]Wavelength-shift based sensors.

In comparison with [17], without considering RI ranges, our maximal resolution is one order better and we also provide higher sensitivity. With similar RI range, Wang and Farrell [16] achieved comparable resolutions to our SC-MOF sensor. Slightly better resolution is provided by [14] and one order better resolution was presented in [12], but with a significantly more demanding sensor fabrication process and a complex measurement configuration. The best resolution is provided by the wavelength-shift-based sensor [20] for the major segment of the RI range; on the other hand, this approach employs spectral analysis.

The sensitivity achieved is a significant improvement over previously published results [14,16], in particular 47× higher sensitivity than [15] and 3× higher than [17] if we compare only the same RI ranges. This shows the remarkable sensing potential of SC-MOF and the possibility of further applications when detecting various analytes.

To acquire sufficient sensitivity and resolution for high-RI (≥ 1.42) analytes such as EG and GLY76H20, the optimal filling length is from 0.5 to 10 mm. For lower-RI (1.35–1.41) analytes, including IPA/EG mixtures and ETOH, it is desirable to increase the filling length as much as possible with respect to the dynamic range of the utilized measurement setup. We have presented experimental results of a liquid-filled SC-MOF sensor. Additionally, simulations of effective mode area evolution with respect to analyte RI were carried out.

4. CONCLUSION

We have analyzed the filling effects of analytes of various RIs and viscosities. The theoretical filling length limits the experimental measurement only when total loss for a particular analyte at the limit length is lower than the dynamic range of the whole measurement setup. This filling-length-limiting effect may occur for analytes in the RI range of 1.35–1.38.

Our measurement method with the SC-MOF sensor precisely distinguishes all tested analytes and has the potential to be used over a wide range of analyte refractive indices. Shorter filling lengths are suitable for measurements of high-RI analytes (EG, GLY76H2O) where the dynamic range could pose a limitation. Liquid analytes with RI less than 1.41 provide linear

dependences of sensitivity curves, which is highly desired for real sensor applications.

REFERENCES

1. T. M. Monro, W. Belardi, K. Furusawa, J. C. Baggett, N. G. R. Broderick, and D. J. Richardson, "Sensing with microstructured optical fibers," Meas. Sci. Technol. **12**, 854–858 (2001).
2. H. Ebendorff-Heidepriem, S. C. Warren-Smith, and T. M. Monro, "Suspended nanowires: fabrication, design and characterization of fibers with nanoscale cores," Opt. Express **17**, 2646–2657 (2009).
3. X. Feng, F. Poletti, A. Camerlingo, F. Parmigiani, P. Petropoulos, P. Horak, G. M. Ponzo, M. Petrovich, J. D. Shi, W. H. Loh, and D. J. Richardson, "Dispersion controlled highly nonlinear fibers for all optical processing at telecoms wavelengths," Opt. Fiber Technol. **16**, 378–391 (2010).
4. U. Møller, Y. Yu, C. Petersen, X. Gai, L. Brilland, D. Mechin, C. Caillaud, J. Troles, B. Luther-Davies, and O. Bang, "Multi-milliwatt mid-infrared supercontinuum generation in a suspended core chalcogenide fiber," Opt. Express **23**, 3282–3291 (2015).
5. A. Csaki, F. Jahn, I. Latka, T. Henkel, D. Malsch, T. Schneider, K. Schröder, K. Schuster, A. Schwuchow, R. Spittel, D. Zopf, and W. Fritzsche, "Nanoparticle layer deposition for plasmonic tuning of microstructured optical fibers," Small **6**, 2584–2589 (2010).
6. E. Coscelli, M. Sozzi, F. Poli, D. Passaro, A. Cucinotta, S. Selleri, R. Corradini, and R. Marchelli, "Toward a highly specific DNA Biosensor: PNA-modified suspended-core photonic crystal fibers," IEEE J. Sel. Top. Quantum Electron. **16**, 967–972 (2010).
7. A. S. Webb, F. Poletti, D. J. Richardson, and J. K. Sahu, "Suspended-core holey fiber for evanescent-field sensing," Opt. Eng. **46**, 010503 (2007).
8. S. C. Warren-Smith, S. V. Afshar, and T. M. Monro, "Theoretical study of liquid-immersed exposed-core microstructured optical fibers for sensing," Opt. Express **16**, 9034–9045 (2008).
9. G. Tsiminis, F. Chu, S. C. Warren-Smith, N. A. Spooner, and T. M. Monro, "Identification and quantification of explosives in nanolitre solution volumes by Raman spectroscopy in suspended core optical fibers," Sensors **13**, 13163–13177 (2013).
10. S. Warren-Smith, H. Ebendorff-Heidepriem, T. Foo, R. Moore, C. Davis, and T. Monro, "Exposed-core microstructured optical fibers for real-time fluorescence sensing," Opt. Express **17**, 18533–18542 (2009).
11. C. M. B. Cordeiro, C. J. S. de Matos, E. M. dos Santos, A. Bozolan, J. S. K. Ong, T. Facincani, G. Chesini, A. R. Vaz, and C. H. B. Cruz, "Liquid-core, liquid-cladding photonic crystal fibers," Meas. Sci. Technol. **15**, 11207–11212 (2007).
12. P. Torres, E. Reyes-Vera, A. Díez, and M. V. Andrés, "Two-core transversally chirped microstructured optical fiber refractive index sensor," Opt. Lett. **39**, 1593–1596 (2014).
13. N. Díaz-Herrera, D. Viegas, P. A. S. Jorge, F. M. Araújo, J.-L. Santos, M.-C. Navarrete, and A. González-Cano, "Fibre-optic SPR sensor with a FBG interrogation scheme for readout enhancement," Sens. Actuators B **144**, 226–231 (2010).
14. W. Qian, C. C. Chan, C. L. Zhao, Y. Liu, T. Li, L. Hu, K. Ni, and X. Dong, "Photon. crystal fiber refractive index sensor based on a fiber Bragg grating demodulation," Sens. Actuators B **166**, 761–765 (2012).
15. Y. Jin, X. Dong, H. Dong, and C. Shen, "Refractive-index sensor based on tilted fiber Bragg grating interacting with multimode fiber," Microwave Opt. Technol. Lett. **52**, 1375–1377 (2010).
16. Q. Wang and G. Farrell, "All-fiber multimode-interference-based refractometer sensor: proposal and design," Opt. Lett. **31**, 317–319 (2006).
17. S. F. Silva, O. Frazão, J. L. Santos, and F. X. Malcata, "A reflective optical fiber refractometer based on multimode interference," Sens. Actuators B **161**, 88–92 (2012).
18. Z. Ran, Y. Rao, W. Liu, X. Liao, and K. Chiang, "Laser-micromachined Fabry–Perot optical fiber tip sensor for high-resolution temperature-

independent measurement of refractive index," Opt. Express **16**, 2252–2263 (2008).

19. J.-R. Zhao, X.-G. Huang, W.-X. He, and J.-H. Chen, "High-resolution and temperature-insensitive fiber optic refractive index sensor based on Fresnel reflection modulated by Fabry–Perot interference," J. Lightwave Technol. **28**, 2799–2803 (2010).

20. S. Pevec and D. Donlagic, "High resolution, all-fiber, micro-machined sensor for simultaneous measurement of refractive index and temperature," Opt. Express **22**, 16241–16253 (2014).

21. S. Pevec and D. Donlagic, "Miniature fiber-optic sensor for simultaneous measurement of pressure and refractive index," Opt. Lett. **39**, 6221–6224 (2014).

4.5   Fiber-optic refractometric sensors using a semi-ellipsoidal sensing element

This chapter is a version of the published manuscript:

[J5]: A. N. Castro Martinez, M. Komanec, T. Nemecek, S. Zvanovec, and S. Khotiaintsev, "Fiber optic refractometric sensors using a semi-ellipsoidal sensing element", APPLIED OPTICS, vol. 55, no. 10, pp. 2574-2579, 2016.

Relevance to my Ph.D. thesis:

SC-MOF and TOF sensors are compared to a newly developed form of semi-ellipsoidal sensing element. The main advantage of the semi-ellipsoidal sensor lies in its simplicity, combined with its reasonable sensitivity to the external RI and its capability of covering a broad measuring range between 1.00 and 1.47 RI only by varying the position of the input optical fiber. The comparison with two of our other sensors (TOF and SC-MOF) is presented. The sensing region, featuring a semi-ellipsoidal element reaches a wide RI range, however, SC-MOF and TOF sensors provide higher sensitivity, especially close to the refractive index of silica.

appliedoptics

Fiber optic refractometric sensors using a semi-ellipsoidal sensing element

Amalia Nallely Castro Martinez,[1,*] Matej Komanec,[2] Tomas Nemecek,[2] Stanislav Zvanovec,[2] and Sergei Khotiaintsev[1]

[1]*Faculty of Engineering, Universidad Nacional Autónoma de México, Circuito Escolar sn, Ciudad Universitaria, D.F. 04510, Mexico*
[2]*Department of Electromagnetic Field, Faculty of Electrical Engineering, Czech Technical University in Prague, Technicka 2, 166 27 Prague 6, Czech Republic*
Corresponding author: ancm_0186@comunidad.unam.mx

We present theoretical and experimental results for a fiber optic refractometric sensor employing a semi-ellipsoidal sensing element made of polymethyl methacrylate. The double internal reflection of light inside the element provides sensitivity to the refractive index of the external analyte. We demonstrate that the developed sensor, operating at a wavelength of 632 nm, is capable of measurement within a wide range of refractive indices from $n = 1.00$ to $n = 1.47$ with sensitivity over 500 dB/RIU. A comparison of the developed sensor with two more complex refractometric sensors, one based on tapered optical fiber and the other based on suspended-core microstructure optical fiber, is presented.   © 2016 Optical Society of America

OCIS codes: (280.4788) Optical sensing and sensors; (060.2370) Fiber optics sensors; (160.5470) Polymers.

http://dx.doi.org/10.1364/AO.55.002574

1. INTRODUCTION

Optical refractometry is an effective tool for evaluating the refractive index (RI) of analytes to derive specific parameters such as density and liquid level for monitoring environmental contamination, leakage of liquids from pipes, and other hazards. The use of a fiber optic refractometric sensor (FORS) reduces the possibility of igniting an explosive or flammable medium, an attractive feature that allows FORS to be deployed in hazardous areas such as refineries and factories within the petrochemical industry. In addition, FORS can be integrated in remote monitoring applications.

FORSs are usually based on an intensity or wavelength measurement as they employ the total or partial reflection of light at the sensing element interface with the analyte. The corresponding reflection coefficient is a measure of the RI of the analyte [1]. The FORS with the external sensing element then employs the internal reflection of light at the surface of the sensing element that is in contact with the analyte. This kind of sensor operates in a wide range of measured analyte RI, for example, its utilization was discussed for cryogenic liquids (e.g., the RI of liquid helium is 1.0245 at 546 nm, and liquid nitrogen's RI is 1.205 at 589 nm [2,3]). This sensor was also proposed for aqueous solutions in order to evaluate the concentration of sugar [4] or salt [5] in industrial applications and for liquid level measurement in tanks and fuel reservoirs [6,7].

Sohn [8] proposed a liquid sensor consisting of a fiber Bragg grating (FBG) connected to a multimode silica fiber, whose operational principle is based on Fresnel's laws of reflection at the end face of a silica fiber; the FBG was used for monitoring the sensor head. The sensor operates in a RI range from 1.33 to 1.47. Kher *et al.* [9] measured the fuel adulteration through a long period grating (LPG) written in a B/Ge doped single-mode fiber with an average sensitivity of 1666 nm/RIU in the RI range from 1.33 to 1.43. Yan *et al.* [10] increased the sensor sensitivity in the RI range from 1.33 to 1.40 using a hybrid grating structure comprising 45° and 81° tilted fiber gratings that have been inscribed into a single-mode fiber. LPG- [10,11] and FBG- [12,13] based sensors allow the measurement of the liquid level. FORSs based on tapered silica optical fiber [14–16] are capable of measuring RI higher than silica's RI. Other structures based on a single-mode fiber (SMF) taper, such as a Michelson interferometer [17] and an asymmetrical fiber Mach–Zehnder interferometer based on a concatenating single-mode abrupt taper and core-offset section [18], can increase the sensitivity by modifying the diameter of the tapered section. Liang *et al.* [19] employed a LPG inscribed in a single-mode fiber that operates in the wide RI range from 1.32 to 1.47. Liquid level measurement of water and glycol was demonstrated via the multimode interference effect [20]. The development of novel optical fibers, such as

microstructure optical fibers (MOFs), brings a new range of possible applications. Webb *et al.* [21] used the cladding holes for acetylene gas sensing.

A FORS with an external sensing element offers certain advantages, none more significant than the ease in which it can be implemented and the wide RI range of measured analyte that is available. There are two standard configurations of FORS featuring an external sensing element: transmission and reflection [13,15,16,22]. A FORS operating in reflection mode brings two advantages when compared to the transmission mode. First, the sensitivity increases because the light travels twice inside the sensing element. Second, only one optical fiber is used in the sensor instead of the two used in the transmission mode. On the other hand, a directional optical device is required in the reflection mode.

We propose a sensor with an external semi-ellipsoidal sensing element that presents a facile approach to RI detection in a broad RI range from 1.00 to 1.47, whereby, with proper adjustment of the sensor parameters, sensitivity can be tuned to the selected RI range and sensitivity level. By employing polymethyl methacrylate (PMMA), material handling and processing is easy, and a low sensor cost is achieved. Our sensor can be utilized for detection of cryogenic fluids, water pollution monitoring, oil quality monitoring, and detection of water and oil leaks.

This paper is organized as follows. First, a FORS employing a semi-ellipsoidal sensing element made of PMMA is proposed, described theoretically, and optimized for measuring purposes. Experiments are then performed to validate its utilization. Finally, we present a comparison of our sensor with two developed FORSs based on a single-mode fiber taper (SMFT) and a suspended core microstructured optical fiber (SC-MOF).

2. THEORETICAL ANALYSIS

The proposed FORS with an external sensing element is formed using a multimode plastic optical fiber (MM-POF) coupled to a semi-ellipsoidal detection element made of PMMA and an aluminum mirror, allowing the doubling of the sensor working area. The proposed setup of the refractometric sensor in its generic form is shown in Fig. 1.

The variables used for the theoretical analysis were defined as: the half-width of the sensing element, a; the MM-POF core diameter, D; the numerical aperture of the MM-POF, NA; and the distance of the vertical axis of the sensing element to the MM-POF axis, L.

To perform analysis, dimensionless variables $\Lambda = L/a$ and $\Phi = D/a$ are introduced. The optical reflectance function of
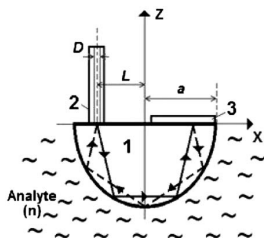

Fig. 1. Schematic of the sensor in reflection mode: 1, sensing element; 2, MM-POF; 3, mirror.

the sensor is given by $R = I_2/I_1$, where I_1 is the intensity of the optical signal transmitted by the fiber, and I_2 represents the optical intensity received by the fiber to account for the possibility of light traveling twice within the sensing element (see Fig. 1). Additionally, the relative reflectance has to be defined as $R^* = R_{ana}/R_{air}$, where R_{air} is the reflectance measured in air as an external analyte, and R_{ana} stands for the reflectance measured in an analyte apart from the air.

The theoretical analysis of the sensor was carried out by a numerical ray tracing method employing a refractometric fiber optical sensor [(SRFO) for its Spanish acronym: sensor refractométrico en fibras ópticas] and a specially developed computer program. It is possible to use geometrical optics because the dimension of the sensing element is greater than the wavelength of the signal.

SRFO allows us to introduce the physical and geometrical parameters of the optical fibers and detection elements such as the RI, NA, and the equation describing the shape of the sensing element. The mathematical model implemented considers nonpolarized and noncoherent light beams. The beam emerging from the fiber is composed of approximately 100,000 rays. Each ray is analyzed individually, from the angle it leaves the fiber's surface and next when it enters the sensing element along the path within the sensing element until it reaches the reflecting mirror. Next, the ray is analyzed along the return path through the sensing element, coupling again to the fiber or place where it leaves the detector surface elements. The Fresnel reflection coefficient was calculated at each reflection point, and the resulting intensity was determined for each ray. The element reflectance R was calculated by integrating the contributions of all rays reaching the fiber core within the limits of NA.

It was enumerated by a SRFO for three sensing elements of different shapes:

(a) hemisphere, which was presented in our previous works [2,20],
(b) semi-ellipsoidal element A, whose shape is described by the equation

$$x^2 + y^2 + 0.746z^2 = 1, \tag{1}$$

(c) a semi-ellipsoidal element B, whose shape is determined by the equation

$$0.92x^2 + 0.92y^2 + 1.27z^2 = 1. \tag{2}$$

In the simulations, we considered air as an external analyte, and the dimensionless distance Λ was varied in the range of 0.40–0.95 to find the best light coupling into the MM-POF core. Other parameters corresponded to the experimental setup (see Section 3). More specifically, we assumed the step-index optical fiber had a dimensionless core diameter $\Phi = 0.125$ and a $NA = 0.5$, and the same material of the optical fiber core and the sensing element PMMA had a RI of 1.492. The results of numerical modeling are shown in Fig. 2.

The performed simulation allowed us to choose a precise value of Λ to determine the best position of the MM-POF with respect to the center of the sensing element, to reach the best light coupling into the MM-POF, and to evaluate the response of the sensing element to changes of the external RI. The reflectance was then obtained as a function of RI, $R(n)$, for RIs
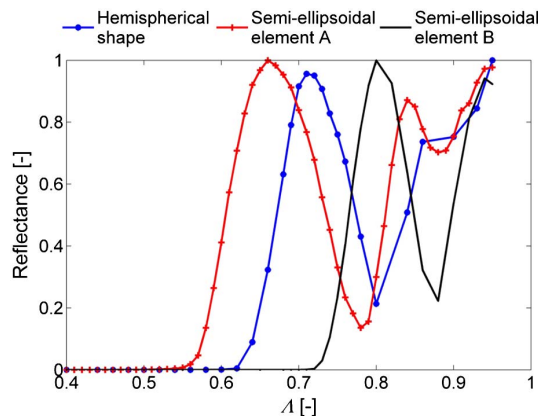
Fig. 2. Derived reflectance of the sensors as a function of dimensionless distance.

Table 1. Values of Λ Selected for Each Sensing Element

Element	Selected Values of Λ
Hemispherical shape	0.70, 0.86, 0.95
Semi-ellipsoidal element A	0.66, 0.84, 0.94
Semi-ellipsoidal element B	0.8, 0.94

ranging from $n = 1.00$ to $n = 1.47$ with increments of 0.005. The selected values of Λ for each sensing element are summarized in Table 1.

Figure 3 presents reflectance as a function of RI for specific values of Λ. It can be demonstrated that the sensing elements are sensitive to RI of the analyte at different intervals of n, indicating that the sensor could be used for detecting liquids with a relatively high RI such as gasoline [15,16] or even cryogenic liquids whose RI is relatively small [2]. Since the primary interest was to detect liquids with a RI within the interval of
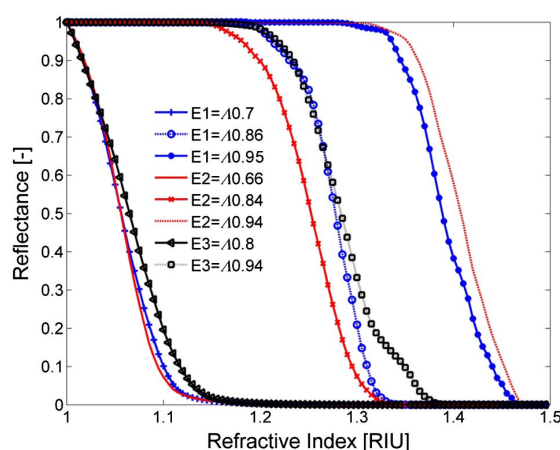

Fig. 3. Reflectance as a function of the refractive index for specific values of Λ. E1, hemispherical shape; E2, semi-ellipsoidal element A; E3, semi-ellipsoidal element B.

1.33–1.44, the hemispherical shape and semi-ellipsoidal element A can both be utilized in the desired RI range. However, the semi-ellipsoidal element A has a more linear response and more uniform sensitivity in comparison to the hemispherical element; therefore, element A better meets the performance requirements given at the beginning of FORS development.

3. EXPERIMENT SETUP

To validate analytical results, an experiment has been performed. The experimental setup (see Fig. 4) included a HeNe laser with a wavelength of 632.8 nm and a power output of 5 mW as the source. A step-index MM-POF (Jiangxi Daishing D-1000-1 made of PMMA with a core diameter of 0.98 mm, NA of 0.5, and a RI of 1.492) was used for connecting the laser source and the sensing element. The MM-POF was mounted on a translation stage that allowed movement along three axes. The semi-ellipsoidal element was fixed to the translation stage, and light was coupled from the MM-POF. An aluminum mirror was glued to the semi-ellipsoidal element. A PT331C phototransistor with a relative spectral sensitivity of ∼0.74 at $\lambda = 632.8$ nm was used as a photodetector. The output of the photodetector was connected to an Arduino UNO, which allowed us to process the data by MatLab.

For the experiment, a developed sensor with a semi-ellipsoidal element A was used (shown in Fig. 5). The semi-ellipsoidal element A, like the MM-POF, was made of PMMA to allow for better coupling from the fiber.

The experiment involved the characterization of the response of the semi-ellipsoidal element to variation of the RI of the analyte. The coupling position from the fiber in terms of Λ was changed to compare the experimental and theoretical data and to validate the sensor reflectance.

Five analytes featuring different RIs (see parameters in Table 2) were selected to evaluate the reflectance of the sensing element measured at a wavelength of 589 nm.
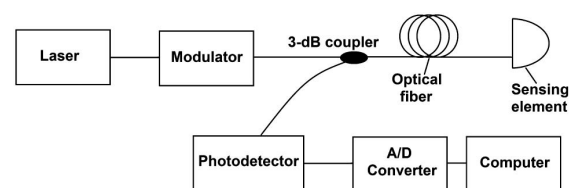
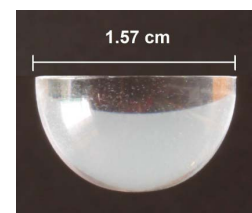

Fig. 4. Block diagram of the experimental setup.

Fig. 5. Semi-ellipsoidal element A.

Table 2. Refractive Indices of Selected Analytes at $\lambda = 589$ nm and 20°C

Analyte	Refractive Index
Water	1.333
Salt water (120 ppm)	1.347
Salt water (350 ppm)	1.375
Antifreeze	1.392
Gasoline	1.432

To evaluate the main advantages of the proposed sensor, its performance was further compared with two other more complex FORSs developed by our team. The first sensor was based on a SMFT, and the second sensor was based on a SC-MOF.

The SMFT sensor was prepared using a flame-heating technique from a conventional silica SMF. The taper was created with two 1-cm-long adiabatic transition regions and with a 1-cm-long taper waist with a diameter of 4.3 μm. The SC-MOF sensor was made of pure silica glass with a core diameter of 2.75 μm, a bridge width of 170 nm, and cladding hole dimensions of 30 × 40 μm. The SC-MOF was precisely cleaved to achieve a perfect cleave with no surface distortion to provide equal capillary forces for all three cladding holes. Both sensors were stored at room temperatures of 22°C–25°C and at a humidity of 35%–45% before the measurements.

Both the SMFT and the SC-MOF sensors were tested with identical analytes, taking into account the wavelength dependence of RIs in both simulations and measurements (e.g., the RI of water $n_{H_2O} = 1.318$ at $\lambda = 1550$ nm and 20°C was calculated by the Cauchy equation [23]). The SMFT sensor was completely immersed in each analyte during the tests. In the case of the SC-MOF, the length of capillaries filled with analytes was 1 cm. A detailed description of the SC-MOF sensor measurement setup can be found in [24], and the SMFT measurement configuration is similar to the one presented in [14], with the modification of a laser source for the one working at 1550 nm, an appropriate photodetector, and single-mode optical fibers. The reference measurements were done with an SMFT sensor in air. Between measurements of particular analytes, each SMFT was first purified in isopropyl alcohol and then dried.

All measurements with the SMFT and SC-MOF were conducted at a wavelength of 1550 nm. We consider the use of different wavelengths completely justified because the semi-ellipsoidal sensor is made of PMMA, which is transparent in the visible and near-IR range. In contrast, the SMFT and SC-MOF sensors operate at longer wavelengths while having lower material attenuation, maintaining the single-mode regime and providing increased evanescent wave overlap. The main purpose was to validate optical sensors within the same RI range.

4. RESULTS

The reflectance function of the semi-ellipsoidal element A was obtained for five analytes with Λ ranging from 0.4 to 1.0 as determined by the previous simulation; note that no light is coupled for $\Lambda < 0.53$. The reflectance in air was the maximum value of reflectance that we used as a reference in sensor characterization.

The experimental results shown in Fig. 6 indicate that our proposed sensor can be set to a specific RI range by modifying the dimensionless parameter Λ. The range up to 0.66 is more suitable for gas measurement; higher values of Λ have to be set for liquid analytes.

The theoretical and experimental results presented in Fig. 7 exhibit a small deviation ($\sigma = 0.035$). We attribute this deviation to finite material absorption, material nonhomogeneity, and the nonperfect shape of the sensing element, which we did not consider in the theoretical analyses.

In the next step, we compared performance of our developed sensor with SMFT and SC-MOF. Furthermore, we added expected sensitivities for other values of Λ. To compare the sensors' performance, the intensity sensitivity parameter was determined as

$$S = \frac{\Delta I}{\Delta n}, \qquad (3)$$

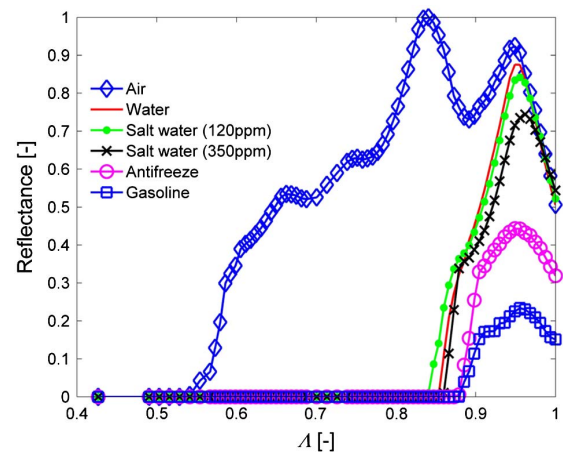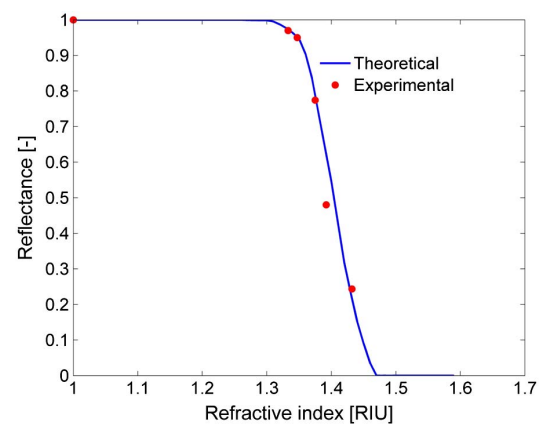**Fig. 6.** Reflectance of the semi-ellipsoidal element A for selected analytes as a function of Λ.

Fig. 7. Theoretical and experimental reflectance function $R(n)$ of the semi-ellipsoidal element under $\Lambda = 0.94$.

where ΔI is the difference between the optical intensity for the two analytes with the closest RI, and Δn is the RI difference. The observed sensitivity of the three sensors $S(n)$ is displayed by graphs in Fig. 8. The inset of Fig. 8 shows the predicted sensitivity of the semi-ellipsoidal sensor for different parameters Λ.

We can observe that the sensor with the semi-ellipsoidal element A can be utilized in the RI range of 1.00–1.47, where for particular regions of interest a specific parameter Λ must be set. For example, the inset in Fig. 8 shows a predicted sensibility of ∼200 dB/RIU in the RI range of 1.00–1.20 under $\Lambda = 0.66$, with the peak sensitivity $S > 400$ dB/RIU at the RI of 1.04, thus being suitable for detection of cryogenic fluids.

By changing the Λ parameter to 0.84 (see inset in Fig. 8), the sensitivity increases up to 1500 dB/RIU in the RI range of 1.25–1.32. By further increasing Λ to 0.94, the RI range of operation shifts to 1.33–1.47. The sensor with an external sensing element and $\Lambda = 0.94$ (denoted as a sensor with semi-ellipsoid element A) was afterward compared to the SMFT and SC-MOF sensors.

Our sensor with semi-ellipsoid element A matched the simulation results (as depicted in Fig. 7) and provided a resolution of 3.08×10^{-4} in general laboratory conditions. (The ideal value is approximately one order smaller in the vicinity of RI = 1.40 when considering precise temperature stabilization of the whole measurement setup.)

In the range of 1.33–1.40, we obtained an increase in sensitivity of our sensor from 35 dB/RIU up to 180 dB/RIU, which is comparable to SMFT and SC-MOF sensor sensitivity in the same range. This is a quite good result, given that the sensor with the semi-ellipsoidal element is more simple and easy to fabricate than more complex SMFT and SC-MOF sensors.

The sensitivity range within a RI range of 1.41–1.43 is dominated by SMFT and SC-MOF with sensitivity above 500 dB/RIU for both sensors. The better performance, in comparison to the sensor with the semi-ellipsoidal element A ($S \approx 250$ dB/RIU), is attributed to the fact that the analyte's RI is close to the RI of the sensor material (silica) of both SMFT and SC-MOF.

For the FORS with semi-ellipsoidal sensing element A at Λ of 0.94, the simulations showed that the sensitivity S exponentially increased from ∼300 dB/RIU at RIU of 1.42 and

exceeded 500 dB/RIU at RIU > 1.452. Some oils have RIs in the range of 1.44–1.47; therefore, the aforementioned FORS sensor can find applications in the oil industry.

5. CONCLUSION

We presented a theoretical and simulation background for the development and optimization of a fiber optic refractometric sensor with a semi-ellipsoidal sensing element. The possibility of varying the number of serial reflections at the sensing element surface by changing the position of the optical fiber with respect to the axis of the sensing element was discussed. This change expressed by parameter Λ enables tuning of the working RI range. In particular, under $\Lambda = 0.66$, cryogenic liquids can be detected with high sensitivity (∼500 dB/RIU at a RI of 1.04). Based on the aforementioned background, a sensor with a semi-ellipsoidal sensing element and parameter $\Lambda = 0.94$ was implemented and tested with five analytes in the RI range of 1.333–1.432. The difference between the predicted and observed behavior of the sensor was negligible ($\sigma = 0.035$). In the RI range of 1.333–1.392, the sensor exhibited a sensitivity of 180 dB/RIU (contaminated water fits in this particular RI range). The aforementioned sensitivity is close to that of two other, more complex sensors (SMFT and SC-MOF) that we also developed and tested. In the RI range of 1.44–1.47, the sensitivity of the sensor with the semi-ellipsoidal sensing element exceeded 500 dB/RIU (some oils fit in this specified range).

The main advantage of the sensor is its simplicity combined with its high sensitivity to the external RI and a capability to cover a broad measuring range between 1 and 1.47 RIU only by varying the position of the optical fiber with respect to the axis of the sensing element. Potential applications of this sensor include detection of cryogenic fluids, monitoring water pollution and some oils, and, in particular, detection of oil leaks.

Fig. 8. Sensitivity of developed sensors as a function of the RI of an external analyte.

REFERENCES

1. S. Yin and P. Ruffin, *Fiber Optic Sensors* (Wiley, 2002).
2. K. E. Romo-Medrano and S. N. Khotiaintsev, "An optical-fibre refractometric liquid-level sensor for liquid nitrogen," Meas. Sci. Technol. **17**, 998–1004 (2006).
3. T. Chen, Q. Wang, R. Zhang, Y. Lin, and K. P. Chen, "Distributed liquid level sensors using self-heated optical fibers for cryogenic liquid management," Appl. Opt. **51**, 6282–6289 (2012).
4. M. Shao, X. Qiao, H. Fu, H. Li, Z. Jia, and H. Zhou, "Refractive index sensing of SMS fiber structure based Mach–Zehnder interferometer," IEEE Photon. Technol. Lett. **26**, 437–439 (2014).
5. S. Khotiaintsev, K. Khotiaintsev, and A. Garcia-Moreno, "Modeling of the fiber-optical water salinity sensor," in *8th International Conference on Laser and Fiber-Optical Networks Modeling*, Kharkiv, Ukraine, 2006, pp. 36–38.
6. S. Khotiaintsev, "Discrete POF liquid-level sensor for measuring the level of gasoline and detecting water in automobile tanks," in
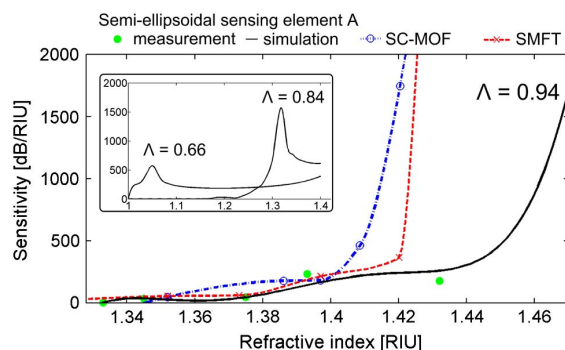
Proceedings of the 18th International Conference on Plastic Optical Fibers (2009), pp. 1–4.

7. S. Khotiaintsev, E. Llanito-Caudillo, S. Perez-Garcia, and J. Morales-Farah, "Optical-fiber refractometric sensor with semi-cylindrical optical detection element for measuring the level of gasoline," in _Proceedings of the IEEE Conference on Electronics, Robotics and Automotive Mechanics_ (IEEE, 2009), pp. 468–473.

8. K. R. Sohn, "Liquid sensors using refractive intensity at the end-face of a glass fiber connected to fiber-Bragg grating," Sens. Actuators A **158**, 193–197 (2010).

9. S. Kher, S. Chaubey, J. Kishore, and S. M. Oak, "Detection of fuel adulteration with high sensitivity using turnaround point long period fiber gratings in B/Ge doped fibers," Sens. J. **13**, 4482–4486 (2013).

10. Z. Yan, C. Mou, Z. Sun, K. Zhou, H. Wang, Y. Wang, and L. Zhang, "Hybrid tilted fiber grating based refractive index and liquid level sensing system," Opt. Commun. **351**, 144–148 (2015).

11. Y. Huang, B. Chen, G. Chen, H. Xiao, and S. U. Khan, "Simultaneous detection of liquid level and refractive index with a long-period fiber grating based sensor device," Meas. Sci. Technol. **24**, 095303 (2013).

12. Q. Jiang, D. Hu, and M. Yang, "Simultaneous measurement of liquid level and surrounding refractive index using tilted fiber Bragg grating," Sens. Actuators A **170**, 62–65 (2011).

13. G. Tsigaridas, D. Polyzos, A. Ioannou, M. Fakis, and P. Persephonis, "Theoretical and experimental study of refractive index sensors based on etched fiber Bragg gratings," Sens. Actuators A **209**, 9–15 (2014).

14. M. Komanec, T. Martan, T. Nemecek, and S. Zvanovec, "Multimode fiber tapers for reproducible refractometric liquid detection," Opt. Eng. **54**, 047102 (2015).

15. D. Wu, Y. Zhao, and O. Wang, _SMF Taper Evanescent Field Based RI Sensor Combined with Fiber Loop Ring Down Technology_ (IEEE, 2015).

16. A. Mukherjee, D. Munsi, V. Saxena, R. Rajput, P. Tewari, V. Singh, and P. Gupta-Bhaya, "Characterization of a fiber optic liquid refractive index sensor," Sens. Actuators B **145**, 265–271 (2010).

17. Z. Tian, S. S. Yam, and H. P. Loock, "Refractive index sensor based on an abrupt taper Michelson interferometer in a single-mode fiber," Opt. Lett. **33**, 1105–1107 (2008).

18. G. Yin, S. Lou, and H. Zou, "Refractive index sensor with asymmetrical fiber Mach-Zehnder interferometer based on concatenating single-mode abrupt taper and core-offset section," Opt. Laser Technol. **45**, 294–300 (2013).

19. T. C. Liang, H. S. Huang, and M. H. Chuang, "Study on fiber grating sensors for concentration measurement of cottonseed oil adulteration in pure olive oil," Microelectron. Eng. **148**, 21–24 (2015).

20. J. E. Antonio-Lopez, J. J. Sanchez-Mondragon, P. LiKamWa, and D. A. May-Arrioja, "Fiber-optic sensor for liquid level measurement," Opt. Lett. **36**, 3425–3427 (2011).

21. A. S. Webb, F. Poletti, D. J. Richardson, and J. K. Sahu, "Suspended-core holey fiber for evanescent-field sensing," Opt. Eng. **46**, 010503 (2007).

22. V. Svirid, S. Khotiaintsev, and P. L. Swart, "Novel optical fiber refractometric transducer employing hemispherical detection element," Opt. Eng. **41**, 779–787 (2002).

23. M. Born and E. Wolf, _Principles of Optics_ (Pergamon, 1980).

24. T. Nemecek, M. Komanec, M. Martan, R. Ahmad, and S. Zvanovec, "Suspended-core microstructured fiber for refractometric detection of liquids," Appl. Opt. **54**, 8899–8903 (2015).

4.6   Refractometric detection of liquids using tapered optical fiber and suspended core microstructured fiber: a comparison of methods

This chapter is a version of the published manuscript:

Relevance to my Ph.D. thesis:

A detailed comparison of TOF and SC-MOF sensors is presented. To evaluate our previous results and to compare both detection methods, we examined TOFs and SC-MOFs of identical core and waist diameters on identical liquid analytes. For this purpose, an innovative TOF encapsulation, including pipeline systems, was presented. Fiber design, theoretical simulations, and measurements are thoroughly described for both methods. Finally, TOF and SC-MOF methods are evaluated, sensitivities and resolutions of the sensors are presented, and limits of detection are shown. Advantages and drawbacks, with respect to potential applications, and an assessment of the benefits of each are discussed.

appliedoptics

Refractometric detection of liquids using tapered optical fiber and suspended core microstructured fiber: a comparison of methods

T. Martan,* T. Nemecek, M. Komanec, R. Ahmad, and S. Zvanovec

Department of Electromagnetic Field, Faculty of Electrical Engineering, Czech Technical University in Prague,
Technicka 2, Prague, Czech Republic
*Corresponding author: martant@fel.cvut.cz

Detecting explosive, flammable, or toxic industrial liquids reliably and accurately is a matter of civic responsibility that cannot be treated lightly. Tapered optical fibers (TOFs) and suspended core microstructured optical fibers (SC MOFs) were separately used as sensors of liquids without being compared to each other. We present a highly sensitive time-stable TOF sensor incorporated in the pipeline system for the in-line regime of measurement. This paper is furthermore focused on the comparison of this TOF and SC MOF of similar parameters for the detection of selected liquids. A validated method that incorporates TOF and SC MOF of small core (waist) diameter for refractometric detection is presented. The principle of detection is based on the overlap of an enhanced evanescent wave with a liquid analyte that either fills the cladding holes of the SC MOF or surrounds the waist area of the TOF. Optical power within the evanescent wave for both sensing structures and selected liquid analytes is analyzed. Measurement results concerning TOF and SC MOF are compared. Calculations to ascertain the limit of detection (*LOD*) for each sensor and the sensitivity (*S*) to refractive indices of liquid analytes in the range of 1.4269 to 1.4361 were performed at a wavelength of 1550 nm with the lowest refractive index step of 0.0007. Results affirming that $S = 600.96$ dB/RIU and $LOD = 0.0733$ RIU for the SC MOF and $S = 1143.2$ dB/RIU and LOD of 0.0026 RIU for the TOF sensor were achieved, clearly illustrating that TOF-based sensors can reach close to two times greater sensitivity and 30 times higher limit of detection. This paper extends the comparison of the fiber sensors by discussing the potential applications. © 2017 Optical Society of America

OCIS codes: (280.4788) Optical sensing and sensors; (060.2370) Fiber optics sensors; (060.4005) Microstructured fibers.

https://doi.org/10.1364/AO.56.002388

1. INTRODUCTION

Establishing systems for detecting explosive, flammable, or toxic liquids that are both reliable and fireproof are crucial for human safety and for protecting the environment, not to mention their role in controlling industrial chemical processes [1–3]. Detecting such liquids can be done by silica-based optical fibers (fiber optic sensors), which are not flammable and are immune to outer electromagnetic interferences. A variety of optical fibers, including conventional fibers with long-period gratings [4], fiber Bragg gratings [5] or etched fiber Bragg gratings [6,7], polymer clad silica (PCS) fibers [8] combined with coated adsorption layers for enhanced sensitivity or equipped by opto-chemical transducers to be able to distinguish specific chemical substance(s) [9], were used for the detection of liquids. To enhance sensing features, specialized optical fibers, such as tapered optical fibers (TOFs) [10–12] and microstructured optical fibers (MOFs), in particular, suspended core

microstructured optical fibers (SC MOFs) [13,14], were designed for this purpose.

The basic principle of detecting liquids by TOFs and SC MOFs hinges upon an evanescent wave overlap in a liquid analyte resulting in a change in the attenuation of the guided light. An SC MOF is characterized by an inner structure consisting of an extremely small core (with its diameter in units of microns or less than one micron) surrounded by three large cladding air holes. Both the small SC MOF core size and a tested liquid filling the cladding holes contribute to an increase in loss due to the evanescent wave propagating in the holes. The SC MOF can be applied as a refractometric sensor for monitoring gasses or liquid analytes and for DNA analysis, as well as being used for fluorescence or Raman spectroscopy purposes [15–18]. A theoretical study has been carried out to capture the enhanced resolution and sensitivity of SC MOFs with core diameters below 1 μm [19]. Such a configuration leads to an

increase in the overlapping of the evanescent wave propagating along the core-cladding boundaries with the analyte. Exposed-core SC MOFs for liquid filling were presented in Ref. [20], while other means of liquid filling, including the filling of a hollow-core PCF with double selectivity resulting in a liquid-core and liquid-cladding fiber, were proposed in Ref. [21]. The SC MOFs, together with inner surface functionalization, e.g., equipped with a silver wire guided in one cladding hole, are suitable for use as surface plasmon resonance (SPR) sensors [22–24].

TOF sensors are usually based on tapered conventional optical fibers, as is the case with single-mode optical fibers (SMFs) or multimode optical fibers [25–27]. TOF can be defined as a fiber heated over a defined length and stretched to an extremely narrow filament resulting in a small diameter. Occasionally, the diameter of the taper waist can also be measured of the order of a few hundreds of nanometers or even below 100 nm in which case the tapers are called optical nanowires or nanotips [28–30]. TOFs are also applied as (bio) sensors in reflection (fiber probes) or transmission arrangements, e.g., in medicine, botany, or industrially, as a fiber optic refractometer, a SPR sensor, or a sensor equipped with an optical chemical transducer for pH measurement [31–33].

This paper introduces a new TOF principle incorporated in pipeline systems for the in-line regime of measurement. In the next step, it provides a comparison of SMF-based TOF and silica-based SC MOF sensors, which were designed, developed, and subsequently analyzed for the detection of selected liquid analytes. In particular, to validate simulation results and to illustrate the comparison better, TOF of comparable parameters to SC MOF, i.e., both having the same core diameters, were prepared. The sensitivity and limits of detection (*LOD*s) of both TOF and SC MOF of similar parameters were analytically and experimentally determined and validated. The comparison of both kinds of fiber sensors assesses additional benefits and drawbacks with regard to future applications.

2. TAPERED OPTICAL FIBER AND SUSPENDED CORE MICROSTRUCTURED OPTICAL FIBER

A. Tapered Optical Fiber

Tapered optical fiber was prepared by the flame brushing technique, i.e., by heating (to approximately 1700°C) a section of the SMF (core/cladding diameter of 9/125 μm) with a hydrogen–oxygen flame. A gas burner is moved from left to right between two fiber holders, while both ends of the fiber (fixed in holders) are pulled in opposite directions. The movement, stretching, and heating processes are fully PC controlled; see Fig. 1(a). The process gives rise to two specific parts of the TOF: the taper waist (defined by the movement of the gas burner) and two taper transition areas. The taper waist lies in the thinnest central section of the TOF and the taper transitions are regions with narrowing diameters between the untapered original fiber and the taper waist; see Fig. 1(b). A photograph of the tapering apparatus for the preparation of the TOF sensor can be seen in Fig. 1(c). The protective tube is prepared before the tapering process (it is laterally drilled for liquid input and output) and SMF is placed through the tube
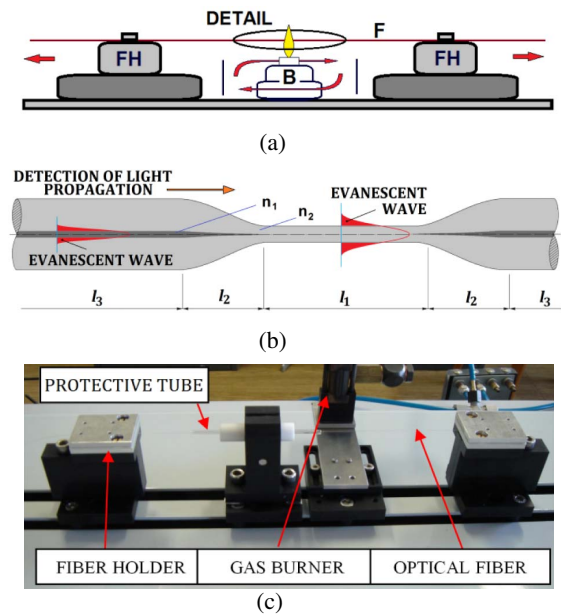

Fig. 1. (a) Schematic picture of the tapering process. F, optical fiber; B, burner; FH, fiber holder. (b) Details of a longitudinal structure of the TOF made from SMF—regions and evanescent wave. l_1, waist region; l_2, transition area; l_3, region of the untapered optical fiber; n_1, refractive index of the core (doped silica); n_2, refractive index of the cladding (pure silica). (c) Photograph of the tapering apparatus for preparation of the TOF sensor.

and fixed in holders; see Fig. 1(c). The TOF is covered by the protective tube and glued after the tapering process.

The TOF was prepared with the following parameters: a tapered waist diameter of 2.75 μm, a length of 5.0 mm, an exponential transition length of 16.0 mm, and the total length of the TOF was 37.0 mm. A scanning electron microscope (SEM) photograph of the longitudinal section of the developed TOF waist and the taper transition is shown in Figs. 2(a) and 2(b),
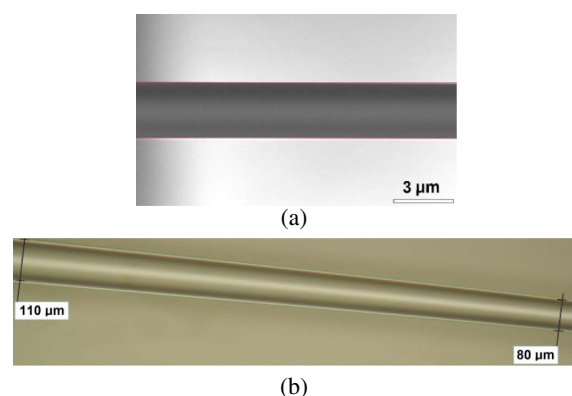

Fig. 2. Photographs of the homogeneous longitudinal sections of the TOF. (a) SEM photograph of the 2.75 μm diameter TOF waist. (b) The taper transition.
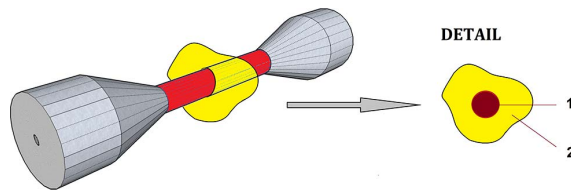
Fig. 3. Longitudinal structure of a TOF made from SMF. Detail: 1, cross section of the TOF waist (sensing) area; 2, the liquid analyte located around the TOF waist (cladding) region.

Fig. 5. SC MOF cross section. (a) Microscope photograph of the SC MOF cross section. (b) SEM photograph of the 2.75 μm core area.

respectively. Photographs of the waist and the transition section of the TOF are presented to show the homogeneity of its surface. The diameter of the transition gradually (along 16.0 mm) decreases from the untapered part (diameter of 125 μm) to the waist (diameter of 2.75 μm) in order to minimize insertion loss. An example of part of the transition section is shown in Fig. 2(b) from the diameter of 110 μm down to 80 μm.

The germanium-doped core of the original SMF, with refractive index n_1, is narrowed by tapering over the transition area (with the core diameter decreasing) resulting in a tapered waist with the original doped core almost completely negligible. The taper waist is thus of pure silica. From this point of view, both the waist of the TOF and the SC MOF core consist of pure silica material. The TOF waist area is used for sensing because of its enhanced evanescent wave; see Figs. 1(b) and 2(a). In the case of the TOF waist, the original cladding acts as a new core and the surrounding liquid analyte represents a new cladding; see Fig. 3. The length of the TOF waist was optimized to be of similar length as the level of the liquid filled in the cladding holes of the SC MOF. The SMF-based TOF sensor has been designed for a wavelength of 1550 nm due to the low loss of the fused silica and the enhanced overlap of the evanescent wave in this band compared to the visible spectral band for reaching a higher sensitivity.

B. Suspended Core Microstructured Optical Fiber

For the detection, a silica-based SC MOF with a core diameter of 2.75 μm and three cladding holes has been designed for a wavelength of 1550 nm. Detailed descriptions of the inner structure of the SC MOF, in terms of its cross section and longitudinal structure showing particular regions and an evanescent wave, are presented in Figs. 4(a) and 4(b), respectively. Mode intensity distributions within the designed structure of
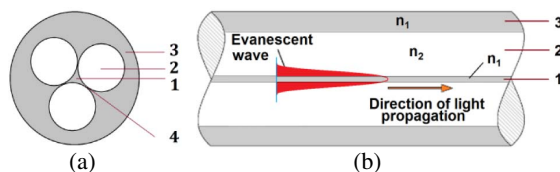
the SC MOF were numerically analyzed using the finite element method (FEM) technique.

The SC MOF has been fabricated with a core diameter of 2.75 μm and a bridge thickness of 0.27 μm. The radial diameters of the three cladding holes are all 29.73 μm, i.e., the area of one cladding hole is 925 μm². The 125 μm outer diameter of the SC MOF was designed to provide a facile connection to SMFs.

A cross section of the SC MOF with a stripped polymeric jacket is shown in Fig. 5(a). Figure 5(b) shows the Jeol JSM-6510 SEM detail of the core area together with three silica bridges. The inscribed circle represents 2.75 μm diameter of the fiber core and corresponds to the diameter of the fiber core discussed further in this paper.

C. Detection Setup

1. Arrangement with the TOF

The set-up for liquid analyte detection containing the TOF sensor built within the pipeline system is shown in Fig. 6(a).

A superluminescent diode (SLED) radiating with a central wavelength of 1550 nm, a full width at half-maximum bandwidth of 56.0 nm, and maximal output power of 1.4 mW was used as a wideband light source. Light from the SLED was coupled into an SMF patchcord and then guided to the TOF sensor. The liquid analyte was pumped into the pipeline system from "input of liquid" to fill the area of the waist of the TOF sensor in Phase 1; see Fig. 6(a). The light was further guided from the TOF sensor to the second SMF patchcord and attenuation of light was measured by the detector (DET). In Phase 2 (after measuring the liquid analyte), the liquid analyte was pumped out from the area of the TOF sensor

Fig. 4. (a) Cross section of the SC MOF. (b) Longitudinal structure of the SC MOF—regions and evanescent wave: 1, core area; 2, cladding holes; 3, outer silica cladding; 4, silica bridges; n_1, refractive index of the core or refractive index of outer cladding; n_2, refractive index of the cladding holes (filled by a liquid analyte).
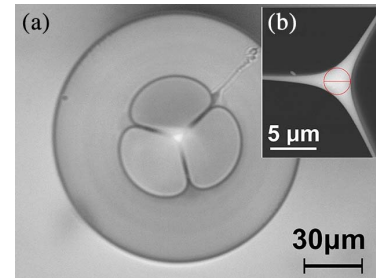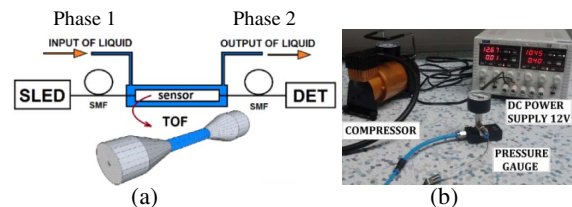

Fig. 6. (a) Schematic of the measurement setup for the detection of liquids using TOF. SLED, superluminescent diode; SMF, single-mode fiber patch cord; TOF, tapered optical fiber sensor; DET, detector. (b) System for liquid analyte pumping.

through "output of liquid"; see Fig. 6(a). An air compressor was used for the liquid analyte pumping in and pumping out utilizing negative pressure. The compressor was connected into the output part of the pipeline system. The pressure was controlled by a pressure gauge; see Fig. 6(b).

2. Arrangement with the SC MOF

The prepared and characterized SC MOF of a length of 1.5 m was used as a sensing element in the measuring setup (see Fig. 7), which consisted of two phases: Phase 1, which includes the air reference measurement [Fig. 7(a)] and the SC MOF filling process [Fig. 7(b)], and Phase 2, which involves the inspection of the liquid level in the SC MOF cladding holes [Fig. 7(c)] and cutting the SC MOF by a cleaver [Fig. 7(d)].

The same SLED as for TOF measurements was connected to the SMF, whereby light was further collimated (COL) and focused 40× by the objective (OBJ), with an NA = 0.65, directly into the core area of a section of the SC MOF; see Fig. 7.

Phase 1 was divided into two steps. First [Fig. 7(a)], the cladding holes of the SC MOF were filled only by air (without a liquid analyte) for reference measurement. The reference sensor attenuation was measured at the end of the SC MOF by the DET—a germanium photodiode with an optical power range of 50 nW to 40 mW and a wavelength range of 700–1800 nm. In the next step [Fig. 7(b)], the cladding holes of the SC MOF were filled by a liquid analyte by capillary forces.

Phase 2 is also divided into two steps. First [Fig. 7(c)], the level of liquid in the SC MOF cladding holes, filled with tested liquid analyte from previous step, was inspected by a

Fig. 7. Schematic of the measurement setup for the detection of liquid analytes using the SC MOF. Phase 1: (a) a section of the SC MOF whose cladding holes are filled by air, and (b) a section of the SC MOF whose cladding holes are filled by liquid analyte (reference). Phase 2: (c) a section of the SC MOF whose cladding holes are filled by a measured liquid analyte, and (d) CUT is the cleaver used for cutting the fiber in the region of the air-filled cladding holes (in the anterior region filled by liquid analyte). SLED, superluminescent diode; SMF, single-mode fiber patch cord; COL, collimator; OBJ, 40× objective used for focusing light; SC MOF, section of the suspended core microstructured optical fiber; OBJ, objective to observe liquid level; CAM, digital camera used for observation; PC, computer; DET, detector.

microscope equipped with an objective (OBJ) for direct observation and by a digital camera (CAM) connected to a computer (PC) to evaluate data and pictures. Attenuation of light guided into the core of the SC MOF was measured for different liquid analytes by the DET. In the next step [Fig. 7(d)], the SC MOF was cut by a cleaver (CUT) in the region of those cladding holes filled by air (in front of the region filled by a liquid analyte), i.e., part of the SC MOF filled by a measured (tested) analyte is cut and discarded by a fiber cleaver, and the SC MOF is prepared to refill the cladding holes by a liquid analyte for another measurement. The measurement setup was kept at a constant room temperature of 20°C.

3. RESULTS

Laboratory testing of approaches employing the TOF or SC MOF on explosive and/or flammable or toxic liquids (e.g., on hydrocarbons, such as gasoline, heptane, hexane, toluene, tetrahydrofuran, or other toxic liquids as dioxane or chloroform) could be harmful to the health of laboratory personnel, so appropriate harmless liquid analytes were prepared to test the TOF or SC MOF sensor. We substituted the targeted dangerous liquids with environmentally friendly azeotropic liquid mixtures of glycerol dissolved in water in different ratios to achieve refractive indices comparable to hydrocarbons or mixtures of hydrocarbons in water. Glycerol (1,2,3-propanetriol) $C_3H_5(OH)_3$ represents a hygroscopic, colorless, viscous liquid (trihydric alcohol) that is not explosive, flammable, or toxic, thereby making it suitable for such tests. The glycerol molecule is polar. Therefore, it is unlimitedly miscible with water due to the presence of hydroxyl groups [34]. Refractive indices of these liquids must be lower than the refractive index of fused silica for a wavelength of 1550 nm. The liquid mixtures featuring refractive indices close to chloroform $CHCl_3$, which is toxic, volatile, and hazardous, or 1,4-Dioxane $C_4H_8O_2$, a volatile solvent used in laboratories, were prepared; see Table 1. Mixtures of glycerol (GLY) of defined concentrations dissolved in water (H_2O) and related refractive indices (RI) measured at 632 nm (at 20°C) and recalculated RI at 1550 nm are listed in Table 1. Values of RI of water (1.3180 at 1550 nm and 20°C) and glycerol (1.4594 at 1550 nm and 20°C) were calculated by the Cauchy equation [35]. Samples of 1-propanol (RI = 1.3738 at 1550 nm) were used as references for measuring these prepared liquid mixtures [36]. Refractive indices of liquid analytes

Table 1. Prepared Mixtures of Glycerol Dissolved in Water of Defined Concentrations and Corresponding Refractive Indices Measured at 632 nm and Recalculated at 1550 nm[a]

Mixture Name	RI at 632 nm	RI at 1550 nm	Concentration
1-propanol	1.3816	1.3738	100% 1-propanol
GLY77.0	1.4383	1.4269	77.0% GLY, 23.0% H_2O
GLY78.0	1.4399	1.4283	78.0% GLY, 22.0% H_2O
GLY80.5	1.4437	1.4318	80.5% GLY, 19.5% H_2O
GLY81.0	1.4445	1.4325	81.0% GLY, 19.0% H_2O
GLY83.5	1.4484	1.4361	83.5% GLY, 16.5% H_2O

[a]The reference is 1-propanol.

were continuously measured (controlled) by a WYA-Z Digital Refractometer working in the full automatic regime at 632 nm for refractive indices nD from 1.3000 to 1.7000, with a resolution of nD = 0.0001, featuring a measurement accuracy of ±0.0002 and recalculated at wavelength 1550 nm according to Ref. [36]. Determination of the refractive index of concentration was done by

$$\text{RI}(m_n)_{1550} = \frac{\text{CON(GLY)}}{100}\text{RI(GLY)}_{1550}$$
$$+ \frac{\text{CON(H}_2\text{O)}}{100}\text{RI(H}_2\text{O)}_{1550}, \qquad \textbf{(1)}$$

where $\text{RI}(m_n)_{1550}$ is the recalculated refractive index at 1550 nm (and m_n stands for the mixture name), CON(GLY) is the percentage concentration of glycerol, CON(H$_2$O) is the percentage concentration of water, RI(GLY)$_{1550}$ is the refractive index of glycerol at 1550 nm, and RI(H$_2$O)$_{1550}$ is the refractive index of water at 1550 nm. For example, the recalculation of GLY77.0 at a wavelength of 1550 nm is calculated as

$$\text{RI(GLY77.0)}_{1550} = \frac{77.0\%}{100}1.4594 + \frac{23.0\%}{100}1.3180$$
$$= 1.4269.$$

The total difference of the refractive indices in the measurement, i.e., between GLY83.5 and GLY77.0, is 0.0092, and the minimally reached difference of the prepared mixtures is 0.0007; see Table 1.

A. TOF Simulations and Measurements

A prepared TOF, particularly its waist area, was numerically analyzed in COMSOL Multiphysics. The fundamental core mode intensity profiles of the TOF were calculated by using the FEM technique at a wavelength of 1550 nm. Results of these simulations for the TOF waist surrounded by air and by 1-propanol are shown in Fig. 8.

The calculated n_{eff}, A_{eff}, and powers within the evanescent wave in SC MOF cladding holes filled by air, 1-propanol or by GLY77.0 to GLY83.5, are presented in Table 2. Numerical analyses show that the overlap of an evanescent wave (power of evanescent wave in the surrounding analyte) for 1-propanol is almost 11 times higher than the overlap of an evanescent wave for air; see the details in Table 2.

The TOF sensor incorporated in the protective glass tube was tested by filling this tube with a liquid analyte ranging from GLY77.0 to GLY83.5. The detection of other liquids was realized by using the pipeline developed for the insertion of testing liquids; see Fig. 9.

The SMF patchcord was connected to the light source on the input side, the TOF sensor was inside the protective glass tube, and the SMF patchcord was connected to the detector on the output side; see Fig. 9. A schematic picture of the measurement is shown in Fig. 6, which illustrates how the TOF sensor was completely surrounded (immersed) by a measured liquid analyte. After each measurement, the TOF sensor was cleaned by 1-propanol and dried by air, which was also used as a reference for measurements. Temporal changes of attenuation of the TOF based on refractive index changes for GLY77.0 to GLY83.5, together with the reference (1-propanol) and air level, i.e., the reversibility of the operation of the TOF, are shown in Fig. 10.
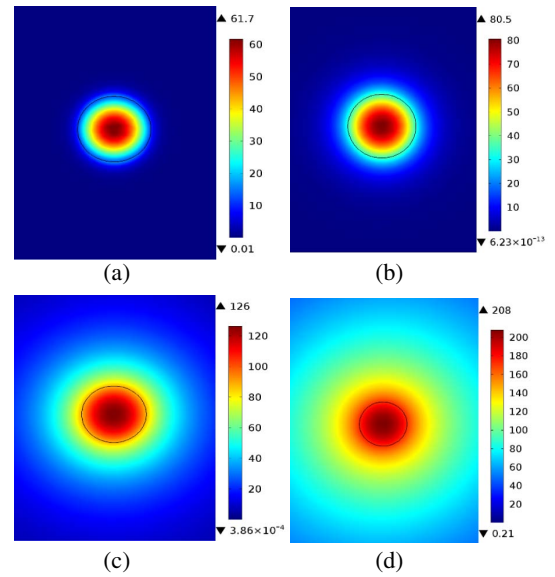
Fig. 8. Calculated, fundamental core mode, and normalized intensity of electric field profiles of the TOF. The taper waist is surrounded by (a) air, (b) 1-propanol, (c) GLY77.0, and (d) GLY83.5. The black ring represents the boundary of the TOF waist.

Table 2. Calculated Optical Power Carried by an Evanescent Wave of the TOF[a]

Analyte	Refractive Index	n_{eff} [−]	A_{eff} [μm^2]	Power in Analyte [%]
Air	1.0002	1.3083	4.7114	1.53
1-propanol	1.3738	1.4120	7.3667	16.34
GLY77.0	1.4269	1.4289	21.0252	64.23
GLY78.0	1.4283	1.4299	23.3679	68.22
GLY80.5	1.4318	1.4324	32.9783	79.49
GLY81.0	1.4325	1.4330	35.8749	81.89
GLY83.5	1.4361	1.4362	56.3184	92.66

[a]The taper waist is surrounded by air or 1-propanol and then surrounded by a mixture of glycerol dissolved in water GLY77.0 to GLY83.5.
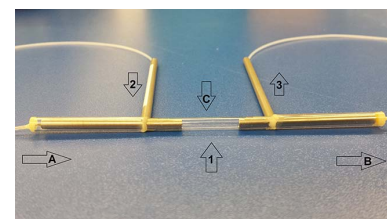
Fig. 9. Photograph of the pipeline with an inbuilt TOF sensor. (A) SMF fiber connected to the SLED source (on the left). (B) SMF connected to the detector (on the right). (C) TOF sensor. 1, protective glass tube filled with a measured liquid; 2, input of liquid; 3, output of liquid.
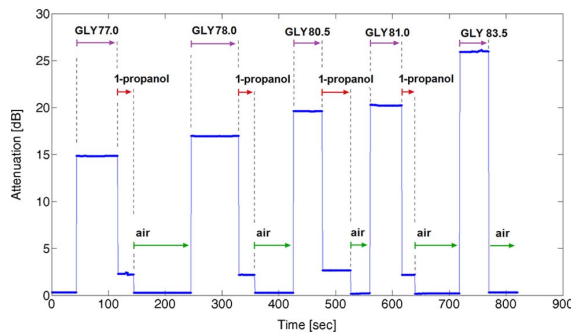
Fig. 10. Temporal changes in the attenuation of the TOF based on refractive index changes (GLY77.0 to GLY83.5). The basic reference level is represented by air and a TOF cleaning is represented by the 1-propanol level.
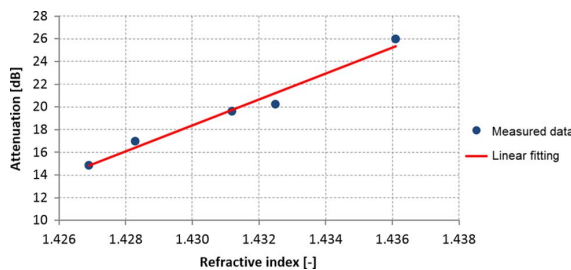
Fig. 11. Calibration curve—dependence of the attenuation on refractive index of the liquid surrounding the TOF (taper waist).

The calibration curve—dependence of attenuation on refractive index changes of the TOF—is shown in Fig. 11 and demonstrates how increasing attenuation for increasing refractive indices of the liquid analyte can be described by the linear dependence over the total measured interval of refractive indices. Please note, for a considerably wider RI range, the linearity of the calibration curve slightly decreases.

Sensitivity S of the TOF was determined mathematically from the slope of the linearly fitted calibration curve (see Fig. 11), and the correlation index R for this curve was calculated using the equation

$$R(X, Y) = \frac{\sum (x - \bar{x})(y - \bar{y})}{\sqrt{\sum (x - \bar{x})^2 \sum (y - \bar{y})^2}}, \qquad (2)$$

where $\bar{x}$ and $\bar{y}$ are the mean values of fitted sample points on the x axis and the y axis, respectively.

Sensitivity S was calculated as

$$S = \frac{dY}{dX}. \qquad (3)$$

Resulting values of the sensitivity and correlation index in the case of the TOF are $R = 0.9901$ and $S = 1143.2$ dB/RIU, respectively.

A LOD was determined from the noise level and sensitivity S, which is defined by the following equation:

$$LOD = \frac{3 \cdot \text{noise}}{\text{sensitivity}} = \frac{3 \cdot \frac{y + \Delta y}{y}}{S}. \qquad (4)$$

LOD was calculated to reach 0.0026 RIU by using Fig. 11 and Eq. (4).

B. SC MOF Simulations and Measurements

The designed structure of the SC MOF was numerically analyzed using COMSOL Multiphysics, version 5.0, simulation software. Fundamental core mode intensity profiles of the SC MOF were calculated by using the FEM technique at a wavelength of 1550 nm. The calculated effective mode index (n_{eff}), effective area (A_{eff}), and powers within the evanescent wave in cladding holes of the SC MOF filled by air, 1-propanol, or by GLY77.0 to GLY83.5 (power in analyte) are presented in Table 3.

Numerical analyses show that an overlap of the evanescent wave (the power carried by the evanescent wave in the cladding holes) for the reference measurement, with cladding holes of the SC MOF filled by 1-propanol, is almost nine times higher than the overlap of an evanescent wave for cladding holes of the SC MOF filled by air; see Table 3.

The power in the cladding holes (evanescent wave overlap in cladding holes) filled by GLY83.5 is 1.5 times higher than the power in the cladding holes filled by GLY77.0 and 5.3 times higher than 1-propanol (reference). The calculated effective areas (A_{eff}) for GLY80.5 and GLY81.0 have high confinement losses, and GLY83.5 has exceedingly high confinement loss. A selected Visualization 1 of the results of these calculations, at 1550 nm for the SC MOF cladding holes filled by air ($n = 1.0002$), 1-propanol ($n = 1.3738$), and filled by GLY77.0 ($n = 1.4269$) and GLY83.5 ($n = 1.4361$), is shown in Fig. 12.

Light coupled into the SC MOF is strongly guided into the core of the fiber thanks to the high difference in the refractive index between the core material and the air-filled cladding holes. It implies that the overlap of an evanescent wave and the sensitivity of the SC MOF is minimal; see Fig. 12(a). When cladding holes are filled by a liquid analyte, whose refractive index is not dissimilar to the refractive index of the silica core, the overlap of the evanescent wave increases as does sensitivity; see Figs. 12(b)–12(d). A photograph of the longitudinal structure of the SC MOF in the area of the boundary between

Table 3. Calculated Effective Mode Index (n_{eff}), Effective Area (A_{eff}), and Optical Power Carried by an Evanescent Wave in the Cladding Holes of the SC MOF Filled by Air, 1-propanol, or by GLY77.0 to GLY83.5

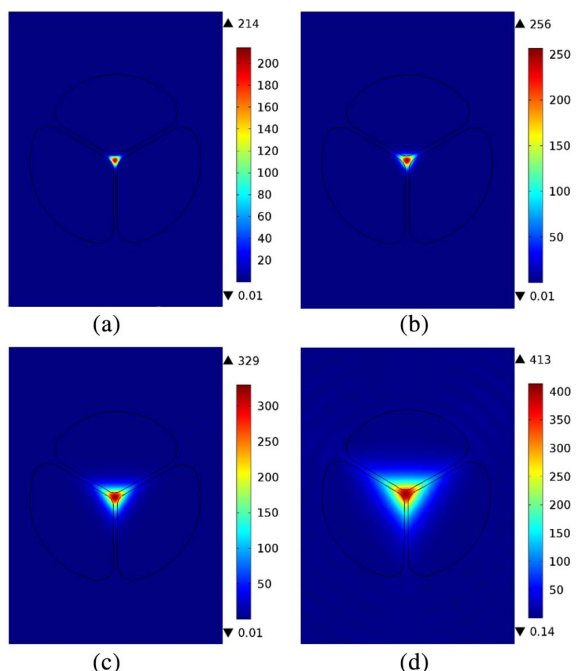| Analyte	Refractive Index [–]	n_{eff} [–]	A_{eff} [μm^2]	Power in Analyte [%]
Air	1.0002	1.4074	6.76	1.33
1-propanol	1.3738	1.4218	11.41	11.58
GLY77.0	1.4269	1.4330	33.92	40.77
GLY78.0	1.4283	1.4336	37.20	43.22
GLY80.5	1.4318	1.4353	52.91	50.25
GLY81.0	1.4325	1.4356	56.84	52.04
GLY83.5	1.4361	1.4377	Too high confinement loss	61.32

(a)   (b)

(c)   (d)

Fig. 12. Calculated fundamental, core mode normalized, intensity of electric field profiles of the SC MOF structure. The SC MOF cladding holes are filled by (a) air, (b) 1-propanol, (c) GLY77.0, and (d) GLY83.5.

air- (left) and liquid- (right) filled cladding holes is shown in Fig. 13.

The attenuation of the SC MOF was measured by the cutback method using the setup shown in Phase 1 part (a) of Fig. 7. The analyzed attenuation of the air-filled cladding holes of the SC MOF, at a wavelength of 1550 nm, was 1 dB/m. The cladding holes of the SC MOF were then filled in the 5 mm length by the reference liquid (1-propanol) and then by experimental liquid analytes GLY77.0 to GLY83.5; see Table 1. The volume of the measured liquid analyte filled in the length of 5 mm in three cladding holes of the SC MOF is approx. 13.9 nl. In this case, the attenuation of the SC MOF was measured by the cut-back method using the setup shown in Phase 2 parts (a) and (b) of Fig. 7. Cladding holes of the SC MOF were filled by measured liquid
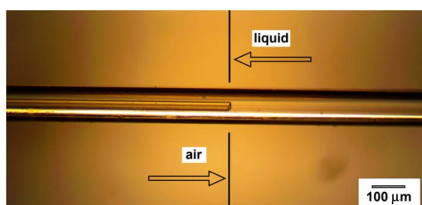

Fig. 13. Photograph of the longitudinal structure of the SC MOF in the region of the boundary between liquid-analyte- (right side) and air- (left side) filled cladding holes.
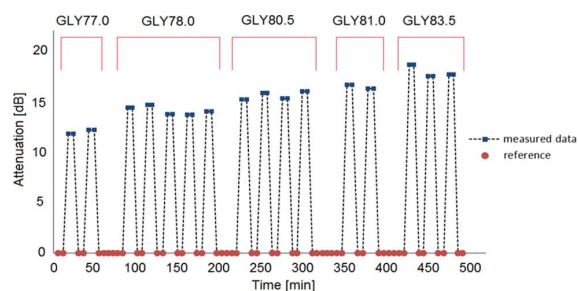

Fig. 14. Temporal changes in the attenuation of the SC MOF based on refractive index change.

analytes via capillary forces due to the relatively low viscosity of the liquid mixtures used.

Temporal changes in the attenuation of the SC MOF, based on the refractive index changes of particular mixtures (from GLY77.0 to GLY83.5), are shown in Fig. 14. Liquids of refractive indices of GLY77.0 to GLY83.5, which were used to fill the cladding holes of the SC MOF, caused changes to the refractive index of the cladding structure and induced changes in the attenuation of the guided light in the core of the SC MOF; see Fig. 14. The attenuation of each liquid was measured several times by repeatedly filling the cladding holes of the SC MOF by GLY77.0 to GLY83.5. Slight changes of attenuation for the given refractive index (GLY77.0 to GLY83.5) could be the result of different capillary forces in each cladding hole caused by a slightly different radial diameter for each hole.

A calibration curve—the dependence of the mean measured values of attenuation on the refractive index changes caused by different concentrations of GLY in water used to fill cladding holes of the SC MOF—is shown in Fig. 15 and demonstrates an increase in attenuation in correlation with higher refractive indices of the liquid analyte. The linear dependence was obtained for the total measured interval of refractive indices.

Using the calibration curve (see Fig. 15) and Eq. (3), the sensitivity S of the SC MOF was determined as 600.96 dB/RIU, and by using Eq. (2), the correlation index R was calculated to as 0.97098.

A *LOD* was calculated by using Fig. 15 and Eq. (4):

$$LOD = \frac{3 \cdot \frac{14.23+0.46}{14.23}}{600.96} = 0.0733 \ [\text{RIU}].$$
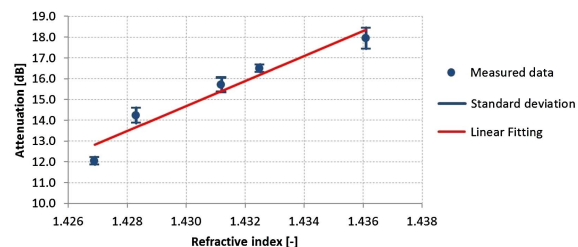

Fig. 15. Calibration curve—the dependence of the measured values of attenuation on refractive indices of SC MOF cladding holes filled with liquid.

4. DISCUSSION

The main advantage of the SC MOF is that it requires a minuscule amount of liquid analyte, specifically 27.8 nl/cm. In our case, the liquid filling length is 5.0 mm, i.e., the equivalent volume of liquid analyte in cladding holes of the SC MOF is 13.9 nl. The SC MOF measurement is more complex as the precise filling length must be controlled by a microscope examining various liquid analytes requires the SC MOF, as shown in Fig. 7 in the case of Phase 2, and to use another SC MOF section. It can be solved, e.g., by Ref. [20]. Calculations show that the effective area of the guided modes of the SC MOF, in particular for liquids from GLY 77 to GLY 83.5, is higher in comparison to the effective area of the guided modes of the TOF waist, implying that the SC MOF has a higher confinement loss, which may be explained by optical power being carried by the evanescent wave that is coupled out via the silica bridges. The measured attenuation for different refractive indices (of liquids) by the SC MOF sensor manifests small fluctuations; see Fig. 14. These measurement inaccuracies could be caused, in comparison with the TOF sensor, by manufacturing imperfections of the structural profile and symmetry of the SC MOF cladding holes. This means that each measurement of each liquid (with different viscosities) is slightly influenced by different capillary forces in each cladding hole, which affects individual filling lengths. The accuracy of measurement could also be affected by the cut-back method; a SC MOF section filled by a measured liquid is cleaved after each measurement. On the other hand, the SC MOF is mechanically more robust because the core is connected by the silica bridges to the outer silica cladding, in comparison to the TOF sensor, which is not protected by the outer cladding.

The TOF does provide a defined length of the waist (sensing area) so that the user is only required to immerse the waist of the TOF into the liquid analyte. Originally, the TOF sensor in the region of the taper waist is more fragile compared to the SC MOF. The fragility of the TOF waist is solved by the pipeline system formed by protective glass tube housing. The tube itself has the following dimensions: a length of 60 mm and an inner diameter of 2 mm, i.e., the inner volume is about 188 μl. However, the inner volume of the protective glass tube can be reduced (up to 16 times) to achieve a lower liquid sample volume and a shorter filling time for the liquid analyte. This can be achieved by inserting the TOF into a capillary fiber, which has an internal diameter >125 μm.

Both fiber optic sensors were stable during the whole measurement campaign. The fluctuation in output power during TOF testing was caused by an imperfect purification of the TOF waist surface (in the protective tube) during measurements when the liquid analytes were changed. Light coupling into the TOF was facile as the TOF is made from SMF. Light coupling into the SC MOF core area required a focusing apparatus because the core diameter was only 2.75 μm. Calculations show that the evanescent wave overlap to the liquid analyte and sensitivity of the TOF sensor is higher than the sensitivity of the SC MOF, which was confirmed by measurement.

A comparison of the price of both fiber sensors (SC MOF and TOF) is noteworthy. Current MOF fiber prices are significantly higher than an ordinary SMF, which is tapered to the desired waist diameter.

5. CONCLUSIONS

This paper focused on the application of a TOF sensor for the purposes of detecting prepared mixtures of glycerol dissolved in water to represent hazardous liquids with identical refractive indices. The new TOF principle incorporated in a pipeline system for the in-line regime of measurement was designed, characterized, and applied to liquid analyte detection. To provide a comparison of the TOF with a similar type of fiber sensor, a SC MOF featuring similar parameters to the TOF sensor was chosen. The SC MOF and TOF were tested on refractive indices in the range of 1.4269–1.4361 and at a wavelength of 1550 nm. Both fiber structures were numerically analyzed and the results of the measurements were compared.

A calculated sensitivity of $S = 600.96$ dB/RIU and a limit of detection $LOD = 0.0733$ RIU were achieved for SC MOF, whereas the TOF sensor achieved $S = 1143.2$ dB/RIU and $LOD = 0.0026$ RIU. The TOF has almost two times higher sensitivity and a 30 times higher limit of detection in comparison to the SC MOF sensor. Such differences are the result of a higher overlap of the evanescent wave to the liquid analyte (1.5 times higher power in an analyte for GLY83.5; see Tables 2 and 3) with respect to the symmetrical, cylindrical shape of the TOF waist (sensing area) when compared to the shape of the SC MOF core (sensing area). The SC MOF sensor can be used for applications where the amount of liquid is limited, as in certain medicinal or botanical situations where one-time detection is possible, and the TOF sensor can be used in applications where the amount of a liquid analyte is readily available, such as when detecting hydrocarbons in fuels or the toluene concentration in water.

REFERENCES

1. L. C. Shriver-Lake, K. A. Breslin, P. T. Charles, D. W. Conrad, J. P. Golden, and F. S. Ligler, "Detection of TNT in water using an evanescent wave fiber-optic biosensor," Anal. Chem. **67**, 2431–2435 (1995).
2. E. Musayev and S. E. Karlik, "A novel liquid level detection method and its implementation," Sens. Actuators A **109**, 21–24 (2003).
3. R. Falate, R. C. Kamikawachi, M. Müller, H. J. Kalinowski, and J. L. Fabris, "Fiber optic sensors for hydrocarbon detection," Sens. Actuators B **105**, 430–436 (2005).
4. R. Slavik, "Extremely deep long-period fiber grating made with a CO_2 laser," IEEE Photon. Technol. Lett. **18**, 1705–1707 (2006).
5. V. V. Spirin, M. G. Shlyagin, S. V. Miridonov, E. Mitrani, J. Mendieta, and A. Marquez-Lucero, "Fiber optic Bragg-grating-based sensor for liquid hydrocarbon leak detection and localization," Proc. SPIE **3986**, 292–299 (2000).
6. B. N. Shivananju, M. Renilkumar, G. R. Prashanth, S. Asokan, and M. M. Varma, "Detection limit of etched fiber Bragg grating sensors," J. Lightwave Technol. **31**, 2441–2447 (2013).

7. J. Li, H. Wang, L.-P. Sun, Y. Huang, L. Jin, and B.-O. Guan, "Etching Bragg gratings in Panda fibers for the temperature-independent refractive index sensing," Opt. Express **22**, 31917–31923 (2014).

8. K. Cherif, J. Mrazek, S. Hleli, V. Matejec, A. Abdelghani, M. Chomat, N. Jaffrezic-Renault, and I. Kasik, "Detection of aromatic hydrocarbons in air and water by using xerogel layers coated on PCS fibers excited by an inclined collimated beam," Sens. Actuators B **95**, 97–106 (2003).

9. O. S. Wolfbeis, "Fiber-optic chemical sensors and biosensors," Anal. Chem. **72**, 81–90 (2000).

10. J. D. Love, W. M. Henry, W. J. Stewart, R. J. Black, S. Lacroix, and F. Gonthier, "Tapered single-mode fibers and devices. I. Adiabaticity criteria," IEEE Proc. J. Optoelectron. **138**, 343–354 (1991).

11. J. D. Love and W. M. Henry, "Quantifying loss minimisation in single-mode fiber tapers," Electron. Lett. **22**, 912–914 (1986).

12. A. W. Snyder and J. D. Love, *Optical Waveguide Theory* (Chapman & Hall, 1983).

13. T. M. Monro, W. Belardi, K. Furusawa, J. C. Baggett, N. G. R. Broderick, and D. J. Richardson, "Sensing with microstructured optical fibres," Meas. Sci. Technol. **12**, 854–858 (2001).

14. T. Martan, J. Aubrecht, O. Podrazký, V. Matějec, and I. Kašík, "Detection of hydrocarbons using suspended core microstructured optical fiber," Sens. Actuators B **202**, 123–128 (2014).

15. H. Ebendorff-Heidepriem, S. C. Warren-Smith, and T. M. Monro, "Suspended nanowires: fabrication, design and characterization of fibers with nanoscale cores," Opt. Express **17**, 2646–2657 (2009).

16. E. Coscelli, M. Sozzi, F. Poli, D. Passaro, A. Cucinotta, S. Selleri, R. Corradini, and R. Marchelli, "Toward a highly specific DNA biosensor: PNA-modified suspended-core photonic crystal fibers," IEEE J. Sel. Top. Quantum Electron. **16**, 967–972 (2010).

17. A. S. Webb, F. Poletti, D. J. Richardson, and J. K. Sahu, "Suspended-core holey fiber for evanescent-field sensing," Opt. Eng. **46**, 010503 (2007).

18. G. Tsiminis, F. Chu, S. C. Warren-Smith, N. A. Spooner, and T. M. Monro, "Identification and quantification of explosives in nanolitre solution volumes by Raman spectroscopy in suspended core optical fibers," Sensors **13**, 13163–13177 (2013).

19. S. C. Warren-Smith, S. V. Afshar, and T. M. Monro, "Theoretical study of liquid-immersed exposed-core microstructured optical fibers for sensing," Opt. Express **16**, 9034–9045 (2008).

20. S. Warren-Smith, H. Ebendorff-Heidepriem, T. Foo, R. Moore, C. Davis, and T. Monro, "Exposed-core microstructured optical fibers for real-time fluorescence sensing," Opt. Express **17**, 18533–18542 (2009).

21. C. J. S. de Matos, C. M. B. Cordeiro, E. M. dos Santos, J. S. K. Ong, A. Bozolan, and C. H. Brito Cruz, "Liquid-core, liquid-cladding photonic crystal fibers," Opt. Express **15**, 11207–11212 (2007).

22. N. Luan and J. Yao, "Surface plasmon resonance sensor based on exposed-core microstructured optical fiber placed with a silver wire," IEEE Photon. J. **8**, 4800508 (2016).

23. A. R. Hawkins and H. Schmidt, *Handbook of Optofluidics* (CRC Press/Taylor & Francis, 2010).

24. A. Mendez and T. Morse, *Specialty Optical Fibers Handbook* (Academic/Elsevier, 2007).

25. H. Latifi, M. I. Zibaii, S. M. Hosseini, and P. Jorge, "Nonadiabatic tapered optical fiber for biosensor applications," Photon. Sens. **2**, 340–356 (2012).

26. R. J. Black, S. Lacroix, F. Gonthier, and J. D. Love, "Tapered single-mode fibers and devices. II: experimental and theoretical quantification," IEEE Proc. J. Optoelectron. **138**, 355–364 (1991).

27. S. Pricking and H. Giessen, "Tapering fibers with complex shape," Opt. Express **18**, 3426–3437 (2010).

28. T. Vo-Dinh and C. P. Kasili, "Fiber-optic nanosensors for single-cell monitoring," Anal. Bioanal. Chem. **382**, 918–925 (2005).

29. K. Q. Kieu and M. Mansuripur, "Biconical fiber taper sensor," IEEE Photon. Technol. Lett. **18**, 2239–2241 (2006).

30. T. Vo-Dinh and Y. Zhang, "Single-cell monitoring using fiberoptic nanosensors," WIREs Nanomed. Nanobiotechnol. **3**, 79–85 (2011).

31. M. D. Marazuela and M. C. Moreno-Bondi, "Fiber-optic biosensors–an overview," Anal. Bioanal. Chem. **372**, 664–682 (2002).

32. A. M. Valadez, C. A. Lana, S. I. Tu, M. T. Morgan, and A. K. Bhunia, "Evanescent wave fiber optic biosensor for salmonella detection in food," Sensors **9**, 5810–5824 (2009).

33. I. Kasik, O. Podrazky, J. Mrazek, T. Martan, V. Matejec, K. Hoyerova, and M. Kaminek, "*In vivo* optical detection of pH in microscopic tissue samples of *Arabidopsis thaliana*," Mater. Sci. Eng. C **33**, 4809–4815 (2013).

34. http://www.sigmaaldrich.com/MSDS/MSDS/DisplayMSDSPage.do?country=CZ&language=EN-generic&productNumber=G9012&brand=SIAL&PageToGoToURL=http%3A%2F%2Fwww.sigmaaldrich.com%2Fcatalog%2Fproduct%2Fsial%2Fg9012%3Flang%3Den.

35. M. Born and E. Wolf, *Principles of Optics* (Pergamon, 1980).

36. http://refractiveindex.info/?shelf=organic&book=propanol&page=Moutzouris.
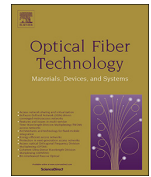
4.7   Experimentally and analytically derived generalized model for the detection of liquids with suspended-core optical fibers

This chapter is a version of the published manuscript:

[J7]: T. Nemecek, M. Komanec, B. Nelsen, T. Martan, D. Suslov, P. Hartmann, and S. Zvanovec, "Experimentally and analytically derived generalized model for the detection of liquids with suspended-core optical fibers", OPTICAL FIBER TECHNOLOGY, vol. 45, pp. 295-299, 2018.

Relevance to my Ph.D. thesis:

In previous chapters, it was proven, that an SC-MOF could be used as a liquid analyte sensor which combines many advantages, such as high sensitivity, small volume detection, use in explosive environment etc. Due to SC-MOF modifiable structure, SC-MOF can be adapted to various liquid analytes and can be designed for a wide scale of sensitivities. To create a universal tool for such sensor design and to provide more detailed sensor description, a more complex sensor investigation of variable design parameters is necessary. An analytical description of optical signal behavior, propagating inside a liquid-filled SC-MOF, has been derived in this paper. Secondly, this description was used to determine SC-MOF sensor parameters. Based on a large amount of measured data, I have derived a generalized model which describes SC-MOF sensor behavior. The generalized model could serve for SC-MOF sensor design predicting sensor parameters, such as sensitivity, resolution and dynamic range. The model can help to find an effective sensor design based on requested liquid analytes. The model outputs, in terms of sensitivity and dynamic range, can be used for a broad range of liquid analytes 1.35 – 1.42, filling lengths from 0.6 to 4.5 cm and for SC-MOF core diameters in the range from 2.4 up to 4.0 μm.

Experimentally and analytically derived generalized model for the detection of liquids with suspended-core optical fibers

Tomas Nemecek[a],[*], Matej Komanec[a], Bryan Nelsen[b],[c], Tomas Martan[a], Dmytro Suslov[a], Peter Hartmann[b],[c], Stanislav Zvanovec[a]

[a] *Department of Electromagnetic Field, Faculty of Electrical Engineering, Czech Technical University in Prague, Technicka 2, Prague 6 166 27, Czech Republic*
[b] *Fraunhofer-Institut für Werkstoff- und Strahltechnik IWS, 01277 Dresden, Germany*
[c] *Institute of Leupold-Institute for Applied Natural Sciences/Optical Technologies, University of Applied Sciences Zwickau, 08056 Zwickau, Germany*

ABSTRACT

A generalized model for the detection of liquids within suspended-core microstructured optical fibers has been experimentally and theoretically derived. The sensor detection is based on the refractometric principle of transmission losses due to the overlap of the evanescent field with the liquid analyte. A number of parameters, including fiber core diameter and filling length, have been included in the general model. Specially tailored suspended-core fibers were manufactured with the core diameters within the range of $2.4\,\mu m$ to $4.0\,\mu m$. Five selected liquid analytes were used to cover the refractive index range of 1.35 to 1.42. Based on experiments, the characteristics of the parameters of the semi-empirical model have been determined by a genetic algorithm using 283 measurement data sets. The model can be used to design sensors for the detection of liquid analytes as it provides a set of parameters allowing to optimize the sensor's sensitivity for a wide scale of applications. Finally, numerical simulations of the system were carried out by an eigenmode routine to support the results of the generalized model.

1. Introduction

Remote monitoring of the quality of liquids in toxic, explosive or flammable environments is essential for safety and is required in various industrial and agricultural processes. Fiber-optic sensors provide many advantages over electronic sensors, including their small size and low weight, their immunity to electromagnetic interference, the absence of any sparks, their long lifetime and easy system integration.

To enhance fiber-optic sensor features, especially sensitivity and resolution, special optical fiber designs have been developed employing microstructured optical fibers (MOFs) [1,2]. The potential of MOFs for optical detection lies in the possibility of tailoring the MOF structure to achieve enhanced sensor performance [3]. Among MOFs, suspended-core MOFs (SC-MOFs) can provide significantly increased evanescent field overlap with the measured analyte, making them exceptionally suitable for the purposes of the detection of liquid analytes. An overview of SC-MOF sensor applications is summarized in [4,5]. SC-MOF sensors focusing on specific liquid analytes or in-liquid particles were developed using plasmon resonance [6,7] and other spectroscopic sensing methods [8]. Even though the abovementioned SC-MOF sensors provide high sensitivity, they require a complex multi-step sensor preparation, often including opto-chemical transducers.

Refractive index-based sensors represent a simplified and universal sensor approach for the detection of liquid analytes, e.g. in petrol quality analysis, where the refractive index of gasoline change as a result of blending with bioalcohol was studied in [9] and similarly ethanol-gasoline concentration was measured by long-period gratings in [10]. Several SC-MOF structural modifications for the detection of liquid analytes have been previously presented as an exposed-core fiber [11,12]. Conventional and selective hole filling of SC-MOF was also examined [13,14]. The combination of fiber Bragg gratings and SC-MOF was presented in [15], where the achieved sensitivity was up to $100\,nm/RIU$. Resonance based RI sensing was demonstrated by MOF tapering, resulting in air-hole collapse [16], where the resolution acquired by this approach was around 1×10^{-5} RIU. An interference-based sensor, consisting of two air-clad MOFs spliced between standard single-mode fibers, was presented in [17], indicated sensitivity was $230\,nm/RIU$ and achieving resolution of 3.4×10^{-5} RIU.

This paper significantly extends our previous work [18] by developing an analytical description of optical signal propagation within a liquid analyte filled SC-MOF. Based on an extensive amount of experimental data, a generalized model is derived, which describes the
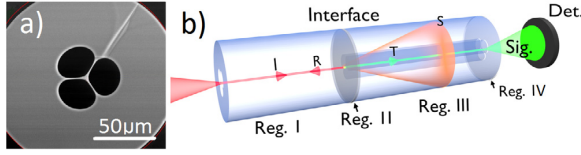

Fig. 1. a) Scanning-electron microscope (SEM) image of the end-face of a 4 μm core diameter SC-MOF and b) a schematic representation the studied interactions inside the SC-MOF studied; Det – Detector, Sig – Signal, I – Incident, R – Reflected, T – Transmitted and S – Scattered light. Region I – air-filled cladding holes, Region II – air-clad liquid-clad interface, Region III – liquid-filled cladding holes, Region IV – liquid-filled cladding free-space interface.

theoretical and empirical behavior of the SC-MOF sensor. This model can be used as a universal tool for SC-MOF sensor design.

2. Light propagation in SC-MOF structure

The mechanisms which cause losses in a partially liquid-filled SC-MOF (shown in Fig. 1) can be divided into two essential loss contributions. The major loss sources are illustrated in Fig. 1 b). The first of them is represented by reflection and scattering losses at the boundary where the air-filled cladding (depicted as Region I) interfaces the liquid-filled cladding (depicted as Region II), as well as in the case of the interface of liquid-filled cladding (depicted as Region III) and free-space at the end of the SC-MOF (depicted as Region IV). Region IV further represents radiation from the SC-MOF end-face. The second type of loss is caused by the evanescent component of the SC-MOF mode being either absorbed or scattered by the liquid analyte itself (Region III).

A numerical-based solution of the losses in the liquid-filled SC-MOF was carried out by a self-developed eigenmode routine using a finite-difference method with a sparse-matrix eigenvalue solver which we utilized to solve the propagation of modes in both the air- and liquid-filled sections of the SC-MOF sensor (Region I and Region III). It was important to consider the full-polarization form of the wave equation because the tight confinement of the modes depends strongly on the boundary conditions between glass and air, or, glass and the liquid analyte (previously defined in [18]). A set of first-order polarized guided modes derived for SC-MOF, with a core diameter (d_{core}) of 4 μm, is shown in Fig. 2.

It was assumed, for the purpose of simplicity, that only the fundamental mode is excited in Region I. The model can be written as:

$$\overrightarrow{E_{III}} = a_0 \overrightarrow{E_O} + \overrightarrow{E_s}, \tag{1}$$

where $\overrightarrow{E_s}$ is light scattered at the interface, $\overrightarrow{E_0}$ is the normalized fundamental mode electric field in Region III and $|a_0|^2$ gives the fraction of power coupled into the outgoing fundamental mode [19], used as the input field for Region III. It is assumed that the remaining power $(1-|a_0|^2)$ is scattered into the cladding modes and mostly lost due to scattering out of SC-MOF. The power, therefore, transferred to the fundamental mode of Region III at the interface (Region II) is given by:
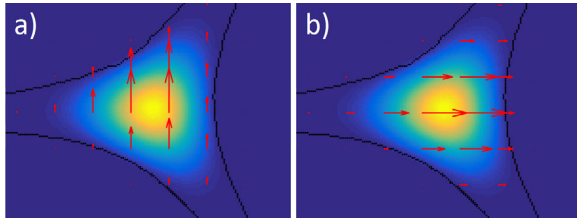

Fig. 2. Numerically calculated polarized fundamental modes of the SC-MOF with a 4 μm core diameter at 1550 nm. a) and b) are orthogonal to each other, $\beta = 5.788 \, \mu m^{-1}$.
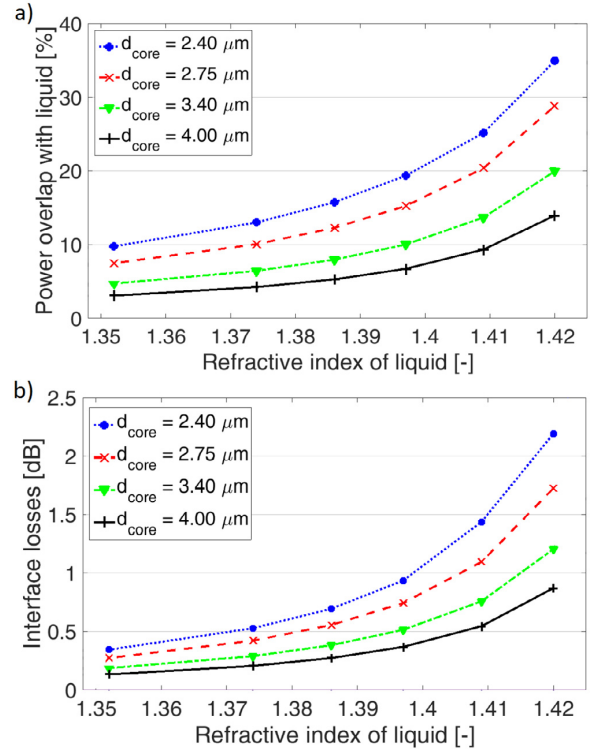

Fig. 3. Finite difference results of a) the power overlap with liquid analytes with respect to SC-MOF core diameters for Region III (see Eq. (1)) and b) losses due to reflection and scattering at the interface (Eq. (2)).

$$P_{III} = |a_0|^2 P_I, \tag{2}$$

with P_I, P_{III} being the power in Regions I and III, respectively (reflection at this interface was calculated to be extremely small because the mode in Region I is very tightly confined in the glass core of the SC-MOF). Once the light has entered Region III, the liquid analyte gives rise to both absorption losses and weak scattering losses. Both loss coefficients are proportional to the distance traveled through the liquid analyte and the power overlap of the fundamental mode with the liquid analyte. The differential power loss in Region III can be expressed as:

$$\frac{\partial P}{\partial z} = -(\rho_a \sigma_{abs} + \rho_s \sigma_{scatt})\eta P, \tag{3}$$

where P is the power along the length of SC-MOF, σ_{abs}, σ_{scatt} are the absorption and scattering cross-sections, respectively, ρ_a and ρ_s are the density of absorbing and scattering centers in the liquid analyte, respectively, and η is the percentage of mode intensity overlap with the liquid analyte. The derived dependencies of power overlapping with liquid and interface losses on RI and core diameter are shown in Fig. 3. The solution to Eq. (3), considering the full length of the liquid-filled section, can be written as:

$$P = P_{III} e^{-(\rho_a \sigma_{abs} + \rho_s \sigma_{scatt})\eta l_{fill}}, \tag{4}$$

where l_{fill} is the length of liquid-filled SC-MOF, and P_{III} stands for the power at the input interface of Region III.

The losses in Region IV do not change significantly from the completely unfilled SC-MOF to the filled case. Since the losses of the filled SC-MOF will be calculated relative to that of the completely unfilled SC-MOF, losses due to Region IV are not included in the final equation.

Finally, inserting Eq. (2) into Eq. (4), the attenuation caused by liquid analyte in the SC-MOF sensor can be determined in [dB] by:
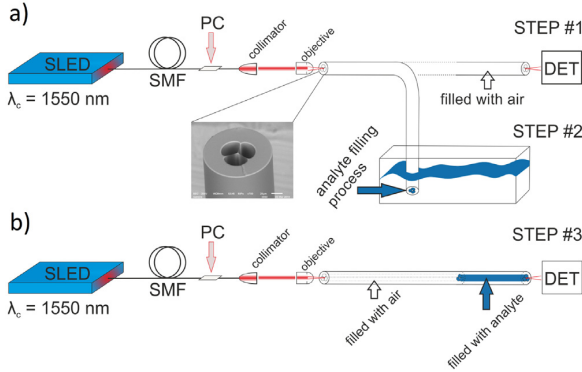
T. Nemecek et al.

Fig. 4. Scheme of the measurement setup using SC-MOF for detection of liquid analytes, a) Step 1 – reference measurement, followed by Step 2 – SC-MOF filling process, b) Step 3 – liquid analyte measurement process. SMF – single mode fiber, PC – polarization controller, DET – detector.

$$L_{att} = 10log_{10}(e)((\rho_a\sigma_{abs} + \rho_s\sigma_{scatt})\eta l_{fill} - ln|a_0|^2). \qquad (5)$$

3. Analyte measurements

To derive a generalized model of the SC-MOF sensor, an extensive measurement campaign has been performed. In our measurement setup (see Fig. 4), a super-luminescent LED (SLED) diode centered at a wavelength of 1545 nm with a 40 nm full-width at half-maximum intensity distribution was used. The polarization of the SLED output was adjusted by a polarization controller (PC), collimated by a GRIN collimator and, subsequently, focused via an objective (with a 40x magnification and a numerical aperture of NA = 0.60) into the selected silica SC-MOF (RI at 1545 nm is 1.441). The detector was a Ge-based photodiode with a sensitivity level of 50 nW. SC-MOFs were filled with selected liquid analytes and the filling length was monitored with a digital microscope, which allowed us to achieve a filling-length precision better than 20 μm.

To cover a wide range of liquid analyte RIs, we prepared liquid analytes: Ethyl-alcohol (RI = 1.3520) and mixtures of Isopropyl-alcohol and Ethylene-glycol (EG) (with RI = 1.3861, 1.3970, 1.4085 and 1.4204 at EG concentrations by volume of 25%, 50%, 75% and 100%, respectively). All RI data assumes a wavelength of 1545 nm. Each liquid analyte was used to characterize the performance of each SC-MOF sample with inner core diameters of 2.40, 2.75, 3.40, and 4.00 μm. Clading outer diameter ranged from 108 μm to 157 μm. In each measurement step (see Fig. 4) the reference power was first measured with the air-filled SC-MOF (Step 1). Subsequently, a defined length of the SC-MOF was filled with a liquid analyte via capillary forces (Step 2). Filling lengths ranged from 0 cm to 4.5 cm (the upper limit was set by the dynamic range of the measurement setup). We measured each liquid analyte three times within the above-mentioned Steps 1–3. The temperature was kept constant within the range of ±1 °C during the measurement to eliminate RI drifts of the liquid analytes. Fundamental-mode excitation was optimized by near-field measurements of the guided light within SC-MOF.

The measured dependencies of attenuation (L_{att}) of an SC-MOF sensor (determined as the difference from the reference measurement) with a core diameter of 3.40 μm for the range of tested liquid analytes and different filling lengths are illustrated in Fig. 5 a). Note that the slope of the curve is linear in the case of filling lengths ranging from 0.5 cm up to 4.5 cm. This is in contrast to shorter filling lengths where the scattered light from the air-to-liquid interface (illustrated in Fig. 1 b) still has a significant intensity at the point it reaches the detector.
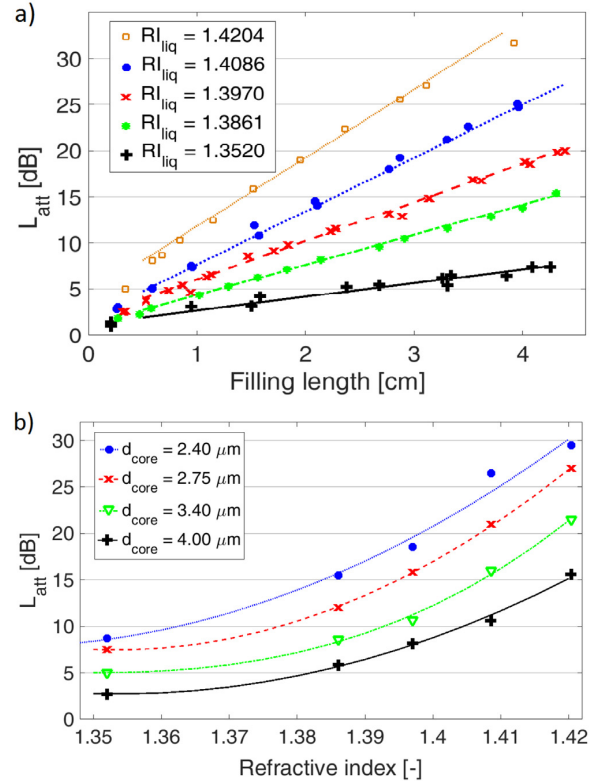

Fig. 5. Measured dependencies of SC-MOF sensor attenuation on a) filling length for SC-MOF with a core diameter of 3.40 μm, b) RIs of liquid analytes and SC-MOF core diameters when filling length = 2.5 cm.

4. Generalized model

Parameters generated by the numerical model require a large computational effort to determine a detailed description of a specific sensor system, thus we have derived a generalized model of a SC-MOF sensor for the detection of liquid analytes based on experimental data and validated by simulation. The performance of the SC-MOF sensor can be determined in relation to L_{att} caused by the: i) dependence on the filling length (l_{fill} ranging from 0.5 cm to 4.5 cm); ii) dependence on the RI of the liquid analyte (RI_{liq} from 1.35 to 1.42); and iii) dependence on the power overlap in the liquid analyte corresponding to the core diameter (from 2.4 μm to 4.0 μm). The following generalized model of overall sensor attenuation has been derived based on Eq. (5) and the measured data:

$$L_{att}(l_{fill}, RI_{liq}, d_{core}) = l_{fill} \times c_1(RI_{liq}, d_{core}) + c_2(RI_{liq}, d_{core}), \qquad (6)$$

where c_1 and c_2 are experimentally derived coefficients dependent on RI_{liq} and d_{core} based on 283 measurements. While the coefficient c_1 represents attenuation in the liquid-filled SC-MOF (Region III), c_2 is then influenced by conditions on the interface between the air and the liquid-filled cladding holes (Region II, IV) corresponding to the scattering and reflection of the optical signal. The dependencies of the coefficients c_1 and c_2 have been empirically determined, see the visualization with respect to RI_{liq} and d_{core} in Fig. 6.

The general description of c_1 [dB/cm] and c_2 [dB] dependencies has been derived utilizing a genetic algorithm [20] on the experimentally collected data. A population of 10^6 generations was used to obtain a precise solution. The following dependencies have been derived using the genetic algorithm:
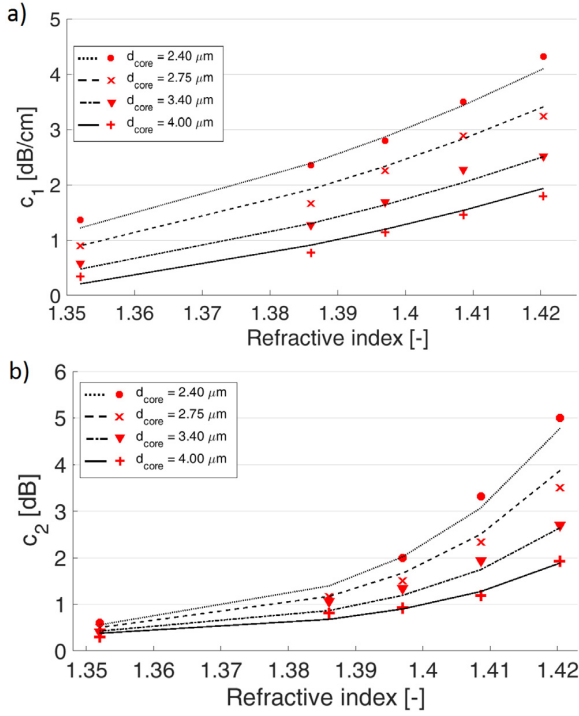
Fig. 6. Coefficient evolution of analyzed SC-MOF. a) c_1 values, b) c_2 values from measurements (symbols) and curves calculated from the generalized model (lines).

$$c_1 = a_1 \times \left(\left(1 + \frac{a_2}{d_{core}} \right) \right) \times (e^{(a_3(RI_{liq}-1))}-1), \tag{7}$$

$$c_2 = e^{\left(b_1 + \left(\frac{b_2}{d_{core}} \right) \right)} \times (e^{(b_3(RI_{liq}-1))}-1), \tag{8}$$

values of the variables are summarized in Table 1. The results of these equations are plotted as lines on top of the measured data points shown in Fig. 6 a) and b). Fig. 6 a) is the same as the theoretically derived Fig. 3 a) up to an overall, analyte-dependant proportionality constant (this constant is seen in the first term of Eq. (5)), whereas, Figs. 6 b) and 3 b) are comparable and represent interface losses.

The standard deviation of the generalized model is below 0.9 dB over the entire studied RI range. Sensor resolution, based on experimental data, is better than 10^{-4} RI over the whole RI range 1.35 to 1.42 and SC-MOF core diameter from 2.4 µm up to 4 µm.

The utilization of the derived model can be illustrated in the following example of the design of a sensor for Ethylene-glycol (i.e., antifreeze) monitoring. The desired detection RI ranges from RI = 1.3861 to 1.4204 representing water-diluted Ethylene-glycol and pure Ethylene-glycol, respectively. For the purposes of this example, we assume that a standard source/detector deployment limits the measurement setup up to the maximum dynamic range of 20 dB. The main aim is to design a sensor with the highest sensitivity. Based on the input

Table 1
Derived variables for determination of c_1 (Eq. 7) and c_2 (Eq. 8), with losses measured in decibels.

Variables for c_1		Variables for c_2	
a_1 [1/cm]	−0.0027	b_1 [−]	−14.9012
a_2 [µm]	−7.3708	b_2 [µm]	5.0225
a_3 [−]	18.0144	b_3 [−]	34.1974

Table 2
Example of sensor design based on a constant dynamic range of 20 dB for Ethylene–glycol monitoring.

SC-MOF		
Core size [µm]	Filling length [cm]	Sensitivity [dB/RIU]
2.5	1.77	334.1
3.0	2.32	375.7
3.5	3.01	411.3
4.0	3.92	441.8

limits, the model proposes a set of SC-MOFs of various core diameters. For each core diameter the maximum filling length is limited by the maximum dynamic range. Final solutions of the sensor are summarized in Table 2, where the sensitivity S is determined as:

$$S = \frac{\Delta L_{att}}{\Delta RI_{liq}} \tag{9}$$

The highest sensitivity, based on data from the derived model, can be reached in this case for an SC-MOF of 4 µm core diameter and a filling length of 3.92 cm.

For this specific situation, more options can be generated by the model, which mainly provides the sensitivity evaluation of the SC-MOF sensor and also the possibility of an application-tailored approach. Generally, a larger core diameter would be preferred to provide higher coupling efficiency and longer filling length to increase the sensitivity.

5. Conclusions

The semi-empirical generalized model of SC-MOF for the detection of liquid analytes has been derived. The model serves as a universal tool for a specific sensor design given a wide scale of input parameters such as refractive index range, dynamic range or minimal sensitivity requirements. The generalized model is based on an immense experimental data set, which also eliminated the need for the computationally expensive eigenvalue routine which still requires additional input parameters such as the scattering and absorption cross sections of the analyte. We carried out 283 measurements of SC-MOFs with core diameters in the range of 2.4 µm to 4.0 µm, and with liquid analyte refractive index in the range of 1.35 to 1.42. A genetic algorithm was applied to find a simplified general description of sensor behavior over a wide range of SC-MOF parameters.

Using the genetic algorithm, we found two key coefficients to describe the sensor. The first coefficient represents optical signal attenuation in the liquid analyte, while the second represents signal loss at the air-analyte interface. These results are in strong correlation with the analytical description based on the numerical solutions, where a developed theoretical approach has been applied to describe the complete system performance using an eigenmode solver. The standard deviation of the semi-empirical model is below 0.9 dB for the entire refractive index range and the whole scale of SC-MOF parameters that we investigated. The resolution and sensitivity of the proposed SC-MOF sensors are more than sufficient for detection of a broad range of liquid analytes, e.g. petrol quality analysis in Ethylene-glycol and gasoline blends monitoring.

Appendix A. Supplementary data

Supplementary data associated with this article can be found, in the

online version, at https://doi.org/10.1016/j.yofte.2018.08.005.

References

[1] A.M. Cubillas, S. Unterkofler, et al., Photonic crystal fibres for chemical sensing and photochemistry, Chem. Soc Rev. 42 (22) (2013) 8629–8648.

[2] M. Calcerrada, C. Garcia-Ruiz, M. Herraez, Chemical and biochemical sensing applications of microstructured optical fiber-based systems, Laser Photonics Rev. 9 (6) (2015) 604–627.

[3] R. Kostecki, H. Ebendorff-Heidepriem, S.C. Warren-Smith, T.M. Monro, Predicting the drawing conditions for microstructured optical fiber fabrication, Opt. Mat. Exp. 4 (2014) 29–40.

[4] O. Frazao, et al., Suspended-core fibers for sensing applications, Phot. Sens. 2 (2) (2012) 118–126.

[5] T.M. Monro, et al., Sensing with suspended-core optical fibers, Opt. Fiber Tech. 16 (2010) 343–356.

[6] Y. Zhao, D. Ze-qun, J. Li, Photonic crystal fiber based surface plasmon resonance chemical sensors, Sens. Actuators B: Chem. 202 (2014) 557–567.

[7] J.P.B. Lee, S. Roh, Current status of micro- and nano-structured optical fiber sensors, Opt. Fiber Technol. (2009) 209–221.

[8] T.G. Euser, J.S.Y. Chen, M. Scharrer, P.S.J. Russell, N.J. Farrer, P.J. Sadler, Quantitative broadband chemical sensing in airsuspended solid-core fibers, Appl. Phys. 103 (1) (2008) 103108.

[9] I. Nita, E. Geacai, S.O.O. Iulian, Study of the refractive index of gasoline + alcohol pseudo-binary mixtures, Ovidius Univ. Ann. Chem. (2017) 18–24.

[10] G.R.C. Possetti, M. Muller, J.L. Fabris, Refractometric optical fiber sensor for measurement of ethanol concentration in ethanol-gasoline blend, Int. Microwave Optoelectron. Conf. (2009) 616–620.

[11] C. Warren-Smith, H. Ebendorff-Heidepriem, et al., Exposed-core microstructured optical fibers for real-time fluorescence sensing, Opt. Exp. 17 (2009) 18533–18542.

[12] R. Kostecki, H. Ebendorff-Heidepriem, et al., Silica exposed-core microstructured optical fibers, Opt. Mater. Expr. 2 (11) (2012) 1538–1547.

[13] C.M.B. Cordeiro, E.M. dos Santos, C.H.B. Cruz, D. Ferreira, Lateral access to the holes of photonic crystal fibers – selective filling and sensing applications, Opt. Exp. 14 (18) (2006) 8403–8412.

[14] Y.P. Wang, S.J. Liu, X.L. Tan, W. Jin, Selective-fluid-filling technique of microstructured optical fibers, J. Lightwave Techol. 28 (22) (2010) 3193–3196.

[15] S.C. Warren-Smith, T. Monro, Exposed core microstructured optical fiber bragg gratings: refractive index sensing, Opt. Exp. 22 (2) (2014) 1480–1489.

[16] V.P. Minkovich, J. Villatoro, et al., Holey fiber tapers with resonance transmission for high-resolution refractive index sensing, Opt. Exp. 13 (19) (2005) 7609–7614.

[17] S. Silva, J.L. Santos, F.X. Malcata, J. Kobelke, K. Schuster, O. Frazao, Optical refractometer based on large-core air-clad photonic crystal fibers, Opt. Lett. 36 (6) (2011) 852–854.

[18] T. Nemecek, M. Komanec, M. Martan, R. Ahmad, S. Zvanovec, Suspended-core microstructured fiber for refractometric detection of liquids, Appl. Opt. 54 (30) (2015) 8899–8903.

[19] K. Kataoka, Estimation of coupling efficiency of optical fiber by far-field method, Opt. Rev. 17 (5) (2010) 476–480.

[20] S.M. Lothar, Theory of genetic algorithms, Theor. Comput. Sci. 259 (2001) 1–61.

5.   Conclusion

This thesis provided detailed insight into the approaches and methods of liquid analyte detection techniques based on specialty optical fibers. The state of the art was presented with an emphasis on the refractometric approach, especially for the detection of liquid analytes.

An analytical study of multi-mode coreless optical fibers was carried out [J1] with an emphasis on the role of particular higher-order modes with respect to their sensitivity for liquid analyte detection. With selective higher-order mode excitation the overall sensor sensitivity was significantly increased. An experimental study of the pre-calculated fiber has been carried out and theoretical results were verified.

In our specialty optical fiber based sensor approach [J2] we used the refractometric method in combination with the tapering of MM optical fibers. The tapering process has been mastered, over 200 TOF sensor samples have been prepared, with minimized TOF waist diameter deviations below 0.25 μm. Sensitivity curve for selected fiber types, with respect to their TOF waists, was presented and saturation points of sensitivity have been determined, for the first time. These saturation points provide an important limitation of effective TOF waist diameter for particular MM fibers. Sensitivity over 200%/RIU has been reached in an RI range of 1.352 up to 1.426.

Then, surface structural modification of single-mode TOFs has been presented for the first time [J3] as a part of the TOF preparation process. The structural modification occured when the TOF was exposed to hygroscopic liquid analytes. A 12-month long-term test, as well as proof-of-principle tests, have been performed. Almost ten times higher sensitivity has been achieved based on the surface structural modification of up to 2100 dB/RIU while keeping good sensor stability and still providing a linear response of the proposed single-mode TOF sensor.

To increase robustness and to allow sensor customization, a new refractometric technique based on an SC-MOF has been developed for the detection of liquid analytes [J4]. Broad range of liquid analytes can be measured and an inner SC-MOF structure can be designed to optimize sensor performance in terms of sensitivity, resolution and dynamic range, with respect to the selected liquid analyte. Simulations of mode field distribution and sensitivity of the proposed SC-MOF sensor have been carried out and subsequently verified by measurements. An SC-MOF sensor, with core size of 2.75 μm, has been studied to analyze liquid analytes in the RI range from 1.352 up to 1.426. High sensitivity has been achieved by only requiring a few tenths of nanoliters of the liquid analyte.

To further evaluate the benefits of the SC-MOF and TOF sensors, they were compared

with a semi-ellipsoidal sensing element in [J5]. Furthermore, to evaluate TOF and SC-MOF sensors in more detail, theoretical and experimental comparison was presented [J6]. Method that incorporates TOF and SC MOF of small core (waist) diameter for refractometric detection is presented. Benefits and drawbacks, with respect to their further application, have been summarized and evaluated.

Finally, to fully characterize the newly developed SC-MOF detection technique, the universal methodology for the utilization of SC-MOFs has been derived [J7]. A theoretical description of SC-MOF sensors filled with liquid analyte has been presented. Based on almost 300 measurements, the generalized model has been derived which involves different core-size SC-MOFs, filling lengths and liquid analytes. The model can be used as a universal tool for SC-MOF sensor design. Using this generalized model, SC-MOF sensor parameters, like sensitivity, resolution and dynamic range, can be predicted. The SC-MOF sensor can then be designed based on particular detection demands.

Therefore, based on results published in [J1-J7], the dissertation thesis goals listed in Chapter 3. have been fulfilled.

The results described in the above-mentioned papers show that there are several areas where the research can further evolve. As pointed out, multi-mode optical fibers provide the possibility of increasing sensitivity by selective higher-order mode excitation, which is a challenging task. Our TOF and SC-MOF sensors can be further analyzed in terms of stability for a wider range of analytes, with the aim of practical application. From the scientific point of view the combination of a TOF and SC-MOF sensor with the SPR method could have promising results.

References

[1] G. Rajan, *Optical Fiber Sensors: Advanced Techniques and Applications (Devices, Circuits, and Systems)*, 1 edition. Reading, Massachusetts: CRC Press, 2015.

[2] E. Udd, B. William, and J. Spillman, *Fiber Optic Sensors: An Introduction for Engineers and Scientists*, 2 edition. Wiley, 2011.

[3] G. Stewart, W. Jin, and B. Culshaw, "Prospects for fibre-optic evanescent-field gas sensors using absorption in the near-infrared", *SENSORS AND ACTUATORS B-CHEMICAL*, vol. 38, no. 1-3, pp. 42–47, Jan. 1997.

[4] S. M. Chandani and N. A. F. Jaeger, "Optical fiber-based liquid level sensor", *OPTICAL ENGINEERING*, vol. 46, no. 11, Nov. 2007.

[5] E. Sinchenko, W. E. K. Gibbs, A. P. Mazzolini, and P. R. Stoddart, "The effect of the cladding refractive index on an optical fiber evanescent-wave sensor", *JOURNAL OF LIGHTWAVE TECHNOLOGY*, vol. 31, no. 20, pp. 3251–3257, Oct. 2013.

[6] T. G. Euser, J. S. Y. Chen, M. Scharrer, P. S. J. Russell, N. J. Farrer, and P. J. Sadler, "Quantitative broadband chemical sensing in air-suspended solid-core fibers", *JOURNAL OF APPLIED PHYSICS*, vol. 103, no. 10, May 2008.

[7] V. K. Rai, "Temperature sensors and optical sensors", *APPLIED PHYSICS B*, vol. 88, no. 2, pp. 297–303, Jul. 2007.

[8] S. Wade, S. Collins, and G. Baxter, "Fluorescence intensity ratio technique for optical fiber point temperature sensing", *JOURNAL OF APPLIED PHYSICS*, vol. 94, no. 8, pp. 4743–4756, Oct. 2003.

[9] Y. Zhao, M.-Q. Chen, R.-Q. Lv, P. Wang, and X. Feng, "Small and practical optical fiber fluorescence temperature sensor", *IEEE TRANSACTIONS ON INSTRUMENTATION AND MEASUREMENT*, vol. 65, no. 10, pp. 2406–2411, Oct. 2016.

[10] O. McGaughey, J. V. Ros-Lis, A. Guckian, A. K. McEvoy, C. McDonagh, and B. D. MacCraith, "Development of a fluorescence lifetime-based sol-gel humidity sensor", *ANALYTICA CHIMICA ACTA*, vol. 570, no. 1, pp. 15–20, Jun. 2006.

[11] A. M. Valadez, C. A. Lana, S.-I. Tu, M. T. Morgan, and A. K. Bhunia, "Evanescent wave fiber optic biosensor for salmonella detection in food", *SENSORS*, vol. 9, no. 7, pp. 5810–5824, Jul. 2009.

[12] C.-S. Chu, Y.-L. Lo, and T.-W. Sung, "Review on recent developments of fluorescent oxygen and carbon dioxide optical fiber sensors", *PHOTONICS SENSORS*, vol. 1, no. 3, pp. 234–250, Sep. 2011.

[13] *Raman spectroscopy*, `http://bodyyouknow.org/raman-spectroscopy`, Accessed: 2019-11-12.

[14] M. Lewis, I. Lewis, and P. Griffiths, "Anti-stokes raman spectrometry with 1064-nm excitation: An effective instrumental approach for field detection of explosives", *APPLIED SPECTROSCOPY*, vol. 58, no. 4, pp. 420–427, Apr. 2004.

[15] T. Frosch, D. Yan, and J. Popp, "Ultrasensitive fiber enhanced uv resonance raman sensing of drugs", *ANALYTICAL CHEMISTRY*, vol. 85, no. 13, pp. 6264–6271, Jul. 2013.

[16] S. R. Khandasammy, M. A. Fikiet, E. Mistek, Y. Ahmed, L. Halamkova, J. Bueno, and I. K. Lednev, "Bloodstains, paintings, and drugs: Raman spectroscopy applications in forensic science", *FORENSIC CHEMISTRY*, vol. 8, pp. 111–133, May 2018.

[17] M. P. Buric, K. P. Chen, J. Falk, and S. D. Woodruff, "Enhanced spontaneous raman scattering and gas composition analysis using a photonic crystal fiber", *APPLIED OPTICS*, vol. 47, no. 23, pp. 4255–4261, Aug. 2008.

[18] A. P. Craig, A. S. Franca, and J. Irudayaraj, "Surface-enhanced raman spectroscopy applied to food safety", in *ANNUAL REVIEW OF FOOD SCIENCE AND TECHNOLOGY, VOL 4*, ser. Annual Review of Food Science and Technology, M. Doyle and T. Klaenhammer, Eds., vol. 4, 2013, pp. 369–380.

[19] M. M. L. Yu and P. M. L. Sandercock, "Principal component analysis and analysis of variance on the effects of entellan new on the raman spectra of fibers", *JOURNAL OF FORENSIC SCIENCES*, vol. 57, no. 1, pp. 70–74, Jan. 2012.

[20] J. Cao, E. K. Galbraith, T. Sun, and K. T. V. Grattan, "Comparison of surface plasmon resonance and localized surface plasmon resonance-based optical fibre sensors", in *Sensors & their applications XVI*, P. Kyriacou, A O'Riordan, and G McConnell, Eds., ser. Journal of Physics Conference Series, vol. 307, 2011.

[21] J. Homola, J. Ctyroky, M. Skalsky, J. Hradilova, and P. Kolarova, "A surface plasmon resonance based integrated optical sensor", *SENSORS AND ACTUATORS B-CHEMICAL*, vol. 39, no. 1-3, pp. 286–290, Mar. 1997.

[22] J. H. Ahn, T. Y. Seong, W. M. Kim, T. S. Lee, I. Kim, and K.-S. Lee, "Fiber-optic waveguide coupled surface plasmon resonance sensor", *OPTICAL EXPRESS*, vol. 20, no. 19, pp. 21 729–21 738, Sep. 2012.

[23] M.-C. Navarrete, N. Diaz-Herrera, A. Gonzalez-Cano, and O. Esteban, "Surface plasmon resonance in the visible region in sensors based on tapered optical fibers", *SENSORS AND ACTUATORS B-CHEMICAL*, vol. 190, pp. 881–885, Jan. 2014.

[24] V. V. R. Sai, T. Kundu, and S. Mukherji, "Novel u-bent fiber optic probe for localized surface plasmon resonance based biosensor", *BIOSENSORS & BIOELEC-TRONICS*, vol. 24, no. 9, pp. 2804–2809, May 2009.

[25] B. Sciacca and T. M. Monro, "Dip biosensor based on localized surface plasmon resonance at the tip of an optical fiber", *LANGMUIR*, vol. 30, no. 3, pp. 946–954, Jan. 2014.

[26] J. Boehm, A. Francois, H. Ebendorff-Heidepriem, and T. M. Monro, "Chemical deposition of silver for the fabrication of surface plasmon microstructured optical fibre sensors", *PLASMONICS*, vol. 6, no. 1, pp. 133–136, Mar. 2011.

[27] C. Caucheteur, T. Guo, and J. Albert, "Review of plasmonic fiber optic biochemical sensors: Improving the limit of detection", *ANALYTICAL AND BIOANALYTI-CAL CHEMISTRY*, vol. 407, no. 14, pp. 3883–3897, May 2015.

[28] G. V. Naik, J. Kim, and A. Boltasseva, "Oxides and nitrides as alternative plasmonic materials in the optical range [invited]", *OPTICAL MATERIALS EX-PRESS*, vol. 1, no. 6, pp. 1090–1099, Oct. 2011.

[29] P. Schiebener, J. Straub, J. Sengers, and J. Gallagher, "Refractive index of water and steam as function of wavelength, temperature and density", *JOURNAL OF PHYSICAL AND CHEMICAL REFERENCE DATA*, vol. 19, no. 3, pp. 677–717, 1990.

[30] I. Filmetrics. (2018). Refractive index database, [Online]. Available: `https://www.filmetrics.com/refractive-index-database` (visited on 10/30/2018).

[31] M. Polyanskiy. (2018). Refractiveindex.info, [Online]. Available: `https://www.filmetrics.com/refractive-index-database,urldate={2018-10-30}`.

[32] A. N. Bashkatov and E. A. Genina, "Water refractive index in dependence on temperature and wavelength: A simple approximation", ser. Proceedings of SPIE, vol. 5068, 2003, pp. 5068–5070.

[33] P. A. S. Jorge, S. O. Silva, C. Gouveia, P. Tafulo, L. Coelho, P. Caldas, D. Viegas, G. Rego, J. M. Baptista, J. L. Santos, and O. Frazao, "Fiber optic-based refractive index sensing at inesc porto", *SENSORS*, vol. 12, no. 6, pp. 8371–8389, Jun. 2012.

[34] S. O. Silva, P. Roriz, and O. Frazao, "Refractive index measurement of liquids based on microstructured optical fibers", *PHOTONICS*, vol. 1, no. 4, pp. 516–529, 2014.

[35] R. Black, S Lacrois, F Gonthier, and J. Love, "Tapered single mode fibers and devices 2, experimental and theoretical quantification", *IEEE Proceedings-j Optoelectronics*, vol. 138, no. 5, pp. 355–364, Oct. 1991.

[36] L. Tong, R. Gattass, J. Ashcom, S. He, J. Lou, M. Shen, I Maxwell, and E Mazur, "Subwavelength-diameter silica wires for low-loss optical wave guiding", *NATURE*, vol. 426, no. 6968, pp. 816–819, Dec. 2003.

[37] T. Martan, T. Nemecek, M. Komanec, R. Ahmad, and S. Zvanovec, "Refractometric detection of liquids using tapered optical fiber and suspended core microstructured fiber: A comparison of methods", *APPLIED OPTICS*, vol. 56, no. 9, pp. 2388–2396, Mar. 2017.

[38] J. C. Schlesinger, *Optical Fibers Research Advances*, 1st ed. 400 Oser Avenue, NY, 11788 USA: Nova Science Publishers, Inc., Aug. 2007.

[39] S. Huntington, J. Katsifolis, P. Moar, P. Mulvaney, A. Roberts, L. Cahill, and K. Nugent, "Evanescent field characterisation of tapered optical fibre sensors in liquid environments using near field scanning optical microscopy and atomic force microscopy", *IEE PROCEEDINGS-OPTOELECTRONICS*, vol. 146, no. 5, pp. 239–243, Oct. 1999.

[40] T. Martan, P. Honzatko, J. Kanka, and K. Novotny, "Workplace for manufacturing devices based on optical fiber tapers", in *15th Czech-Polish-Slovak conference on wave an quantum aspects of contemporary optics*, ser. Proceedings of SPIE, Czech & Slovak Soc Photon; Tech Univ Liberec, Fac Mech Engn; Agcy Act M; SPIE Czech & Slovak Chapter; Palacky Univ, Fac Nat Sci, vol. 6609, 2007.

[41] F. Bilodeau, K. Hill, S. Faucher, and D. Johnson, "Lol-loss highly overcoupled fused couples - fabrication and sensitivity to external-pressure", *JOURNAL OF LIGHTWAVE TECHNOLOGY*, vol. 6, no. 10, pp. 1476–1482, Oct. 1988.

[42] P. Pal and W. H. Knox, "Low loss fusion splicing of micron scale silica fibers", *OPTICS EXPRESS*, vol. 16, no. 15, pp. 11 568–11 573, Jul. 2008.

[43] L. Shi, X. Chen, H. Liu, Y. Chen, Z. Ye, W. Liao, and Y. Xia, "Fabrication of submicron-diameter silica fibers using electric strip heater", *OPTICAL EXPRESSS*, vol. 14, no. 12, pp. 5055–5060, Jun. 2006.

[44] C. Meng, Y. Xiao, P. Wang, L. Zhang, Y. Liu, and L. Tong, "Quantum-dot-doped polymer nanofibers for optical sensing", *ADVANCED MATERIALS*, vol. 23, no. 33, pp. 3770+, Sep. 2011.

[45]   L. Niu, C.-L. Zhao, H. Gong, Y. Li, and S. Jin, "Curvature sensor based on two cascading abrupt-tapers modal interferometer in single mode fiber", *OPTICS COMMUNICATIONS*, vol. 333, pp. 11–15, Dec. 2014.

[46]   A. Ben Khalifa, A. Ben Salem, and R. Cherif, "Fiber-optic refractive index sensor based on tapered thin core fiber", in *Photonic fiber and crystal devices: Advanced in materials and innovations in device applications XI*, S. Yin and R. Guo, Eds., ser. Proceedings of SPIE, vol. 10382, 2017.

[47]   Y. Jung, G. Brambilla, and D. J. Richardson, "Broadband single-mode operation of standard optical fibers by using a sub-wavelength optical wire filter", *OPTICAL EXPRESS*, vol. 16, no. 19, pp. 14 661–14 667, Sep. 2008.

[48]   Y. M. Kamil, M. A. Mustapa, M. H. Abu Bakar, B. Musa, A. Syahir, M. H. Yaacob, and M. A. Mahdi, "Refractive index sensor with asymmetrical tapered fiber based on evanescent field sensing", in *2015 IEEE International broadband and photonics conference (IBP)*, 2015, pp. 40–44.

[49]   R. M. Andre, C. R. Biazoli, S. O. Silva, M. B. Marques, C. M. B. Cordeiro, and O. Frazao, "Strain-temperature discrimination using multimode interference in tapered fiber", *IEEE PHOTONICS TECHNOLOGY LETTERS*, vol. 25, no. 2, pp. 155–158, Jan. 2013.

[50]   W. Huang, C. Xu, S. Chu, and S. K. Chaudhuri, "The finite-difference vector beam propagation method: Analysis and assessment", *JOURNAL OF LIGHTWAVE TECHNOLOGY*, vol. 10, no. 3, pp. 295–305, 1992.

[51]   E. Baude, "Numerical study of tapered fiber optics as evanescent field sensors", in *2013 SBMO/IEEE MTT-S International Microwave Optoelectronics Conference (IMOC)*, Aug. 2013, pp. 1–5.

[52]   L. Li and X. Sun, "Investigation on the tapered fiber evanescent-field sensor based on the comsol software", in *2012 Symposium on Photonics and Optoelectronics*, May 2012, pp. 1–3.

[53]   L. Tong, J. Lou, and E Mazur, "Single-mode guiding properties of subwavelength-diameter silica and silicon wire waveguides", *OPTICS EXPRESS*, vol. 12, no. 6, pp. 1025–1035, Mar. 2004.

[54]   F. Le. Kien, J. Liang, K. Hakuta, and V. Balykin, "Field intensity distributions and polarization orientations in a vacuum-clad subwavelength-diameter optical fiber", *OPTICS COMMUNICATIONS*, vol. 242, no. 4-6, pp. 445–455, Dec. 2004.

[55] P. Polynkin, A. Polynkin, N. Peyghambarian, and M. Mansuripur, "Evanescent field-based optical fiber sensing device for measuring the refractive index of liquids in microfluidic channels", *OPTICAL LETTERS*, vol. 30, no. 11, pp. 1273–1275, Jun. 2005.

[56] C. R. da Silveira, J. C.W. A. Costa, M. T. M. RoccoGiraldi, P. Jorge, A. P. Lopez Barbero, and S. B. Germano, "Bent optical fiber taper for refractive index measurements with tunable sensitivity", *MICROWAVE AND OPTICAL TECHNOLOGY LETTERS*, vol. 57, no. 4, pp. 921–924, Apr. 2015.

[57] L. B. Ha, K. Y. Ho, P. K. Seob, E. J. Beom, K. M. Jin, R. B. Sup, and C. H. Young, "Interferometric fiber optic sensors", *SENSORS*, vol. 12, no. 3, 2012.

[58] P. Wang, H. Zhao, X. Wang, G. Farrell, and G. Brambilla, "A review of multimode interference in tapered optical fibers and related applications", *SENSORS*, vol. 18, no. 3, Mar. 2018.

[59] L. Xu, Y. Li, and B. Li, "Nonadiabatic fiber taper-based mach-zehnder interferometer for refractive index sensing", *APPLIED PHYSICS LETTERS*, vol. 101, no. 15, Oct. 2012.

[60] K. Q. Kieu and M. Mansuripur, "Biconical fiber taper sensors", *IEEE PHOTONICS TECHNOLOGY LETTERS*, vol. 18, no. 21-24, pp. 2239–2241, Nov. 2006.

[61] Y. Hu, C. Jiang, M. Zhou, and J. Liu, "High-sensitivity fiber temperature and refractive index sensing with nonadiabatic fiber taper", *JOURNAL OF OPTICAL TECHNOLOGY*, vol. 85, no. 4, pp. 233–237, Apr. 2018.

[62] T. K Yadav, R. Narayanaswamy, M. H. A. Bakar, Y. M. Kamil, and M. A. Mahdi, "Single mode tapered fiber-optic interferometer based refractive index sensor and its application to protein sensing", *OPTICAL EXPRESSS*, vol. 22, no. 19, pp. 22 802–22 807, Sep. 2014.

[63] S. Mas, J. Marti, D. Monzon-Hernandez, and J. Palaci, "Low-cost refractive index and strain sensor based on tapered fibers", *OPTICS COMMUNICATIONS*, vol. 361, pp. 99–103, Feb. 2016.

[64] G. Salceda-Delgado, D. Monzon-Hernandez, A. Martinez-Rios, and G. A. Cardenas-Sevilla, "Optical microfiber mode interferometer for temperature-independent refractometric sensing", *OPTICAL LETTERS*, vol. 37, no. 11, pp. 1974–1976, Jun. 2012.

[65] T. Martan, J. Kanka, I. Kasik, and V. Matejec, "Theoretical analysis and preparation of tapered suspended core microstructure fibers", *INTERNATIONAL JOURNAL OF OPTOMECHATRONICS*, vol. 3, no. 3, pp. 233–249, 2009.

[66] H. C. Nguyen, B. T. Kuhlmey, E. C. Mägi, M. J. Steel, P. Domachuk, C. L. Smith, and B. J. Eggleton, "Tapered photonic crystal fibres: Properties, characterisation and applications", *APPLIED PHYSICS B*, vol. 81, no. 2, pp. 377–387, Jul. 2005.

[67] N. Jing, C. Teng, X. Zhao, and J. Zheng, "Temperature dependence of a refractive index sensor based on a macrobending micro-plastic optical fiber", *APPLIED OPTICS*, vol. 54, no. 8, pp. 1890–1893, Mar. 2015.

[68] C. Teng, F. Yu, N. Jing, and J. Zheng, "The influence of temperature to a refractive index sensor based on a macro-bending tapered plastic optical fiber", *OPTICAL FIBER TECHNOLOGY*, vol. 31, pp. 32 –35, Sep. 2016.

[69] P. Wang, G. Rajan, Y. Semenova, and G. Farrell, "Temperature dependence of a macrobending edge filter based on a high-bend loss fiber", *OPTICS LETTERS*, vol. 33, no. 21, pp. 2470–2472, Nov. 2008.

[70] C. Beres, F. V. B. de Nazar, N. C. C. de Souza, M. A. L. Miguel, and M. M. Werneck, "Tapered plastic optical fiber-based biosensor-tests and application", *BIOSENSORS & BIOELECTRONIC*, vol. 30, no. 1, pp. 328–332, Dec. 2011.

[71] H.-Y. Lin, C.-H. Huang, G.-L. Cheng, N.-K. Chen, and H.-C. Chui, "Tapered optical fiber sensor based on localized surface plasmon resonance", *OPTICAL EXPRESS*, vol. 20, no. 19, pp. 21 693–21 701, Sep. 2012.

[72] E. Yablonovitch, "Photonic band-gap structures", *JOURNAL OF THE OPTICAL SOCIETY OF AMERICA*, vol. 10, no. 2, pp. 283–295, Feb. 1993.

[73] J. C. Knight, T. A. Birks, P. S. J. Russell, and D. M. Atkin, "All-silica single-mode optical fiber with photonic crystal cladding", *OPTICAL LETTERS*, vol. 21, no. 19, pp. 1547–1549, Oct. 1996.

[74] A. S. Cerqueira Jr., "Recent progress and novel applications of photonic crystal fibers", *REPORTS ON PROGRESS IN PHYSICS*, vol. 73, no. 2, Feb. 2010.

[75] M Feng, A. Mairaj, D. Hewak, and T. Monro, "Nonsilica glasses for holey fibers", *JOURNAL OF LIGHTWAVE TECHNOLOGY*, vol. 23, no. 6, pp. 2046–2054, Jun. 2005.

[76] T. M. Monro, K. M. Kiang, J. H. Lee, K. Frampton, Z. Yusoff, R. Moore, J.Tucknott, D. W. Hewak, H. N. Rutt, and D. J. Richardson, "High nonlinearity extruded single-mode holey optical fibers", in *Optical Fiber Communication Conference and Exhibit*, Mar. 2002, FA1–1–FA1–3.

[77] A. S. Webb, F. Poletti, D. J. Richardson, and J. K. Sahu, "Suspended-core holey fiber for evanescent-field sensing", *OPTICAL ENGINEERING*, vol. 46, pp. 46 –49, 2007.

[78] Y. Hoo, W Jin, C. Shi, H. Ho, D. Wang, and S. Ruan, "Design and modeling of a photonic crystal fiber gas sensor", *APPLIED OPTICS*, vol. 42, no. 18, pp. 3509–3515, Jun. 2003.

[79] J. Jensen, P. Hoiby, G Emiliyanov, O Bang, L. Pedersen, and A Bjarklev, "Selective detection of antibodies in microstructured polymer optical fibers", *OPTICS EXPRESS*, vol. 13, no. 15, pp. 5883–5889, Jul. 2005.

[80] J. Knight, J Broeng, T. Birks, and P. Russel, "Photonic band cap guidance in optical fibers", *SCIENCE*, vol. 282, no. 5393, pp. 1476–1478, Nov. 1998.

[81] K. Kurokawa, K. Nakajima, K. Tsujikawa, T. Yamamoto, and K. Tajima, "Ultra-wideband transmission over low loss pcf", *J. LIGHTWAVW TECHNOLOGY*, vol. 27, no. 11, pp. 1653–1662, Jun. 2009.

[82] A. M. Cubillas, S. Unterkofler, T. G. Euser, B. J. M. Etzold, A. C. Jones, P. J. Sadler, P. Wasserscheid, and P. S. J. Russell, "Photonic crystal fibres for chemical sensing and photochemistry", *CHEMICAL SOCIETY REVIEWS*, vol. 42, no. 22, pp. 8629–8648, 2013.

[83] P. Sazio, A Amezcua-Correa, C. Finlayson, J. Hayes, T. Scheidemantel, N. Baril, B. Jackson, D. Won, F Zhang, E. Margine, V Gopalan, V. Crespi, and J. Badding, "Microstructured optical fibers as high-pressure microfluidic reactors", *SCIENCE*, vol. 311, no. 5767, pp. 1583–1586, Mar. 2006.

[84] E. W. Washburn, "The dynamics of capillary flow", *PHYSICAL REVIEW JOURNALS*, vol. 17, pp. 273–283, 3 Mar. 1921.

[85] J. Tian, Z. Lu, M. Quan, Y. Jiao, and Y. Yao, "Fast response fabry-perot interferometer microfluidic refractive index fiber sensor based on concave-core photonic crystal fiber", *OPTICS EXPRESS*, vol. 24, no. 18, pp. 20 132–20 142, Sep. 2016.

[86] C. M. B. Cordeiro, C. J. S. de Matos, E. M. dos Santos, A. Bozolan, J. S. K. Ong, T. Facincani, G. Chesini, A. R. Vaz, and C. H. B. Cruz, "Towards practical liquid and gas sensing with photonic crystal fibres: Side access to the fibre microstructure and single-mode liquid-core fibre", *MEASUREMENT SCIENCE AND TECHNOLOGY*, vol. 18, no. 10, pp. 3075–3081, 2007.

[87] C. M. B. Cordeiro, M. A. R. Franco, G. Chesini, E. C. S. Barretto, R. Lwin, C. H. B. Cruz, and M. C. J. Large, "Microstructured-core optical fibre for evanescent sensing applications", *OPTICS EXPRESS*, vol. 14, no. 26, pp. 13 056–13 066, Dec. 2006.

[88] F. M. Cox, R. Lwin, M. C. J. Large, and C. M. B. Cordeiro, "Opening up optical fibres", *OPTICS EXPRESS*, vol. 15, no. 19, pp. 11 843–11 848, Sep. 2007.

[89] S. C. Warren-Smith, H. Ebendorff-Heidepriem, T. C. Foo, R. Moore, C. Davis, and T. M. Monro, "Exposed-core microstructured optical fibers for real-time fluorescence sensing", *OPTICAL EXPRESS*, vol. 17, no. 21, pp. 18 533–18 542, Oct. 2009.

[90] R. Kostecki, H. Ebendorff-Heidepriem, S. C. Warren-Smith, and T. M. Monro, "Predicting the drawing conditions for microstructured optical fiber fabrication", *OPTICAL MATERIALS EXPRESS*, vol. 4, no. 1, pp. 29–40, Jan. 2014.

[91] A. van Brakel, C. Grivas, M. N. Petrovich, and D. J. Richardson, "Micro-channels machined in microstructured optical fibers by femtosecond laser", *OPTICAL EXPRESS*, vol. 15, pp. 8731–8736, Jul. 2007.

[92] R. Kostecki, H. Ebendorff-Heidepriem, C. Davis, G. McAdam, S. C. Warren-Smith, and T. M. Monro, "Silica exposed-core microstructured optical fibers", *OPTICAL MATERIALS EXPRESS*, vol. 2, no. 11, pp. 1538–1547, Nov. 2012.

[93] E. P. Schartner, A. Dowler, and H. Ebendorff-Heidepriem, "Fabrication of low-loss, small-core exposed core microstructured optical fibers", *OPTICAL MATERIALS EXPRESS*, vol. 7, no. 5, pp. 1496–1502, May 2017.

[94] J. R. Sparks, J. L. Esbenshade, R. He, N. Healy, T. D. Day, D. W. Keefer, P. J. A. Sazio, A. C. Peacock, and J. V. Badding, "Selective semiconductor filling of microstructured optical fibers", *JOURNAL OF LIGHTWAVE TECHNOLOGY*, vol. 29, no. 13, pp. 2005–2008, 2011.

[95] C. J. S. de Matos, C. M. B. Cordeiro, E. M. dos Santos, J. S. K. Ong, A. Bozolan, and C. H. B. Cruz, "Liquid-core, liquid-cladding photonic crystal fibers", *OPTICS EXPRESS*, vol. 15, no. 18, pp. 11 207–11 212, Sep. 2007.

[96] Y. Wang, S. Liu, X. Tan, and W. Jin, "Selective-fluid-filling technique of microstructured optical fibers", *JOURNAL OF LIGHTWAVE TECHNOLOGY*, vol. 28, no. 22, pp. 3193–3196, Nov. 2010.

[97] H. Ebendorff-Heidepriem, S. C. Warren-Smith, and T. M. Monro, "Suspended nanowires: Fabrication, design and characterization of fibers with nanoscale cores", *OPTICAL EXPRESS*, vol. 17, no. 4, pp. 2646–2657, Feb. 2009.

[98] S. Selleri, E. Coscelli, M. Sozzi, A. Cucinotta, F. Poli, and D. Passaro, "Air-suspended solid-core fibers for sensing", in *Optical sensors 2009*, ser. Proceedings of SPIE, SPIE, vol. 7356, 2009.

[99]   A. Mazhorova, A. Markov, A. Ng, R. Chinnappan, O. Skorobogata, M. Zourob, and M. Skorobogatiy, "Label-free bacteria detection using evanescent mode of a suspended core terahertz fiber", *OPTICS EXPRESS*, vol. 20, no. 5, pp. 5344–5355, Feb. 2012.

[100] T. Monro, W Belardi, K Furusawa, J. Baggett, N. Broderick, and D. Richardson, "Sensing with microstructured optical fibres", *MEASUREMENT SCIENCE AND TECHNOLOGY*, vol. 12, no. 7, pp. 854–858, Jul. 2001.

[101] J. Fini, "Microstructure fibres for optical sensing in gases and liquids", *MEASURE- MENT SCIENCE AND TECHNOLOGY*, vol. 15, no. 6, pp. 1120–1128, Jun. 2004.

[102] Y. Hoo, W Jin, H. Ho, D. Wang, and R. Windeler, "Evanescent-wave gas sensing using microstructure fiber", *OPTICAL ENGINEERING*, vol. 41, no. 1, pp. 8–9, Jan. 2002.

[103] J. Chen, A. Hangauer, R. Strzoda, T. G. Euser, J. S. Y. Chen, M. Scharrer, P. S. J. Russell, and M. C. Amann, "Sensitivity limits for near- infrared gas sensing with suspended-core pcfs directly coupled with vcsels", in *2010 Conference on lasers and electro-optics (CLEO) And quantum electronics and laser science conference (QELS)*, 2010.

[104] J. S. Y. Chen, T. G. Euser, N. J. Farrer, P. J. Sadler, M. Scharrer, and P. S. J. Russell, "Photochemistry in photonic crystal fiber nanoreactors", *CHEMISTRY-A EUROPEAN JOURNAL*, vol. 16, no. 19, pp. 5607–5612, 2010.

[105] S. C. Warren-Smith, S. Afshar, and T. M. Monro, "Theoretical study of liquid- immersed exposed-core microstructured optical fibers for sensing", *OPTICS EX- PRESS*, vol. 16, no. 12, pp. 9034–9045, Jun. 2008.

[106] S. C. Warren-Smith, S. Heng, H. Ebendorff-Heidepriem, A. D. Abell, and T. M. Monro, "Fluorescence-based aluminum ion sensing using a surface-functionalized microstructured optical fiber", *Langmuir*, vol. 27, no. 9, pp. 5680–5685, 2011.

[107] S. C. Warren-Smith, R. Kostecki, L. V. Nguyen, and T. M. Monro, "Fabrication, splicing, bragg grating writing, and polyelectrolyte functionalization of exposed- core microstructured optical fibers", *OPTICALL EXPRESS*, vol. 22, no. 24, Dec. 2014.

[108] T. M. Monro, S. Warren-Smith, E. P. Schartner, A. Franois, S. Heng, H. Ebendorff- Heidepriem, and S. Afshar, "Sensing with suspended-core optical fibers", *OP- TICAL FIBER TECHNOLOGY*, vol. 16, no. 6, pp. 343 –356, 2010.

[109] P. J. Roberts, F. Couny, H. Sabert, B. J. Mangan, T. A. Birks, J. C. Knight, and P. S. J. Russell, "Loss in solid-core photonic crystal fibers due to interface roughness scattering", *OPTICAL EXPRESS*, vol. 13, no. 20, pp. 7779–7793, Oct. 2005.

[110] H. Ebendorff-Heidepriem and T. M. Monro, "Extrusion of complex preforms for microstructured optical fibers", *OPTICAL EXPRESS*, vol. 15, no. 23, pp. 15 086–15 092, Nov. 2007.

[111] G. Zhai and L. Tong, "Roughness-induced radiation losses in optical micro or nanofibers", *OPTICS EXPRESS*, vol. 15, no. 21, pp. 13 805–13 816, Oct. 2007.

[112] H. Lehmann, J. Kobelke, K. Schuster, R. Willsch, H. Bartelt, R. Amezcua-Correa, and J. C. Knight, "Gas sensing with suspended core fibres and hollow core band gap fibres: A comparative study", ser. Proceedings of SPIE, vol. 7503, 2009, pp. 7503–7504.

[113] K. Schuster, H. Lehmann, T. Elsmann, T. Habisreuther, and S. Dochow, "Specialty fibers for fiber-optic sensors", in *2014 Optical fiber communication conference and exhibition (OFC)*, 2014.

[114] G. Yin, Y. Wang, C. Liao, B. Sun, Y. Liu, S. Liu, Q. Wang, K. Yang, J. Tang, and X. Zhong, "Simultaneous refractive index and temperature measurement with lpfg and liquid-filled pcf", *IEEE PHOTONICS TECHNOLOGY LETTERS*, vol. 27, no. 4, pp. 375–378, Feb. 2015.

Author's publications

List of author's publications related to the doctoral thesis

All authors contributed equally unless otherwise stated.

Papers in Peer-Reviewed Journals with Impact Factor:

[J1] E. A. Romanova, S. Korsakova, M. Komanec, T. Nemecek, A. Velmuzhov, M. Sukhanov, and V. S. Shiryaev, "Multimode Chalcogenide Fibers for Evanescent Wave Sensing in the Mid-IR", IEEE JOURNAL OF SELECTED TOPICS IN QUANTUM ELECTRONICS, vol. 23, no. 2, num. 5601507 2017.

[J2] M. Komanec, T. Martan, T. Nemecek, and S. Zvanovec, "Multimode fiber tapers for reproducible refractometric liquid detection", OPTICAL ENGINEERING, vol. 54, no. 4, num. 047102, 2015.

[J3] M. Komanec, T. Nemecek, P. M. Vidner, T. Martan, F. Lahodny, and S. Zvanovec, "Structurally-modified tapered optical fiber sensors for long-term detection of liquids", OPTICAL FIBER TECHNOLOGY, vol. 47, pp. 187 –191, 2019.

[J4] T. Nemecek, M. Komanec, T. Martan, R. Ahmad, and S. Zvanovec, "Suspended-core microstructured fiber for refractometric detection of liquids", APPLIED OPTICS, vol. 54, no. 30, pp. 8899–8903, 2015.

[J5] A. N. Castro Martinez, M. Komanec, T. Nemecek, S. Zvanovec, and S. Khotiaintsev, "Fiber optic refractometric sensors using a semi-ellipsoidal sensing element", APPLIED OPTICS, vol. 55, no. 10, pp. 2574–2579, 2016.

[J6] T. Martan, T. Nemecek, M. Komanec, R. Ahmad, and S. Zvanovec, "Refractometric detection of liquids using tapered optical fiber and suspended core microstructured fiber: a comparison of methods", APPLIED OPTICS, vol. 56, no. 9, pp. 2388–2396, 2017.

[J7] T. Nemecek, M. Komanec, B. Nelsen, T. Martan, D. Suslov, P. Hartmann, and S. Zvanovec, "Experimentally and analytically derived generalized model for the detection of liquids with suspended-core optical fibers", OPTICAL FIBER TECHNOLOGY, vol. 45, pp. 295–299, 2018.

Papers in Conference Proceedings Listed in Web of Knowledge:

[C1] T. Nemecek, M. Komanec, and S. Zvanovec, "Liquid analytes filling process in suspended-core silica fibers", in *20th Microoptics conference (MOC)*, IEEE, 2015.

[C2] M. Komanec, T. Nemecek, D. Suslov, R. Ahmad, and S. Zvanovec, "Detection of liquids in the near and mid-infrared based on lead-silicate suspended-core microstructured fibers", in Photonics fiber and crystal devices" advances in material and innovations in device applicatinos, ser. Proceedings of SPIE, pp. 9958 - 9964, 2016.

[C3] M. Komanec, T. Nemecek, R. Ahmad, T. Martan, D. Suslov, and S. Zvanovec, "Suspended-core silica and lead-silicate fibers for nonlinear application and sensing purposes", in Micro-structured and specialty optical fibers IV, ser. Proceedings of SPIE, pp. 9886-9891, 2016.

List of author's publications non-related to the doctoral thesis

All authors contributed equally unless otherwise stated.

Papers in Conference Proceedings Listed in Web of Knowledge:

[C4] T. Nemecek, J. Bohata, D. Suslov, M. Komanec, S. Zvanovec, and R. Ahmad, "On the dispersion and mode-field characterization of photonic crystal fibers for nonlinear application", in 2nd International conference on automation, Cognitive science, optics, micro electro-mechanical systems, And information technology (ICACOMIT), pp. 147–151, 2017.

[C5] J. Bohata, S. Zvanovec, T. Nemecek, and M. Komanec, "Detailed Analysis of Multi-Mode Optical Components for Utilization in Data Centers", in 2017 Global information infrastructure and networking symposium (GIIS), pp. 45–49, 2017.

[C6] T. Nemecek, M. Komanec, D. Suslov, P. Peterka, D. Pysz, R. Buczynski, B. Nelsen, and S. Zvanovec, "Development and characterization of highly nonlinear multicomponent glass photonic crystal fibers for mid-infrared applications", in Micro-structured and specialty optical fibers, ser. Proceedings of SPIE, SPIE, pp. 10232, 2017.

[C7] M. Komanec, T. Nemecek, D. Suslov, R. Ahmad, and T. Martan, "Optical Switching Based on Arsenic-Selenide and Lead-Silicate Fibers", in 2016 10th International symposium on communication systems, networks and digital signal processing (CSNDSP), 2016.

[C8] D. Suslov, M. Komanec, T. Nemecek, and S. Zvanovec, "High-efficiency coupling to small-core microstructured fibers for broadband dispersion characterization", in Laser resonators, microresonators, and beamcontrol XX., Bellingham WA, SPIE, San Francisco, 2018.

[C9] B. Venema, T. Nemecek, N. Blanik, V. Blazek, and S. Leonhardt, "Pulse oximetry imaging—practical feasibility and theoretical limitations", in Journal of clinical monitoring and computing, vol. 31, pp. 496–496, 2017.

[C10] Bohata, J.; Zvanovec, S.; Nemecek, T.; Komanec, M. "Impact of Precise Measurements of Multi-Mode fiber components for Data Centers", in 29th Conference and Exhibition on OPTICAL COMMUNICATIONS 2018. Praha, pp. 8-12, 2018.

[C11] T. Nemecek, B. Nelsen, M. Komanec, D. Suslov, and S. Zvanovec, "The influence optical elements of the chromatic dispersion measurements of photonic crystal fibers", Abstract book of RIAO OPTILAS 2016 Washington, DC: The Optical society, pp. 51, 2016.

Citations of the articles included in the Dissertation thesis

Citations in Web of Knowledge and SCOPUS (except self-citations):

[Ci1] A. Sincore, and J. Cook, F. Tan, A. F. Abouraddy, M. C. Richardson and K. L.Schepler, L. Kenneth, "Practical limits of power transmission through single-mode chalcogenide fibers", in OPTICAL ENGINEERING, vol. 57, no. 11, NOV 2018. – citing [J1]

[Ci2] Z Hui, Y. Zhang A-H. Soliman, "Mid-infrared dual-rhombic air hole Ge20Sb15Se65 chalcogenide photonic crystal fiber with high birefringence and high nonlinearity", in CERAMICS INTERNATIONAL, vol. 44, no. 9, pp. 10383-10392, JUN, 2018. - citing [J1]

[Ci3] A. Saha, A. Datta S. Kaman, "Ultrahigh-sensitive multimode interference-based fiber optic liquid-level sensor realized using illuminating zero-order Bessel-Gauss beam, OPTICAL ENGINEERING, vol. 57, no. 3, MAR 2018. -citing [J2]

[Ci4] J. Pniewski, A. Ramaniuk, R. Kasztelanic, M. Smietana, M. Trippenbach, R. Buczynski, "Applicability of suspended-core fibres for attenuation-based label-free biosensing", in OPTICS COMMUNICATIONS, vol. 402, pp. 290-295, NOV 2017. - citing [J4]

[Ci5] A. Gonzalez-Vila, D. Kinet, P. Megret Ch. Caucheteur, "Narrowband interrogation of plasmonic optical fiber biosensors based on spectral combs", OPTICS AND LASER TECHNOLOGY, vol. 96, pp. 141-146, NOV 2017. - citing [J5]